UNIVERSITÀ DEGLI SUDI DI SALERNO

Facoltà di Scienze Matematiche Fisiche e Naturali

Dottorato di Ricerca in Fisica IX Ciclo II Serie

The neutrino interaction analysis chain in OPERA

Coordinatore del dottorato:
Prof. Giuseppe Grella

Candidata:
Dr.ssa Regina Rescigno

Relatori:
Prof. Giuseppe Grella
Università degli Studi di Salerno

Dr. Cristiano Bozza
Università degli Studi di Salerno

Correlatore:
Prof. Dario Autiero
IPNL, Università Claude Bernard Lione I – Francia

ANNO ACCADEMICO 2010/2011

Contents

Introduction

The aim of the OPERA experiment is to provide a “smoking-gun” proof of neutrino oscillations, through the detection of the appearance signal of ν_τ’s in an initially pure ν_μ beam. The beam is produced at CERN, 732 Km far from the detector, which is located underground in the Gran Sasso laboratory.

The evidence of the appearance signal will be provided by the detection of the daughter particles produced in the decay of the τ lepton. A micro-metric spatial resolution is needed in order to measure and study the topology of the ν_τ-induced events. With this goal, nuclear emulsions, the highest resolution tracking detector, were chosen to be the core of the OPERA apparatus.

The analysis of the large amount of nuclear emulsions used in the OPERA experiment has required the development of a new generation of fast automatic microscopes, featuring a scanning speed more than one order of magnitude higher than in past emulsion-based experiments. The long R&D carried out by the Collaboration has given rise to two new systems: the European Scanning System (ESS) and the Japanese S-UTS.

The work presented in this thesis has been carried out in one of the laboratories involved in the OPERA emulsion scanning, hosted at the University of Salerno, and during a 6 month’s stay at the IPNL (Institut de Physique Nucleaire de Lyon).

As for emulsion data-taking, several bricks from the 2008, 2009 and 2010 OPERA runs were scanned in Salerno and about 250 ν_μ-induced events were located. For the events triggered in the 2008 run, a kinematical analysis was performed, by developing a new likelihood-based software, able to estimate the momentum of the particles traversing the emulsion sheets through multiple Coulomb scattering. The algorithm was also tested on a set of Monte-Carlo data and a set of pion tracks collected during the 2003, 2004 and 2007 test beam campaigns at CERN. The 2008 run sample was used also to perform the

hadron interaction search and the data collected were merged with those from other laboratories to estimate the background to the hadronic decay channel.

The kinematical analysis of the $\tau \rightarrow h$ decay channel is the subject of the second part of this thesis, developed while staying at the IPNL. The study on the quantities used to discriminate the signal and the background was accomplished by using simulated data. The kinematical cuts suggested by the OPERA Proposal were reviewed and the efficiencies obtained by applying these cuts were re-computed. In addition, another set of discriminating variables are suggested and their background suppression power is explored. Such estimators are proposed to be the subject of further work in the years to come.

Chapter 1

Neutrino Physics overview

In 1930 Wolfgang Pauli postulated the existence of the neutrino in order to reconcile data on the radioactive decay of nuclei with energy conservation [1]. In this decay neutrons are transformed into slightly lighter protons with emission of electrons:

$$\text{neutron} \rightarrow \text{proton} + \text{electron} + \text{antineutrino}$$

Without neutrino, the energy conservation law required that electron and proton share the neutron energy. In this case each electron would be produced with a monochromatic energy distribution, whereas experiments observed a continuous spectrum, as would be expected for a three-body decay.

The postulated neutrino is chargless and interacts very weakly with matter; it just serves the purpose to balance energy and momentum in the above reaction. In fact, Pauli pointed out that for neutrino to do the job, it had to weigh less than one percent of proton mass, thus establishing the first limit of neutrino mass.

In the next years many efforts have been performed to confirm the existence of this new particle and to understand better its properties. Neutrinos were directly observed by Reines and Cowan in a nuclear reactor experiment in 1956 [2] and found to be left-handed in 1958 [3]. Four years later Lederman, Schwartz and Steinberger established that neutrinos associated to electrons and muons are different particles [4].

Since then, neutrinos have been considered as an essential part of the quantum description of fundamental particles and forces, the Standard Model of Particle Physics [5], [6], [7]. In absence of a direct observation of their masses, neutrinos are introduced in this model as fermionic massless particles.

The first clues that neutrino have mass came from a deep underground experiment carried out by Davis, detecting solar neutrinos. It revealed only about one-third of the flux predicted by Solar models [8], [9]. This result suggested that the solar neutrinos might be transforming into something else. Only electron neutrinos are emitted by the Sun and they could be converting to muon and tau neutrinos, not being detected by the experiments. This phenomen, called "neutrino oscillations", was first proposed by Pontecorvo [10].

If neutrino oscillations exist, neutrinos have to be considered, in the Standard Model, as massive particles and their description needs to be revised.

In this chapter, an overview of Standard Model extensions is given and results of neutrino oscillation experiments are shown.

1.1. Neutrino masses and mixing

The Standard Model of Particle Physics (SM) is a description of strong, weak and electromagnetic interactions. In the formulation provided by Glashow [5], Salam [7] and Weinberg [6], neutrinos are massless fermions having neither strong nor electromagnetic interactions. In the 'basic' SM, there are no RH (right-handed) neutrinos, according with the result of Goldhaber et al. [11] that weakly interacting neutrinos are always left-handed.

The non-existence of RH neutrinos is one of the reasons why neutrino mass might be vanishing. Unlike photons, no profound principle protect the neutrinos from having mass; therefore, by adding RH neutrinos, the Higgs mechanism of the Standard Model can give neutrinos the same type of mass as the electron mass or other charged lepton and quarks.

1.1.1. Mass generation

In the Lagrangian density for the quantum field theory, the Dirac mass term can be written as:

$$L_D = -m_D\bar{\psi}\psi = -m_D(\bar{\psi}_R\psi_L + \bar{\psi}_L\psi_R) \qquad 1.1$$

Such Dirac mass term appears in this form but it can be regarded, for simplicity, as an 'coupling' between left-handed and right-handed particle fields (as shown in Figure 1.1).

It is possible to add right-handed neutrinos (ν_R) to the Standard Model, providing that they do not take part in the weak interactions. A Dirac mass for the neutrino (m_{LR}) would naturally arise as shown in the upper part of Figure 1.2. It is also possible to give neutrinos a new kind of mass called a Majorana[1] [12] mass (m_{LL}) if the LH neutrinos ν_L

[1] Majorana particle is a particle that is its own antiparticle.

are coupled with its own charge and parity conjugated state, the RH antineutrino (ν_L^C) where 'C' denotes the simultaneous operations of charge and parity conjugation.

RH neutrinos can also independently acquire their own Majorana masses M_{RR}, by interacting with their own CP conjugates ν_R^C (Figure 1.3).

In quantum field theory language, this is possible if new fields are added to the 'basic' Standard Model. An arbitrary number *n* of sterile neutrinos ν_s is added to the three standard generations and they can be used to construct two types of mass terms:

$$L_D = \bar{\nu}_{s,i} M^D_{ik} \nu_{L,k} \qquad L_M = \bar{\nu}_{s,i} M^M_{ij} \nu^C_{s,j} \tag{1.2}$$

where $\nu_L = (\nu_{L,1}, \nu_{L,2}, \nu_{L,3})$ are the three active neutrinos fields (only LH) and $\nu_s = (\nu_{s,1}, \nu_{s,2} \ldots \nu_{s,n})$ are RH sterile neutrino fields.

L_D is the Dirac mass term and it is generated after spontaneous electroweak symmetry breaking from a Yukawa-like interaction; it has a neutrino field and an antineutrino field, and conserves the total lepton number. M^D is a complex $3 \times n$ matrix.

L_M is a Majorana mass term and since it involves two neutrino fields, it breaks lepton number conservation by two units; M^M is a symmetric matrix of dimension $n \times n$.

The most general mass terms we can write for ν is a combination of Dirac and Majorana mass term:

$$L = -\begin{pmatrix} \bar{\nu}_L & \bar{\nu}_s^C \end{pmatrix} \begin{pmatrix} m_{LL} & m_{LR} \\ m_{LR}^T & M_{RR} \end{pmatrix} \begin{pmatrix} \nu_L^C \\ \nu_s \end{pmatrix} + h.c. \tag{1.3}$$

To find the mass states we need to diagonalise the mass matrix, i.e. find its eigenvalues and eigenstates.

Figure 1.1: The electron Dirac mass m_e can be thought of as an interaction between a left-handed electron e_L^- and a right-handed electron e_R^-. The long (blue) arrows denote the electron momentum vector and the short (red) arrows denote the electron spin vector. For right-handed electrons e_R^- the spin vector and the momentum vector are aligned, whereas for left-handed electrons e_L^- they are opposite. The mass term may be regarded as interactions that enable left-handed electrons to interact with right -handed electrons.

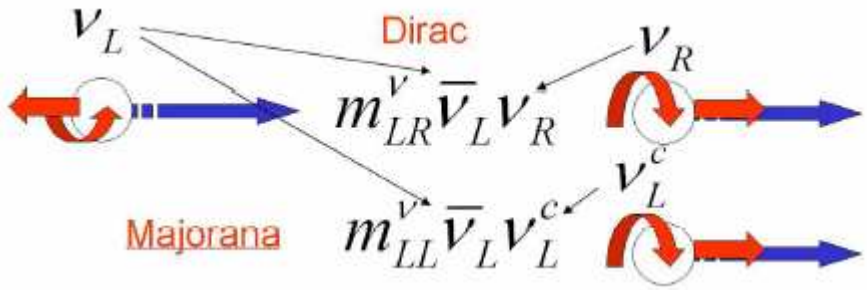

Figure 1.2: For neutrinos there are two types of mass that are possible. As in the case of the electron there is the Dirac mass m_{LR}^{ν} that couples a left-handed neutrino ν_L to a right-handed neutrino ν_R (upper part of he diagram). The role of a right handed neutrino can be played by ν_L^C obtained by transforming the left-handed neutrino ν_L under the operations charge and parity conjugation, where ν_L^C is a right-handed neutrino. If ν_L interacts with ν_L^C this results in Majorana mass term m_{LL}^{ν}.

Figure 1.3: If right-handed neutrinos ν_R are added to the Standard Model, than they also acquire a Majorana mass term M_{RR} by coupling to their own charge and parity conjugated states ν_R^C.

1.1.1.a. The See-Saw Model

As anticipated in the previous section, three neutrino mass terms are possible. Majorana mass terms read $m_{LL}\bar{\nu}_L\nu_L^C$ and $M_{RR}\bar{\nu}_R\nu_R^C$; the Dirac mass term reads $m_{LR}\bar{\nu}_L\nu_R$.

Although left-handed Majorana masses m_{LL} are possible in principle, in the Standard Model they are constrained to zero by the Higgs mechanism. However there is nothing preventing RH neutrinos from having Majorana masses M_{RR}, where the magnitude of such masses can take any value ; in particular such masses might be much larger than those of other particles. LH neutrinos take-part in weak interactions with the W and Z bosons and if they were very heavy the theory would be disturbed. RH neutrinos on the other hand do not take part in weak interactions and so their mass M_{RR} can be large. The heaviness of M_{RR} cannot be motivated in the framework of the Standard Model, but if one believes that the Standard Model is a theory that describes the world only at low energies, it is quite natural to expect that the mass M_{RR} is generated at ultra-high energy by the symmetry breaking of the theory beyond the Standard Model.

The idea of the simplest version of See-Saw mechanism [13], [14] is to assume that the mass terms m_{LL} are zero to begin with, but are generated effectively, after RH neutrinos are introduced. Another fundamental assumption, as anticipated, is that $M_{RR} >> m_{LR}$. In this hypothesis the See-Saw mass matrix is:

$$L = -\begin{pmatrix} \bar{\nu}_L & \bar{\nu}_s^C \end{pmatrix} \begin{pmatrix} 0 & m_{LR} \\ m_{LR}^T & M_{RR} \end{pmatrix} \begin{pmatrix} \nu_L^C \\ \nu_s \end{pmatrix} + h.c. \qquad 1.4$$

In the approximation that $M_{RR} >> m_{LR}$ the matrix can be diagonalised to yield effective Majorana masses of the type m_{LL}:

$$m_{LL} = m_{LR} M_{RR}^{-1} m_{LR}^T$$

The effective left-handed Majorana masses m_{LL} are naturally suppressed by the heavy scale M_{RR}.

1.1.2. Neutrino mixing

Two different neutrino bases have been introduced, (ν_e, ν_μ, ν_τ) being the flavour basis, and (ν_1, ν_2, ν_3) being the neutrino mass basis.

The three flavour states are related to the three neutrino mass states by an unitary matrix U, the "lepton mixing matrix" (known as the Pontecorvo-Maki-Nakagawa-Sakata matrix [15], [16]):

$$\begin{pmatrix} \nu_e \\ \nu_\mu \\ \nu_\tau \end{pmatrix} = \begin{pmatrix} U_{e1} & U_{e2} & U_{e3} \\ U_{\mu 1} & U_{\mu 2} & U_{\mu 3} \\ U_{\tau 1} & U_{\tau 2} & U_{\tau 3} \end{pmatrix} \begin{pmatrix} \nu_1 \\ \nu_2 \\ \nu_3 \end{pmatrix} \qquad 1.5$$

This 3×3 matrix can be parameterized in terms of three mixing angles θ_{ij} and three complex phases (one named after Dirac and the other two after Majorana). Generally, a unitary matrix has six phases but, in this case, three of them are removed by properly choosing the eigenstates. Since the neutrino masses are Majorana there is no additional phase associated with them.

The most common parameterization of the mixing matrix is:

$$U = \begin{pmatrix} 1 & 0 & 0 \\ 0 & c_{23} & s_{23} \\ 0 & -s_{23} & c_{23} \end{pmatrix} \begin{pmatrix} c_{13} & 0 & s_{13}e^{-i\delta} \\ 0 & 1 & 0 \\ -s_{13}e^{-i\delta} & 0 & c_{13} \end{pmatrix} \begin{pmatrix} c_{12} & s_{12} & 0 \\ -s_{12} & c_{12} & 0 \\ 0 & 0 & 1 \end{pmatrix} \begin{pmatrix} e^{i\alpha_1/2} & 0 & 0 \\ 0 & e^{i\alpha_2/2} & 0 \\ 0 & 0 & 1 \end{pmatrix} \qquad 1.6$$

where s_{ij} and c_{ij} stand for, respectively, the sines and cosines of the mixing angles θ_{ij}, δ is the Dirac phase and α_i (i = 1, 2) are the Majorana phases.

The matrix U is factorized in a matrix product of four matrices associated with the physics of neutrinos coming from different sources. As will be shown in section 1.3,

experiments with three different neutrino sources are possible and they investigate different oscillation channels.

Atmospheric neutrinos experiments suggest the possibility of having $\nu_\mu \rightarrow \nu_\tau$ oscillation (first matrix). The second matrix is associated with the physics of reactor neutrino oscillations ($\nu_e \rightarrow \nu_\mu,\nu_\tau$) and here a δ phase (providing a possible source of CP violation) appears [17], [18], [19]. The third matrix is probed by experiments with Solar neutrinos (commonly interpreted as $\nu_e \rightarrow \nu_\mu$ oscillations). The last matrix contains the Majorana phases that are not involved in neutrino oscillations.

1.2. Neutrino oscillation

The history of neutrino oscillations dates back to the work by Pontecorvo who in 1957 proposed $\nu \rightarrow \bar{\nu}$ oscillations in analogy with $K \rightarrow \bar{K}$ oscillations, described as the mixing of two Majorana neutrinos [16]. Pontecorvo was the first to realise that what we call "electron neutrino", for example, may be a linear combination of mass eigenstate neutrinos, and that this feature could lead to neutrino oscillations such as $\nu_e \rightarrow \nu_\mu$.

Neutrino oscillations in vacuum would arise if neutrinos are massive ad mixed. From equation 1.5 we see that if neutrinos have mass, the eigenstate ν_α (α = e, μ, τ) produced in a weak interaction with energy E is, in general, a linear combination of the mass eigenestates ν_i with energy E_i, and mass m_i

$$\left|\nu_\alpha\right\rangle = \sum_{i=1}^{n} U_{\alpha i}^{*} \left|\nu_i\right\rangle \qquad 1.7$$

After travelling a distance L (or, equivalently, time t) a neutrino originally produced with a flavor α evolves as follows:

$$\left|\nu_\alpha(t)\right\rangle = \sum_{i=1}^{n} U_{\alpha i}^{*} \left|\nu_i(t)\right\rangle \quad \textit{where} \quad \left|\nu_i(t)\right\rangle = e^{-iE_i t}\left|\nu_i(0)\right\rangle \qquad 1.8$$

The probability to find state $|\nu_\beta>$ after a time t, starting from a state $|\nu_\alpha>$ is:

$$P(\nu_\alpha \rightarrow \nu_\beta) = \left|\left\langle \nu_\beta(t) \middle| \nu_\alpha(0) \right\rangle\right|^2 = \left|\sum_{i=1}^{n} U_{\beta i} e^{-iE_i t} U_{\alpha i}^{*}\right|^2 \qquad 1.9$$

Remembering that U is a unitary matrix and by using the ultra-relativistic approximations $E_i = \sqrt{p_i^2 + m_i^2} \simeq p_i + m_i / 2E$ it is possible to rewrite equation 1.9 as:

$$P(\nu_\alpha \to \nu_\beta) = \left| \delta_{\alpha\beta} + \sum_{i=2}^{n} U_{\beta i} U_{\alpha i}^{*} [e^{-i\frac{\Delta m_{i1}^2}{2E}L} - 1] \right|^2 \qquad 1.10$$

where $\Delta m_{i1}^2 = m_i^2 - m_1^2$ and $L = ct$ is the distance between the source and the detector. Equation (1.10) shows that transition probability depends on elements of the mixing matrix, on the difference of the squares of neutrino masses and on the parameter L/E, defined by the experimental setup. If U = I and/or $\frac{\Delta m_{i1}^2 L}{E} \ll 1$ the neutrino oscillation does not show up.

In the simplified scenario of two-neutrino mixing between ν_α, ν_β, there is only one mass-squared difference and the mixing matrix can be parameterized in terms of one mixing angle:

$$U = \begin{pmatrix} \cos\theta & \sin\theta \\ -\sin\theta & \cos\theta \end{pmatrix} \qquad 1.11$$

The resulting transition probability between different flavors can be written as:

$$P(\nu_\alpha \to \nu_\beta) = \sin^2 2\theta \sin^2\left(\frac{\Delta m^2 L}{4E}\right) \qquad 1.12$$

This expression can be also cast in the shape:

$$P(\nu_\alpha \to \nu_\beta) = \sin^2 2\theta \sin^2\left(1.27 \frac{(\Delta m^2 / eV^2)(L / Km)}{(E / GeV)}\right) \qquad 1.13$$

This expression is useful because the results of oscillations experiments are often analysed in first approximation in a two-family scenario. An experiment is characterized by the typical neutrino energy E and by the source-detector distance L. Once these variables are fixed, different values of transition probability are possible, depending on Δm^2 and $\sin^2 2\theta$. The constraints on $P(\nu_\alpha \to \nu_\beta)$ are translated into allowed or excluded regions in the (Δm^2, $\sin^2 2\theta$) plane by inverting expression 1.13.

In order to be sensitive to a given value of Δm^2 , an experiment can be optimised choosing $E / L \approx \Delta m^2 (L \sim L_{osc})$ where $L_{osc} = E / \Delta m^2$. If (E/L) >> Δm^2 (L << L_{osc}) the oscillation does not have enough time to yield a detectable effect because $\sin^2(\Delta m^2 L/E) << 1$.

If (E/L) << Δm^2 (L >> L_{osc}), it is possible to show that the oscillation phase goes through many cycles before the detection and it is smeared out to $\sin^2(\Delta m^2 L/E) = 1/2$ by the finite spread of the energy spectrum and of the source-detector distance.

For null results that set an upper bound on the oscillation probability $P(\nu_\alpha \rightarrow \nu_\beta) \leq P_L$, the excluded region lies always on the upper right side of the (Δm^2, $\sin^2 2\theta$) plane, limited by the followed asymptotic lines (see Figure 1.4):

- A vertical line at $\sin^2 2\theta = 2P_L$, for Δm^2 >> E/L (by setting $\sin^2(\Delta m^2 L/E) = \frac{1}{2}$ on average)
- For Δm^2 << E/L the oscillation phase can be replaced by its first-order expansion and the limiting curve takes the form $\Delta m^2 \sin 2\theta = 4\sqrt{P_L} / (L/E)$

A positive result, i.e. a non-vanishing fraction of oscillated neutrinos, can be used to define a confidence region on $P(\nu_\alpha \rightarrow \nu_\beta)$, which translates to equal probability contours on the (Δm^2, $\sin^2 2\theta$) plane.

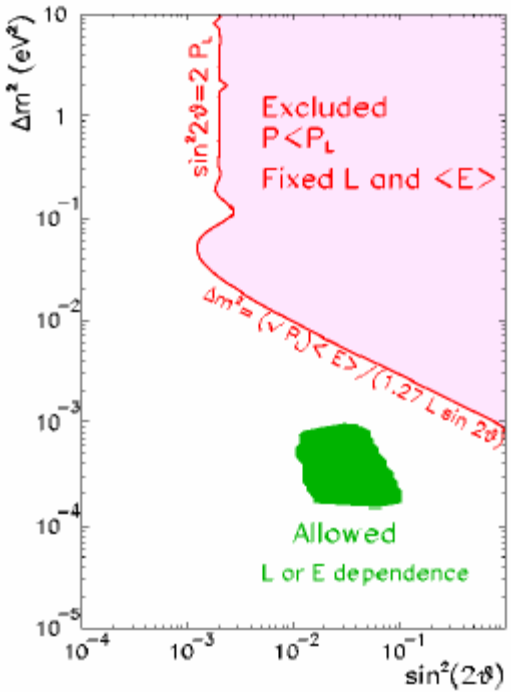

Figure 1.4: The characteristic form of an excluded region from a negative search with fixed L/E and of an allowed region from a positive search with varying L/E in the two-neutrino oscillation parameter plane

1.3. Neutrino oscillation experiments

There are a large number of experiments trying to observe neutrino oscillations. Some rely on man-made sources like nuclear reactors or accelerators; others rely on “natural” sources such as solar neutrinos or neutrinos from cosmic-rays (atmospheric neutrinos).

All of these neutrino oscillation experiments are complementary because they involve neutrinos of different energies travelling over different distances.

The detectors are designed to be large in order to compensate the small neutrino interaction cross sections and are often placed underground to shield the cosmic muons.

The accelerator experiments can be classified into *short-baseline* (SBL) and *long-baseline* (LBL) depending on the source-detector distance. This quantity spans from a few km (in SBL experiments) to hundreds of km (in LBL experiments).

1.3.1. Solar neutrinos

Solar neutrinos are produced by the nuclear fusion process in the core of the Sun, which yields exclusively the electron flavor. These neutrinos are produced with different energies; this is reflected in the design of solar neutrino experiments, each of which probes a specific energy range (Figure 1.5).

The first result on detection of solar neutrinos was announced by Davis in 1968. In the gold mine of Homestake [20], [21] , the solar neutrinos flux was measured for about 30 years and found lower by about 1/3 with respect to predictions of the Standard Solar Model (SSM). The favoured explanation for this deficit is the neutrino oscillations.

The solar neutrinos flux has been measured also by other experiments (GALLEX [22], [23], [24], Kamiokande [25], SuperKamiokande [26], [27] – see Table 1.1), all finding a deficit, but with disagreeing quantitative results. The most complete scenario comes from SNO (Sudbury Neutrino Observatory) in Canada. The experiment measured both the flux of electron neutrinos (CC interactions) [28] and the total flux of all three types of neutrinos (by NC interactions) [29], [30]. The SNO data shows that the SSM is correct, and the Solar neutrino deficit was a result of the oscillation of electron neutrinos into ν_μ and ν_τ, which were below the energy threshold to produce CC interactions. The three-flavor oscillation picture also allows to reconcile the results of almost all experiments, by folding the neutrino production spectra with the L/E oscillation dependence. Neutrino oscillations consistent with solar neutrino observations have been seen using man-made neutrinos from nuclear reactors at KamLAND [31], [32] in Japan. KamLAND has already seen a signal of neutrino oscillations in the so-called Solar neutrino LMA (Large Mixing Angle) mass range.

By combining KamLAND and SNO results with other solar neutrino data (especially that of SuperKamiokande) it is possible to remove ambiguities and estimate two oscillation parameters:

$$\sin^2 2\theta_{12} = 0.314(1^{+0.18}_{-0.15}) \qquad 1.14$$

$$\Delta m^2_{21} = 7.92(1 \pm 0.09) \times 10^{-5} eV^2 \qquad 1.15$$

according to the most recent global fits (see Figure 1.6).

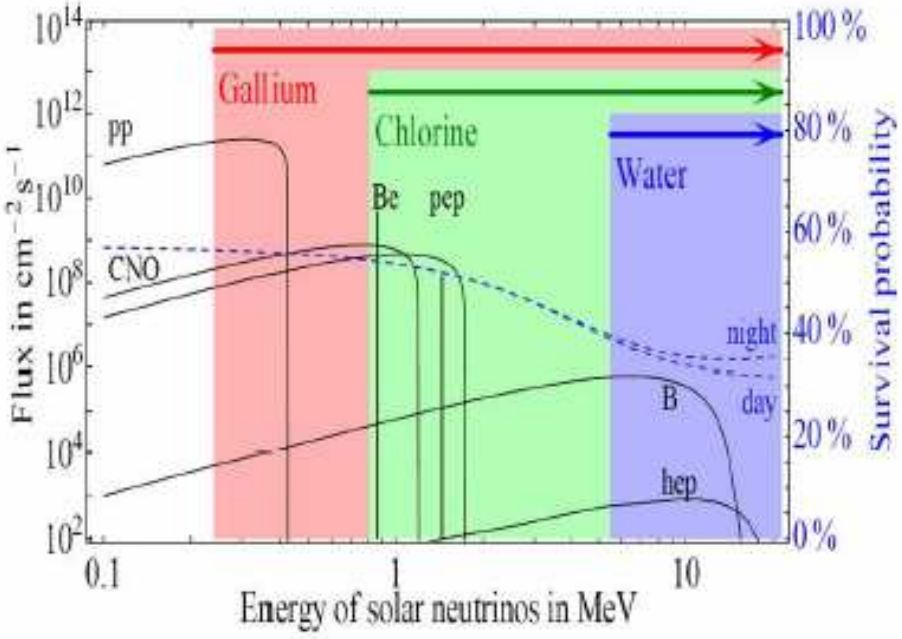

Figure 1.5: The predicted unoscillated spectrum dΦ/dE ν of solar neutrinos, together with the energy thresholds of the experiments performed so far and with the best-fit oscillation survival probability $P_{ee}(E_\nu)$ (dashed line).

Experiment	Flux Measured	SSM	Found/Theory
Homestake	$2.56 \pm 0.16 \pm 0.14$	$7.7^{+1.2}_{-1.4}$	0.33 ± 0.03
Gallium	$77.5 \pm 6.2^{+4.3}_{-4.7}$	129^{+8}_{-6}	0.60 ± 0.006
SAGE	$67.2^{+7.2+3.5}_{-7.0-3.0}$	129^{+8}_{-6}	0.52 ± 0.06
Kamiokande	$2.80 \pm 0.19 \pm 0.33$	$5.15^{+1.0}_{-0.7}$	0.54 ± 0.07
Super-Kamiokande	$2.45 \pm 0.04 \pm 0.07$	$5.15^{+1.0}_{-0.7}$	$0.475 \pm 0.008 \pm 0.013$

Table 1.1: The solar neutrino flux measured by Homestake [21], Gallium [22], SAGE [23], Kamiokande [25] and Super-Kamiokande [27]

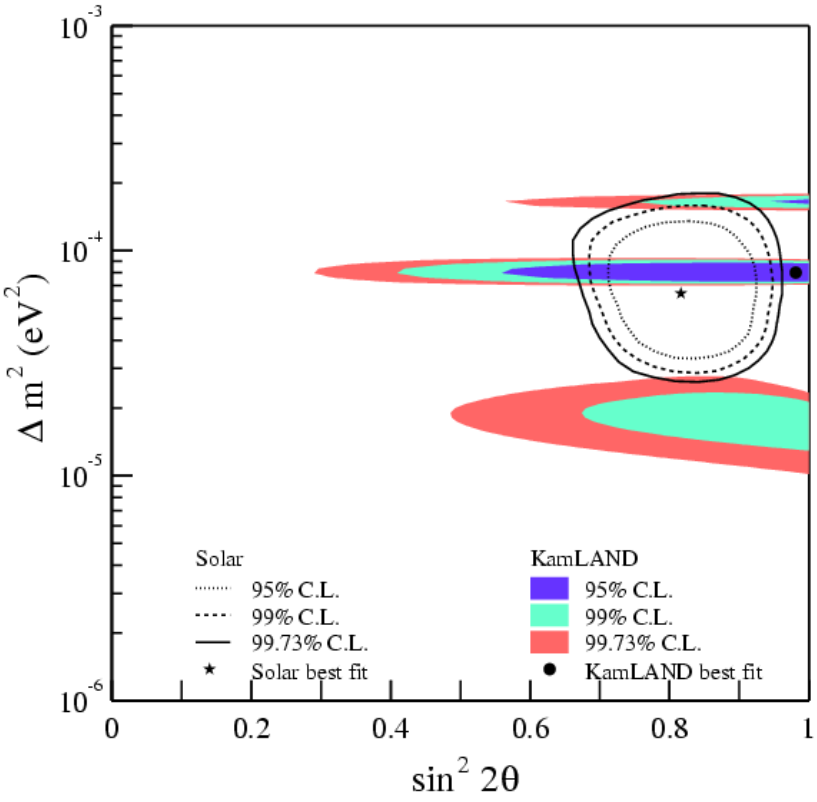

Figure 1.6: Solar and KamLAND oscillation parameter analysis

1.3.2. Atmospheric neutrinos

Atmospheric neutrinos are produced in showers triggered by collision of cosmic rays with the atmosphere of the Earth. Some of the mesons produced in these showers, mostly pions and kaons, decay into electron and muon neutrinos and anti-neutrinos. Since ν_e is produced mainly from the decay $\pi \to \mu \nu_\nu$ followed by $\mu \to e \nu_\mu \nu_e$, one naively expects a 2:1 ratio of ν_μ to ν_e. Absorption in the Earth is negligible in the entire relevant energy range, and therefore a detector located near the surface of the Earth will receive a neutrino flux from all directions.

Atmospheric neutrinos were first detected in 1960's by underground experiments in South Africa [33] and the Kolar Gold Field [34] experiment in India. These experiments measured the flux of vertical muons (they could not discriminate between downgoing and upgoing directions) and although the observed total rate was not in full agreement with theoretical predictions [35], [36], the effect was not statistically significant.

The experiments performed in the 1970's and 1980's, IMB [37] and Kamiokande [25], detected a ratio of ν_μ-induced events to ν_e-induced events smaller than the expected one by a factor of about 0.6. Kamiokande performed separate analysis for both sub-GeV neutrinos and multi-GeV neutrinos which showed the same deficit. This was the original formulation of the atmospheric neutrino anomaly.

Kamiokande also presented the zenith-angle dependence of the deficit for multi-Gev neutrinos. The zenith-angle is defined as the angle between the local vertical direction and the trajectory of the reconstructed charged lepton. Vertically downgoing (upgoing) particles have cosθ = +1(-1); horizontally arriving particles come from cosθ =0 (see Figure 1.7). The Kamiokande result seemed to indicate that the deficit was mainly due to neutrinos coming from below the horizon. Atmospheric neutrinos are produced isotropically at a distance of about 15 km above the surface of the Earth. Therefore neutrinos coming from the top of detector travel approximately 15 km before interacting, whereas neutrinos coming from the bottom of detector traverse the full diameter of the Earth (10^4 km). The Kamiokande distribution suggested that the deficit increases with the distance between the neutrino production and interaction point.

The higher statistics available for SuperKamiokande, along with the confirmations by Soudan2 [38] and MACRO [39], improved the measurement of the deficit, thus yielding tighter confidence regions for the oscillation allowed parameter region.

Super-Kamiokande detects atmospheric neutrinos by their interaction with the nuclei of hydrogen and oxygen in the 22.5 kiloton central fiducial mass of a high-purity water tank. “Fully contained" interactions are those whose final particles stop within the fiducial region. The neutrino flavor is tagged by detecting and identifying the lepton in the final state (muon or electron). In Figure 1.8 the zenith-angle distributions of different samples are shown. Comparing the observed and expected (MC) distributions we can notice that:

- ν_e distributions are well described by the MC while ν_μ show a deficit. Thus the atmospheric neutrinos deficit is due to disappearance of ν_μ rather than appearance of ν_e.
- The suppression of contained μ-like events is stronger for larger cosθ, which implies that the deficit grows with the source-detector distance. This can be described by in terms of up-down symmetry :

$$A_\mu = \frac{U - D}{U + D} = -0.316 \pm 0.042(stat.) \pm 0.005(syst.) \qquad 1.16$$

At present, the most favoured interpretation of this result is that muon neutrinos are oscillating mainly to tau neutrinos. $\nu_\mu \leftrightarrow \nu_e$ is excluded with high CL both because SK results showed that the ν_e contained events are very well predicted by the Standard Model and because explaining the atmospheric data with $\nu_\mu \rightarrow \nu_e$ transitions has direct implications for the $\bar{\nu}_e \rightarrow \bar{\nu}_\mu$ transition. In particular, there should be a $\bar{\nu}_e$ deficit in the CHOOZ [40], [41] reactor experiments (see section 1.3.3), which is excluded by data.

Atmospheric data support maximal mixing, with the following best-fit of two-family oscillation parameters:

$$\sin^2 2\theta_{23} = 1, \qquad \Delta m^2_{32} = 2.6 \times 10^{-3} eV^2 \qquad 1.17$$

The 90% C.L. range for Δm^2_{32} at $\sin^2 2\theta_{23} = 1$ is between 2.0 and 3.2×10^{-3} eV^2. The experimental results in the Δm^2_{32} - $\sin^2 2\theta_{23}$ plane are shown in Figure 1.9. The data set is dominated by SuperKamiokande; results from the long baseline neutrino beam experiments K2K [42], [43] and MINOS [44](see section 1.3.3) are also shown in the same plot.

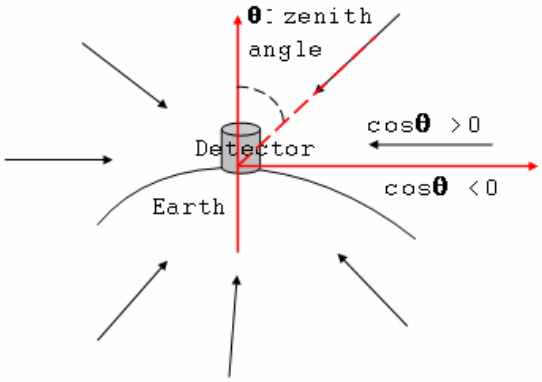

Figure 1.7: Schematic view of the cosmic rays arriving to the Earth

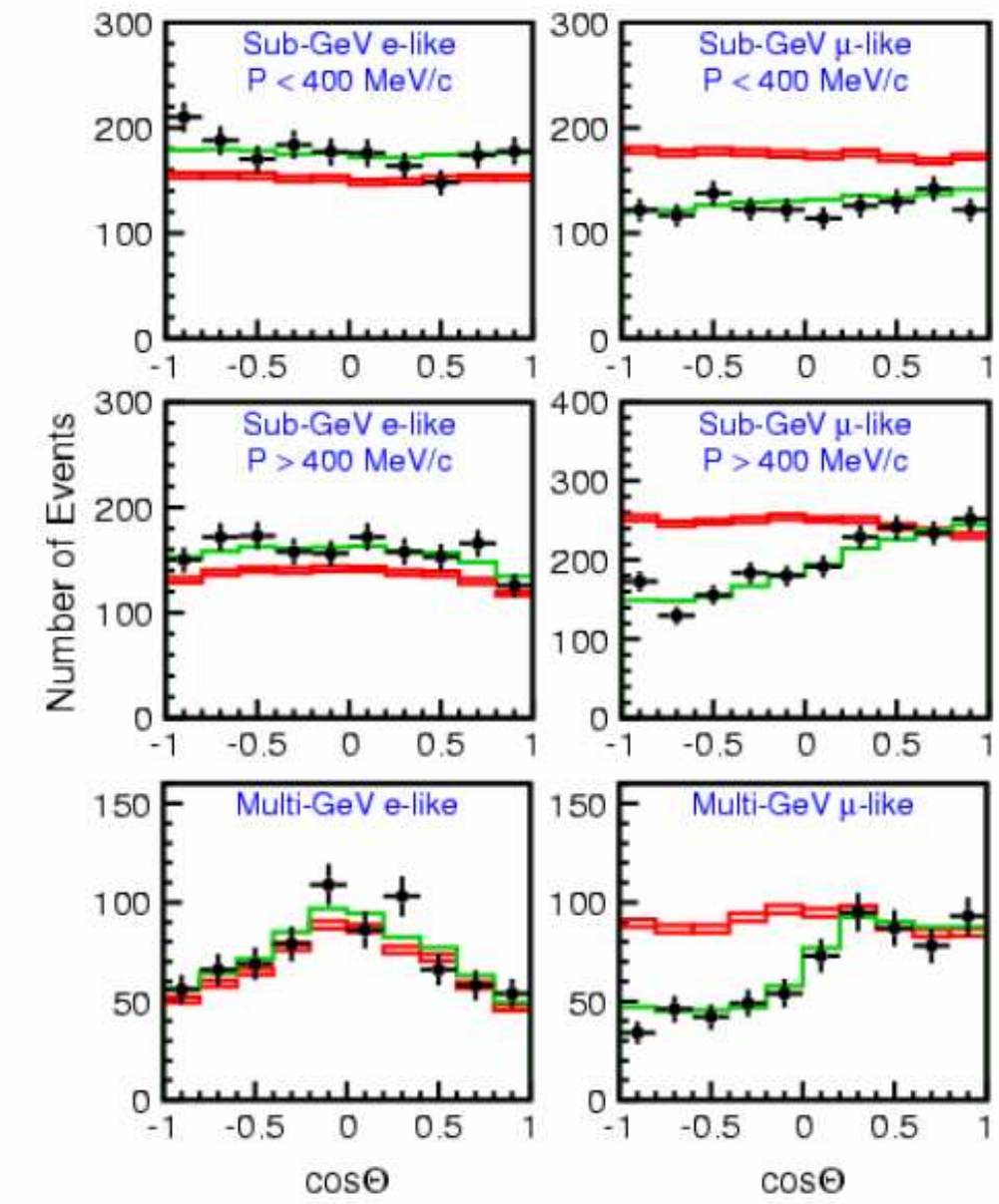

Figure 1.8: Zenith angle distribution of SuperKamiokande 1289 days data samples. Dots, green and red line correspond to data, MC with no oscillation and MC with best fit oscillation parameters, respectively

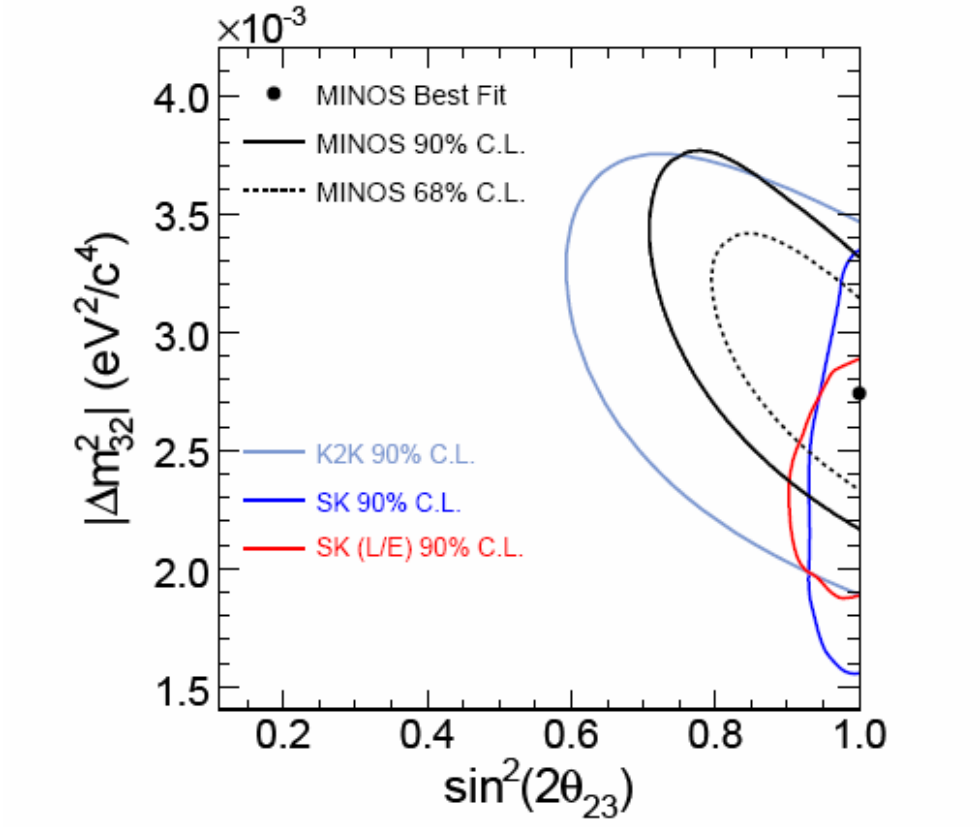

Figure 1.9: The best-fit ranges at 90% CL from SK, K2K and MINOS.

1.3.3. Laboratory experiments

Laboratory experiments to search for neutrino oscillations are performed with neutrinos produced at either accelerators or nuclear reactors. An experiment is characterized by the typical neutrino energy E and by the source-detector distance L (usually called *"baseline"*). The Δm^2 value for which the experiment sensitivity is at its best is tuned by properly choosing L/E. Laboratory experiments have been set up in order to confirm/discard results of solar and atmospheric neutrinos experiments.

Two different approaches are possible: in *disappearance* experiments, one looks for the attenuation of a single-flavoured neutrino beam, due to the mixing with heavier flavours, going undetected because unable to produce CC interactions. In *appearance* experiments, one searches for CC-interactions by neutrinos of a flavour not originally present in a neutrino beam.

1.3.3.a. Nuclear reactor experiments

Nuclear reactor produce $\bar{\nu}_e$ beams with energy of the order of a few MeV. Due to the low energy, electrons are the only charged leptons that can be produced in neutrino CC interactions. If $\bar{\nu}_e$ oscillates to another flavor, its CC interaction cannot not be observed

because the neutrino has not enough energy in the laboratory frame to produce the associated charged lepton. Therefore oscillation experiments performed at reactors are disappearance experiments. They have the advantage that smaller value of Δm^2 can be accessed due to the lower neutrino beam energy. Table 1.2 shows the limits on P_{ee} from the null results of Gosgen [45], Krasnoyarsk [46], Bugey [47] and CHOOZ [40], [41].

In particular, CHOOZ is the first LBL ("*long baseline*") reactor experiment. With a baseline of 1000 m and a mean energy of 3 MeV, CHOOZ is sensitive to the lowest value of Δm^2, so that it can cross-check information from atmospheric neutrinos and the upper sector of the LMA solutions for solar neutrinos. No evidence was found for a deficit in the neutrino flux; this null result translates to exclusion regions in the (Δm^2, $\sin^2 2\theta$) plane shown in Figure 1.10. The 90% CL limits include $\Delta m^2 < 7\times10^{-4} eV^2$ for maximal mixing and $\sin^2 2\theta < 0.10$ for large Δm^2. The CHOOZ results are significant in excluding part of the region that corresponds to the LMA solution of the solar neutrino problem. Furthermore, the CHOOZ bounds rule out with high significance the possibility that $\nu_\mu \rightarrow \nu_e$ oscillations explain the atmospheric neutrino deficit.

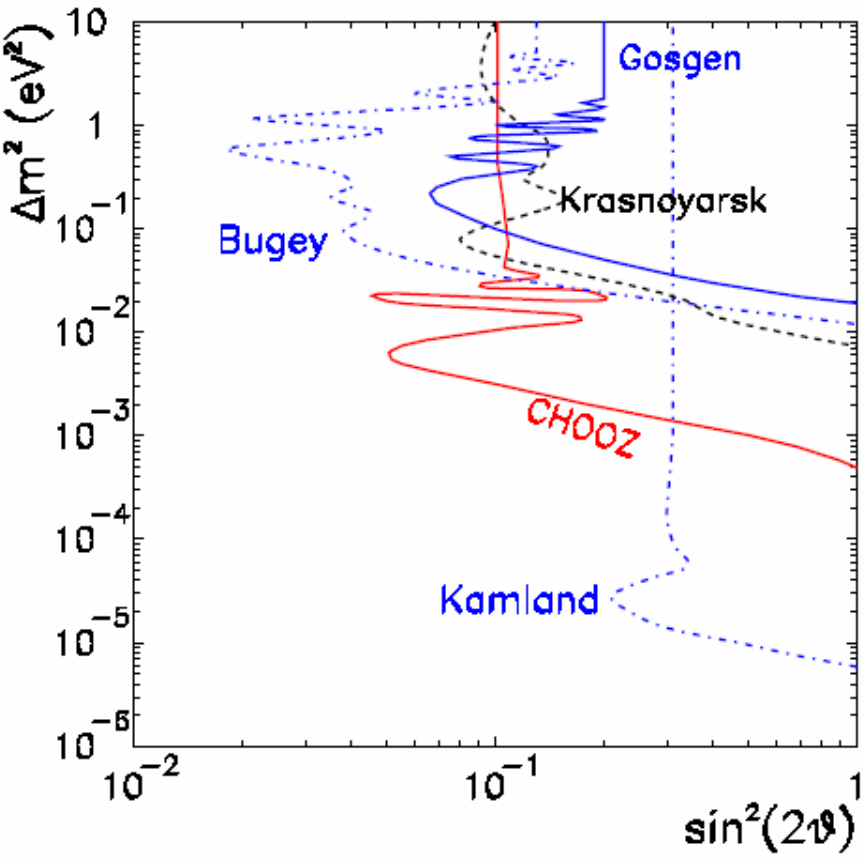

Figure 1.10: Excluded regions at 90% for ν_e oscillations from reactors experiments and the expected sensitivity from the KamLAND experiment.

Experiment	L	Limit	Δm^2_{min} (eV^2)
Bugey	15.40 m	>0.91	10^{-2}
Gosgen	38, 48 , 65 m	>0.9	0.02
Krasnoyarsk	57.230 m	>0.93	7×10^{-3}
CHOOZ	1 Km	>0.95	7×10^{-4}
KamLAND	150-210 Km	>0.85	7×10^{-5}

Table 1.2: 90% CL lower bound on P_{ee} and Δm^2 sensitivity from searches at reactor experiments.

1.3.3.b. Neutrinos from accelerators

Conventional neutrino beams from accelerators are mostly produced by π decay, with the pions produced by the scattering of the accelerated protons on a fixed target (graphite, beryllium..); hadron decays produce muons and muonic neutrinos. The final composition and energy spectrum of the neutrino beam is determined by selecting the sign of the decaying π and by stopping the muons produced in the beam line.

SBL experiments

Most oscillation experiments performed so far with neutrino beams from accelerators have characteristic distances of the order of hundreds of meters (*short baseline* or SBL experiments). Such experiments are not sensitive to the low values of Δm^2 invoked to explain either the solar or atmospheric neutrino but they are relevant for 4-ν mixing schemes.

The CHORUS [53] experiment at CERN searched for $\nu_\mu \leftrightarrow \nu_\tau$ oscillations by looking for τ decays from charged-current ν_τ interactions. The emulsion target of the detector, having a resolution of about a micron, enables the detection of the decay topology of the τ. After having analyzed a sample of 126000 events containing an identified muon and 7500 purely hadronic events, no ν_τ candidate has been found. This result translates in a limit on the mixing angle $\sin^2 2\theta_{\mu\tau} < 8 \times 10^{-4}$ at 90% C.L. for large $\Delta m_{\mu\tau}{}^2$.

The only positive signature of oscillations at a laboratory comes from LSND [48] (Liquid Scintillator Neutrino Detector) which presented the evidence for $\bar{\nu}_\mu \rightarrow \bar{\nu}_e$ at $\Delta m^2 \sim 1$ eV^2. This result cannot be accommodated together with solar and atmospheric neutrino oscillations even in the framework of four-neutrino mixing, in which there are three light active neutrinos and one light sterile neutrino. The region of parameter space that is favoured by the LSND observations has been almost completely excluded by other experiments like KARMEN [49], CCFR [50] and NOMAD [51].

The MiniBooNe [52] experiments searches for $\nu_\mu \rightarrow \nu_e$ oscillations and is specially designed to draw a conclusive statement about the LSND neutrino oscillation evidence.

The first results were shown and published at the beginning of the summer 2007. As shown in Figure 1.11 the LSND 90% CL allowed region is excluded at the 90% CL. The MiniBooNE's results, therefore, rule out a fourth sterile neutrino, thereby verifying the current Standard Model with its three low-mass neutrino species. On the other hand a new anomaly showed up: there were more electron neutrino events detected at low neutrino energies than expected; several possible explanations have been envisaged, the energy spectrum distortion not being compatible with a 3-flavour neutrino oscillation. Further analysis is planned using the MiniBooNE antineutrino sample and a new experiment, MicroBooNE, has been approved at Fermilab to explore this low energy anomaly.

In addition, another experiment, SciBooNE, was set up during the 2007-2008 period, when a second fine-grained detector was placed much closer to the Booster neutrino beam source. SciBooNE will not only allow precision cross section measurements but also can be used as a near detector in conjunction with MiniBooNE to explore muon neutrino disappearance oscillations with better sensitivity.

MiniBooNE represents the first phase for the BooNE experiment, which should use a muon-neutrino beam to determine whether muon neutrinos oscillate to electron neutrinos. In addition to neutrino oscillations. BooNE is also sensitive to other phenomena, such as supernova explosions and the decay of exotic particles.

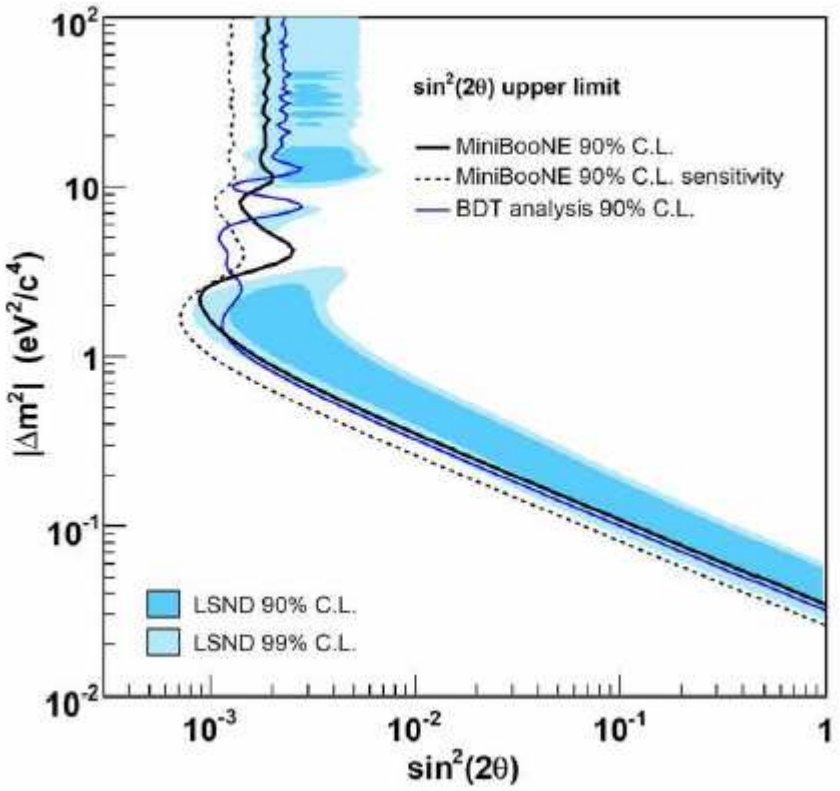

Figure 1.11: The MiniBooNE 90% CL limit and sensitivity (dashed curve) for events with 475 < E_ν^{QE} < 3000 MeV within a two neutrino oscillation model. Also shown is the limit from the boosted decision tree analysis (thin solid curve) for events with 300 < E_ν^{QE} <3000 MeV. The shaded areas show the 90% and 99% CL allowed regions from the LSND experiment.

LBL experiments

Smaller value of Δm^2 can be accessed using accelerator beams for long baseline experiments (LBL). In such experiments an intense neutrino beam from an accelerator is aimed at detector (usually) located underground at several hundred kilometres far away. The minimum goal of these experiments is to test the presently allowed solution for the atmospheric neutrino problem by searching for either ν_μ disappearance or ν_τ appearance.

The first LBL experiment was K2K [54], [55](KEK to Kamiokande): a pure ν_μ beam with mean energy of about 1.3 GeV was sent from KEK to the SK (SuperKamiokande) detector, located L = 250 km away in the Kamioka mine. Since the beam is pulsed, SK can discriminate atmospheric ν_μ from KEK ν_μ. The 2004 K2K results, shown Figure 1.9, are consistent with the expectations based on SK atmospheric data and contain a 4σ indication for oscillations.

The most important K2K result is the energy spectrum: K2K is competitive on the determination of Δm^2_{atm} because, unlike SK, K2K can reconstruct the neutrino energy and data show a hint of the spectral distortion characteristic of oscillations. As a consequence K2K suggests a few different local best-fit values of Δm^2_{atm} , and the global best fit lies in the region suggested by SK.

The running MINOS [44] experiment, showing several similarities to K2K, is designed to detect neutrinos delivered by the Main Injector accelerator at Fermilab (NuMI) with average energies of about 5-15 GeV depending of the beam configuration. Two detectors, functionally identical, will be placed in the NuMI neutrino beam: one at Fermilab and the second one at the Soudan mine, 732 Km away. The near detector allows predicting the non-oscillated flux; the far detector allows to discriminate particles from anti-particles, and to discriminate NC from CC scatterings.

Like K2K data, those from MINOS also contain a hint of the spectral distortion predicted by oscillations (see Figure 1.12) the data disfavour no oscillations by 6.3 standard deviations. The best fit of the data (see Figure 1.13), in the hypothesis of two-flavour oscillations, give:

$$\Delta m^2 = (3.36^{+0.45}_{-0.40}(stat) \pm 0.06(syst)) \times 10^{-3} eV^2 \qquad 1.18$$

$$\sin^2 2\theta = 0.86 \pm 0.11(stat.) \pm 0.01(syst) \qquad 1.19$$

Another LBL experiment is OPERA [56], which is the subject of this thesis. OPERA is designed to search for $\nu_\mu \rightarrow \nu_\tau$ oscillations in the Gran Sasso Laboratory. It will study the interactions of neutrinos with an average energy of 17 GeV, produced at CERN. The goal is to observe the appearance of ν_τ in a pure ν_μ beam.

From the beginning of 2010, the T2K experiment will send a beam of muon-neutrinos from Tokai (on Japan East coast), 300km across the country to a detector at Kamioka. The beam is designed so that it is directed about 2.5 degrees away from the SK detector (it's "off-axis"). The primary goal of T2K is a measurement of θ_{13} through ν_e appearance analysis, in addition to improving current estimates for Δm^2_{23} and θ_{23}

from ν_μ disappearance. In doing this, T2K is also expected to yield an important contribution to the current knowledge of neutrino-nucleon scattering cross-sections.

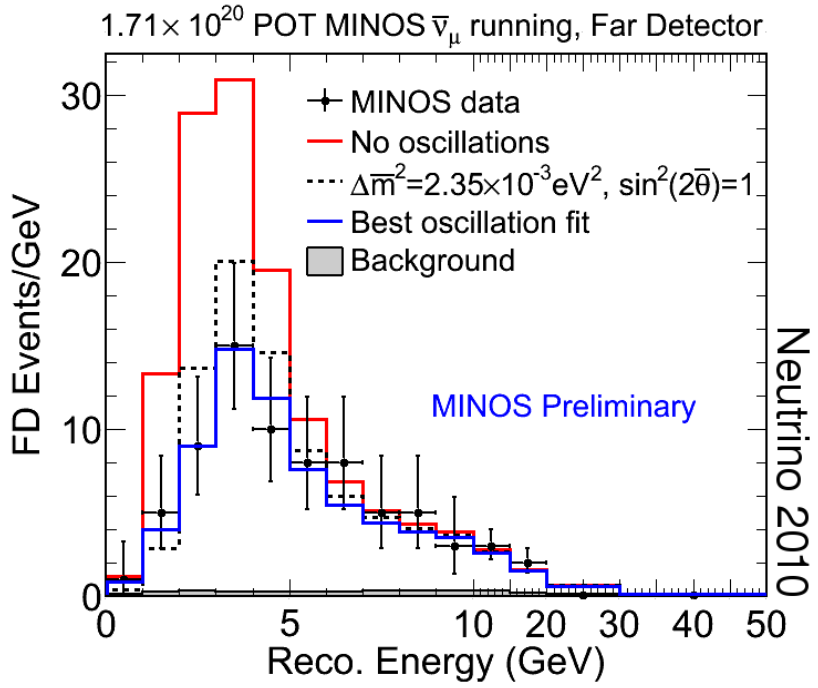

Figure 1.12: This plot compares the events in MINOS Far Detector (black points) to the expected antineutrino energy distribution in the absence of (anti)neutrino disappearance (red histogram). The data disfavour no oscillations at the 6.3 standard deviation level. [57]

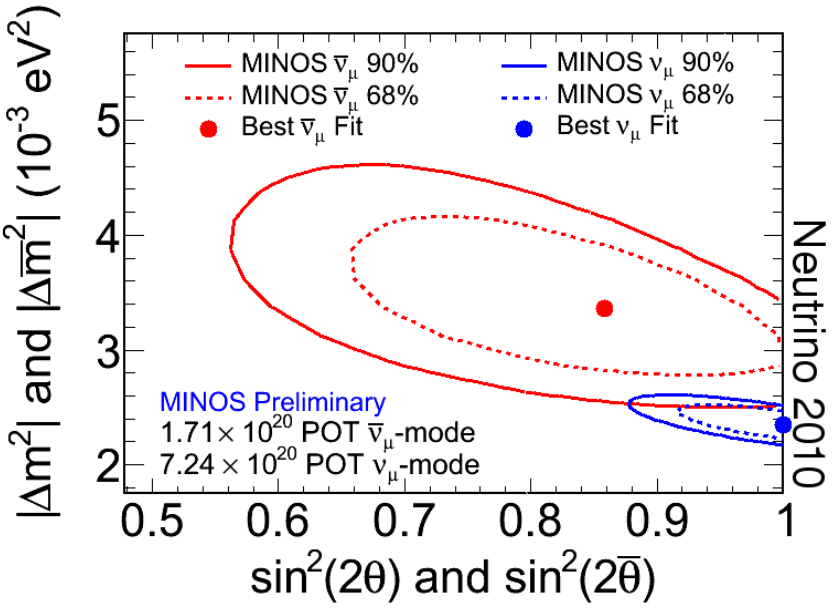

Figure 1.13: Confidence Interval contours in the fit of the MINOS Far Detector antineutrino data (red) to the hypothesis of two-flavor oscillations. The solid (dashed) curves give the 90% (68%) contours. The best fit point is $\Delta m^2=(3.36^{+0.45}_{-0.40}$ (stat.) ±0.06 (syst.))x10^{-3} eV^2 and sin^2(2θ) =0.86 ±0.11 (stat.) ±0.01 (syst.). Also shown are preliminary contours from the MINOS neutrino analysis [57].

1.4. The global oscillation picture

As discussed in the previous sections, neutrino oscillations give no information about the absolute value of the neutrino mass squared eigenvalues m_i^2 (being sensitive only to differences). There are two ordering schemes for neutrino masses that are consistent with the explanation of the atmospheric and solar data as result of neutrino oscillations. The normal (inverted) hierarchy is the one for which the neutrinos separated by atmospheric (solar) mass splitting are heavier than those separated by the solar (atmospheric) mass splitting, as shown in Figure 1.14. As explained in section 1.1.2, the neutrino mixing matrix contains 3 mixing angles: two of them (θ_{23} and θ_{13}) produce oscillations at the larger atmospheric frequency, one of them (θ_{12}) gives rise to oscillations at the smaller solar frequency.

In summary, evidence for neutrino oscillations comes from a wide variety of sources, and the current status of all neutrino oscillation experiments is summarized in Figure 1.15 although this picture is rather crowded, the allowed atmospheric region can be identified by its high value of $\Delta m^2 \approx 2.4\times10^{-3} eV^2$ corresponding to the region labelled "SuperK 90/99 %" in Figure 1.15. The allowed solar region can be identified from its value of $\Delta m^2 \approx 8\times10^{-5} eV^2$, corresponding to the intersection of the upper SNO region with the thin upper KamLAND region in Figure 1.15.

The best world estimates on neutrino masses and mixings from oscillation data are summarised in Table 1.3:.

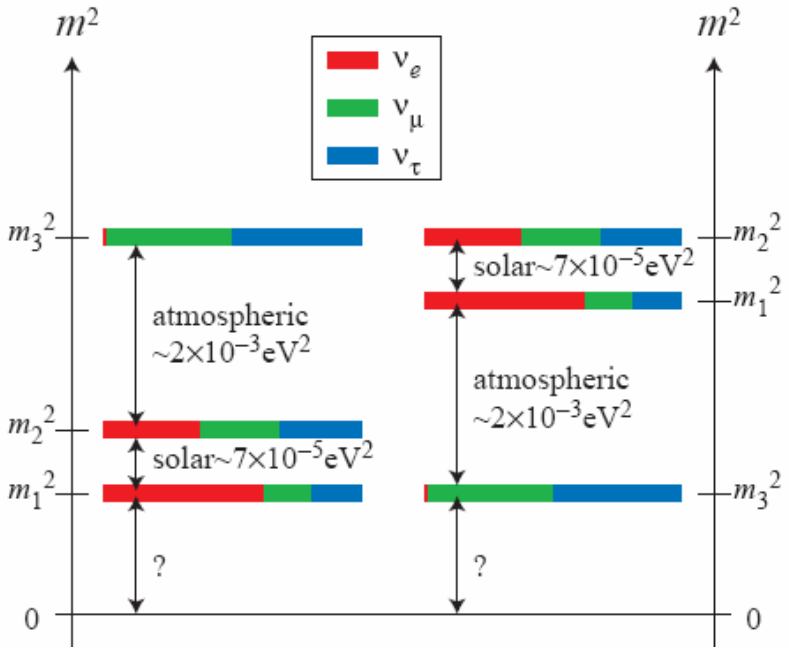

Figure 1.14: Alternative neutrino mass patterns that are consistent with neutrino oscillation explanation of the atmospheric and solar data. The pattern on the left (right) is called normal (inverted) pattern. The coloured bands represents the probability of finding a particular weak eigenstate ν_e, ν_μ, ν_τ in a particular mass eigenstate. The absolute scale of neutrino masses is not fixed by oscillation data and the lightest neutrino mass may vary form 0.0 -0.3 eV.

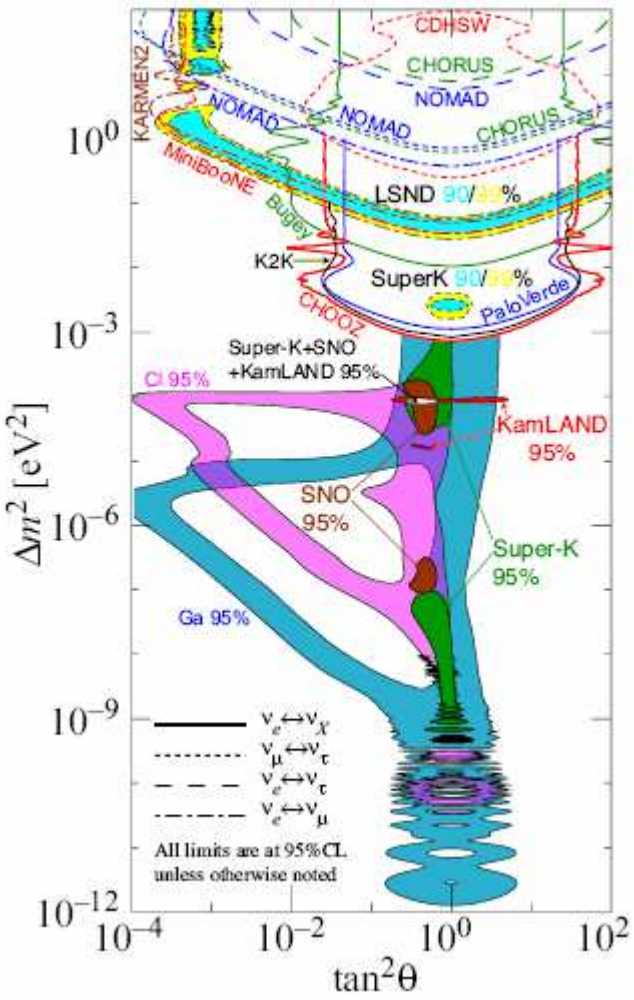

Figure 1.15: The regions of squared-mass splitting and mixing angle favored or excluded by various experiments.

Parameter	Best fit	2σ	3σ	4σ
$\Delta m^2_{21}\left[10^{-5}eV^2\right]$	7.9	7.3-8.5	7.1-8.9	6.8-9.3
$\Delta m^2_{31}\left[10^{-3}eV^2\right]$	2.6	2.2-3.0	2.0-3.2	1.8-3.5
$\sin^2\theta_{12}$	0.30	0.26-0.36	0.24-0.40	0.22-0.44
$\sin^2\theta_{23}$	0.50	0.38-0.63	0.34-0.68	0.31-0.71
$\sin^2\theta_{13}$	0.000	≤0.025	≤0.040	≤0.058

Table 1.3: Best-fit values, 2σ, 3σ and 4σ intervals for the three-flavour neutrino oscillation parameters from global data including solar, atmospheric, reactor and accelerator experimenst.

Chapter 2

The OPERA Experiment

The OPERA (Oscillation Project with Emulsion- tRacking Apparatus) experiment [56] was designed to perform a conclusive test to check the $\nu_\mu \leftrightarrow \nu_\tau$ oscillations hypothesis. It was motivated by results from atmospheric neutrino experiments; hence, its sensitivity covers the Δm^2 region allowed by atmospheric neutrino data. The goal of the experiment is to observe the appearance of ν_τ in an initially pure beam of ν_μ. The observation of even a few ν_τ events will be significant, because of the very low expected background.

In this chapter, the experimental setup and the physical performance of OPERA are briefly described.

2.1. The conceptual design of OPERA

The CNGS, a pure muonic neutrino beam [58], travels from CERN towards the Gran Sasso Laboratory (730 Km away – Figure 2.1 where the OPERA detector is placed. If oscillation occurs, ν_τ interactions are likely to happen; kinematical analysis is performed to discriminate background events (ν_μ CC/NC interactions) from the signal (ν_τ CC interactions). The search for appearance of ν_τ requires the detection and identification of the charged lepton by its decay pattern. Because of its short mean-life (2.9×10^{-13} *s* - $c\tau \sim 87$ μm), a very high resolution tracking device is needed. Nuclear emulsions feature a sub-micron spatial resolution, therefore are suitable for the purpose. This device was used in the CHORUS experiment, which also searched for neutrino oscillations and, later, in DONUT. Unlike CHORUS [53], in which the target was made only of emulsion plates, the OPERA design is based on the Emulsion Cloud Chamber (ECC), a modular structure made of passive plates (lead, in this case) interleaved with

emulsion plates. The so-called *cell*, made of a thin lead plate and emulsion layer, combines the high precision tracking capabilities of nuclear emulsions and the large target mass given by the lead plates. By piling-up 56 cells in a sandwich-like structure one obtains a *brick*; by assembling a large quantity of such modules, it is possible to realise a detector optimised for the study of ν_τ appearance.

This target is complemented with arrays of electronic trackers for the real time determination of the event position and with magnetised iron spectrometers for muon identification and for the estimation of their charge and momentum.

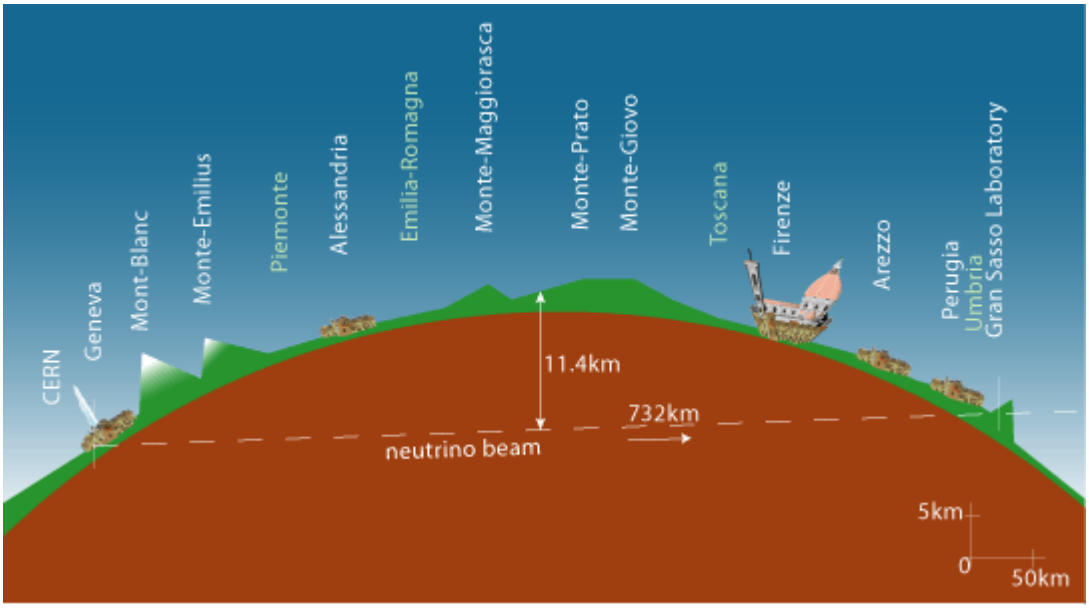

Figure 2.1: Schematic view of the neutrino beam trajectory. The beam is produced at CERN. The detector is located in the Gran Sasso Laboratory, about 730 km away.

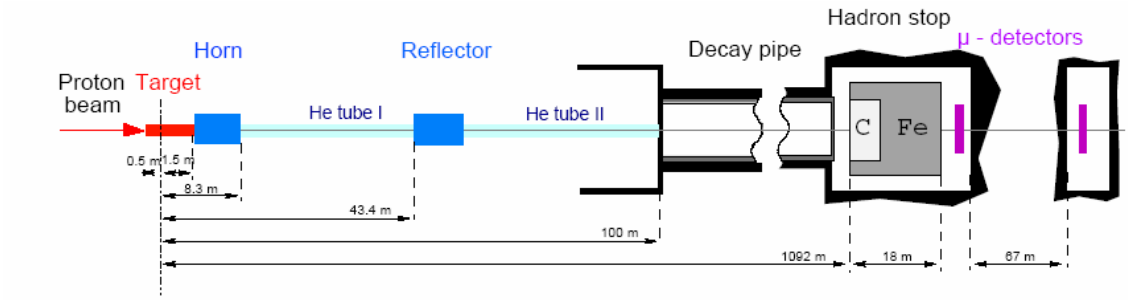

Figure 2.2: Layout of the CNGS beam. The coordinate origin is the focus of the proton beam

2.1.1. Experimental setup

2.1.1.a. The CNGS beam

The CNGS (CERN Neutrino to Gran Sasso) beam [58] is designed and optimised for the study of $\nu_\mu \leftrightarrow \nu_\tau$ oscillations in appearance mode by maximizing the number of charged current ν_τ interactions at the LNGS site.

A 400 GeV proton beam is extracted from the CERN SPS and sent into a target made up of several thin graphite rods. Secondary interaction products (pions and positive kaons) are focused into a parallel beam by a system of two magnetic lenses ("horn" and "reflector").

In a long decay pipe these particles yield muon-neutrinos and muons. The remaining hadrons are absorbed by an iron beam stop. Muons are absorbed further downstream in the rock, while the neutrinos continue to travel to Gran Sasso (Figure 2.2). Due to Earth curvature, the neutrino beam reaches the detector with an angle of about three degrees with respect to the horizontal plane.

Table 2.1 summarizes some beam features. The average neutrino energy at LNGS location is 17 GeV. The $\bar{\nu}_\mu$ contamination is about 2.1 % and the ν_τ-prompt (coming from D_s decay) contamination is negligible. The $\nu_e + \bar{\nu}_e$ contamination is lower than 1% allowing to probe also the sub-dominant oscillation channel $\nu_\mu \leftrightarrow \nu_e$, although with a non-optimised sensitivity. In Figure 2.3 the expected flux (at the LNGS site) of muonic neutrinos is reported.

Assuming a CNGS beam intensity of 22.5×10^{19} p.o.t (protons on target) per 5 year, about 23600 ν_μ CC+ NC interaction are expected and about 205 $\nu_e + \bar{\nu}_e$ CC interaction. In the hypothesis of maximal mixing and $\Delta m^2 = 2.5 \times 10^{-3}$ eV^2 , about 115 ν_τ CC interactions should be produced. Considering the τ detection efficiency (Section 2.2.2) about 10 of them should be detected.

ν_μ (m^{-2}/pot)	7.45×10^{-9}
ν_μ CC events/pot/kton	5.44×10^{-17}
$\left\langle E_{\nu_\mu} \right\rangle$ (GeV)	17
ν_e / ν_μ	0.8%
$\bar{\nu}_\mu / \nu_\mu$	2.0%
$\bar{\nu}_e / \nu_\mu$	0.05%

Table 2.1: Nominal performance of the CNGS reference beam [58-prp]

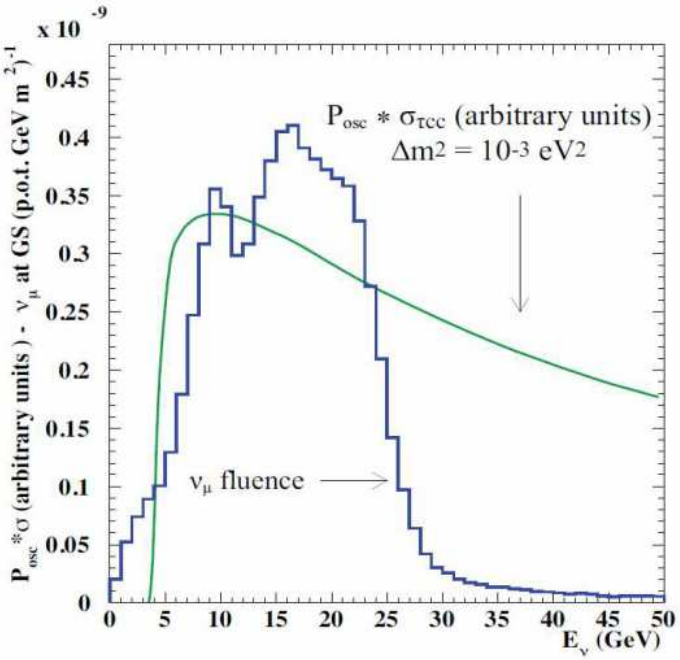

Figure 2.3: CNGS ν - energy spectrum and oscillation probability multiplied by the ν_τ cross section

2.1.1.b. The detector

The OPERA apparatus is a hybrid structure made of electronic devices and nuclear emulsions [59]. The former are needed to select the brick where the interaction took place, to identify the muon tracks and to determine their charge and momentum; nuclear emulsions are used as high-precision tracking planes in the neutrino interaction vertex region.

The OPERA detector has two identical substructures, named *supermodules* (SMs). Each supermodule consists of about 77350 ECC bricks assembled in planar structures called *walls*, orthogonal to the beam direction. Each wall is followed by the two planes of scintillating fibers of the Target Tracker (TT) [60]; a *module* in OPERA terminology is the complex of a brick wall + its two TT planes. A supermodule is made of 29 modules followed by a muon spectrometer (Figure 2.4) [59].

The target

As mentioned above, the OPERA target part is modular; each wall contains about 2668 bricks for a total of 154750 bricks in the whole apparatus. The brick support structure is designed to insert or extracte bricks from the sides of the walls by using an automated manipulator (BMS).

Each brick has transverse dimensions of 10.2 ×12.7 cm^2, a total thickness of about 7.5 cm (corresponding to ~ 10 X_0) and a weight of 8.3 Kg [56]. Its structure is obtained by

stacking 56 lead plates (1-mm thick) interleaved with thin emulsion films. Each film has about 44 μm thick emulsion layers on both sides of a 205 μm thick plastic base[2].

The dimensions of the bricks are set by different requirements:

- each brick should account for a small fraction of the total target mass: when one or more bricks are selected and removed the total mass must not decrease too much;
- transverse dimension should to be larger than uncertainties in the interaction vertex position predicted by electronic trackers;
- the brick thickness must be large enough to allow electron identification thorough EM showers and momentum measurement of hadrons by multiple Coulomb scattering. Electron identification requires about 3 - 4 X_0 and the multiple scattering requires 5÷10 X_0; with 10 X_0, for half of the events such measurements can be done within the same brick where the interaction took place, without the need to follow tracks into downstream bricks.

The Target Tracker strips help restrict the region of the film to be scanned to locate the interaction; they are arranged in two planes oriented along the X and Y directions, close to the wall.

In order to reduce the emulsion scanning load, Changeable Sheets (shortened as CS in the following) were introduced in OPERA [61]. CS doublets are attached to the downstream face of each brick and can be removed without opening the brick. Charged particles from a neutrino interaction in the brick cross the CS doublet and produce a trigger in the TT scintillators. After a trigger, the brick is extracted and its CS doublet is developed and analysed in the scanning facilities at LNGS or in Japan; the information from the CS is used for a precise prediction of the position of the tracks in the most downstream films of the brick, easing track identification and scanback to locate the neutrino vertex point.

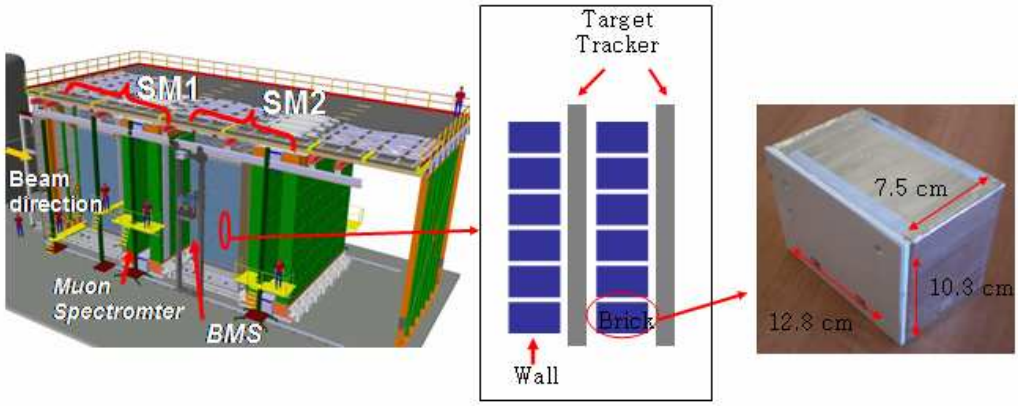

Figure 2.4: Left: schematic drawing of the OPERA detector; Center: sketch of 2 modules; each of them is made of a wall + two Target Tracker planes; Right: real brick picture. CSs sheet are contained in a separate box (white in the image)

[2] More details about nuclear emulsion are reported in the next chapter.

The muon spectrometer

Muon identification, charge assignment and momentum measurement are performed by the muon spectrometers [62]. Each spectrometer consist of a dipolar magnet made of two vertical walls with rectangular cross sections where the magnetic field is approximately uniform. Each wall consist of iron layers interleaved with planes of Resistive Plates Chambers (RPCs) [63], providing tracking inside the magnet, and range measurement of stopping particles.

Drift- tubes (Precision Trackers) are located in front and behind the magnet as well as between the two walls, to measure the muon momentum and for the precise measurement of the muon-track bending.

In order to solve ambiguities in the spatial reconstruction of tracks, each of the drift-tube planes of the PT upstream of the dipole magnet is complemented by an RPC plane with two 42.6° crossed strip-layers called XPCs. RPCs and XPCs also yield a precise start signal to the PTs.

2.1.2. Operation mode

With the CNGS beam on, the data rate from events due to neutrino interactions is in correlation with the beam spill. Because of the long distance from the source, synchronization with the spill is done off-line via GPS. The detector remains sensitive during the inter-spill time and runs in triggerless mode. Events detected out of the beam spill are used for monitoring.

The decision on which bricks need removal after a neutrino interaction is based on information from electronic detectors (see Figure 2.5) [65]. The most likely brick is extracted by BMS and the CS doublet is removed, exposed to X-ray to produce references, then developed to be sent to either CS scanning station (at LNGS and in Japan). The brick is stored underground waiting for CS feedback. If the CS doublet does not show tracks of particles produced in the interaction, another CS is attached to brick, it returns to the detector and the second most likely brick is extracted.

In case of positive result of the CS doublet scanning, the brick is brought to a location at a shallow depth outside the underground hall and exposed to the cosmic muon flux High-energy penetrating tracks provide a pattern for accurate alignment (sub-micron precision) of the emulsion films within a brick. The component of electromagnetic showers in cosmic rays and soft muons are suppressed by a 40 cm iron shield above the bricks [64].

In addition to the X-ray marking performed while the CS box is still in contact with the brick, another set of X-ray marks is added to bricks to be developed before they are disassembled: this set provides a first coarse alignment (about 20 μm precision) without the need to scan any track. The brick is unpacked, each emulsion sheet is labelled with an ID number and developed in an automatic plant. Emulsion films are then sent from the Gran Sasso Laboratory to the scanning laboratories that take care of vertex location and study. Each of them uses one of the two automatic scanning systems, respectively named ESS (European Scanning System) [66] and S-UTS (in Japan) [67], that were developed for OPERA.

Even when the right brick has been extracted for an interaction, the removal of additional bricks, downstream of the one with the primary interaction, may be required for a complete kinematical analysis of decay candidate events.

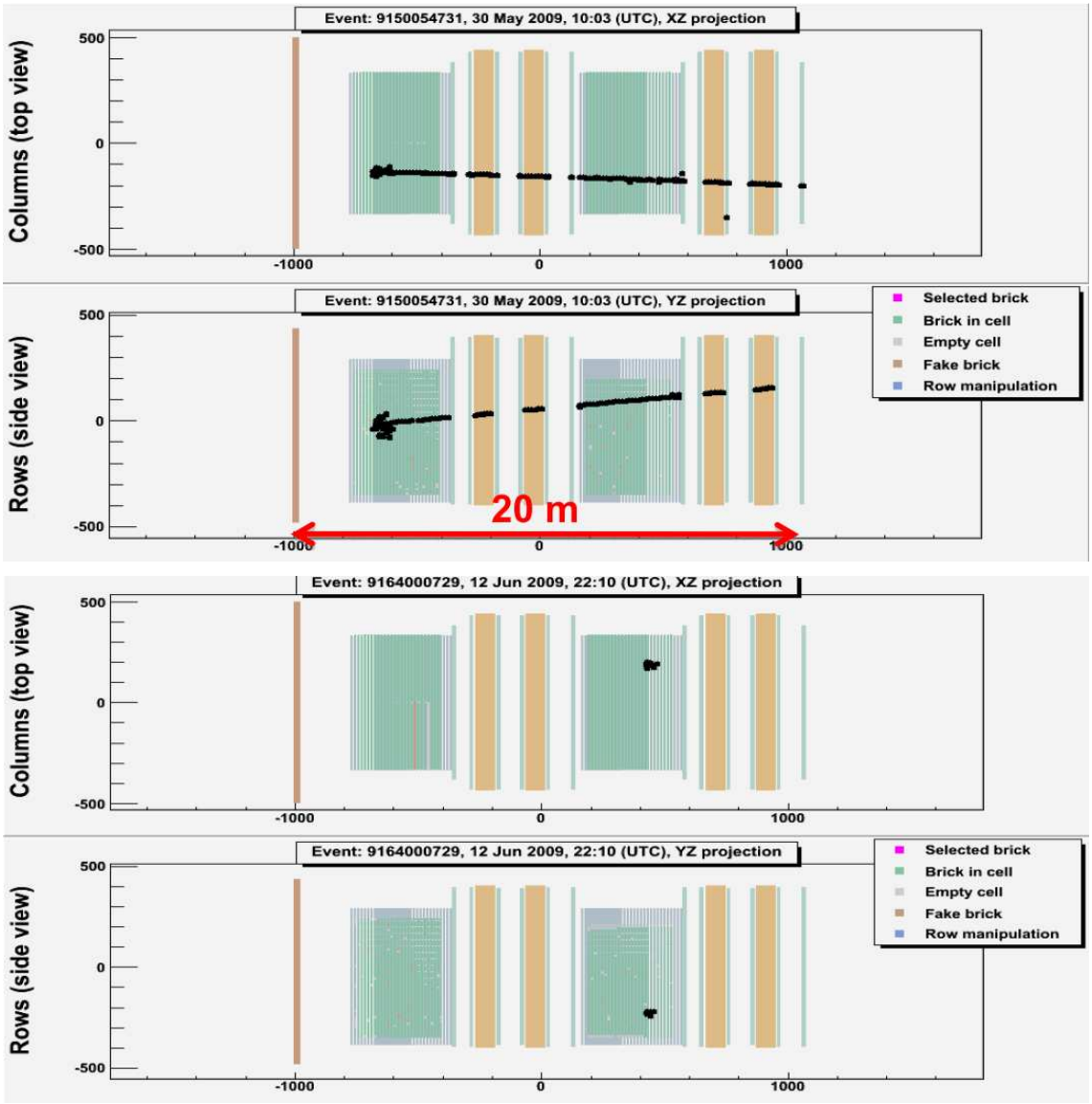

Figure 2.5: Electronic display of tipical ν_μ CC -like (top) and ν_μ NC-like (bottom) events

2.2. Physics Performance

2.2.1. Signal and background

The signal of the occurrence of $\nu_\mu \rightarrow \nu_\tau$ oscillations is the CC interaction $\nu_\tau N \rightarrow \tau^- X$. The τ in the final state is detected through the decay topology and its decay modes to electron, muon or single-prong hadron [56]:

$$\tau^- \rightarrow e^- \nu_\tau \bar{\nu}_e \qquad (B.R.=17.8\%) \qquad 2.1$$

$$\tau^- \rightarrow \mu^- \nu_\tau \bar{\nu}_\mu \qquad (B.R.=17.7\%) \qquad 2.2$$

$$\tau^- \rightarrow h^- \nu_\tau n(\pi^0) \qquad (B.R.=49.5\%) \qquad 2.3$$

The multi-prong hadronic decay channel has been disregarded because of a higher background from hadronic interactions The single-prong decay is characterized by a *kink* topology.

The criterion used to select a *kink* candidate is independent of the τ decay channel, but it depends on where decays occur. τ decays can be classified as *short* or *long* depending on the decay vertex position with respect to primary vertex (Figure 2.6).

Short decays take place in the same lead plate where the primary vertex is found (about 60%). In this case, there is no chance to reconstruct the parent track and an impact parameter method is applied. The track that is candidate to be a τ-decay daughter is selected and if its impact parameter with respect to the measured primary vertex is larger than a given value (10 micron) a *short kink* topology has been found and a more accurate analysis has to be performed.

Long decays are events in which the τ track is long enough to exit the lead plate where the primary vertex occurs. In this case, at least one film is measured also for the parent track. The topology is considered "interesting" if parent and daughter track cross (within measurement errors), giving significant *kink* angle. The angular resolution of 2.1 *mrad* in one emulsion film implies a minimum detectable kink angle of 3.0 *mrad*. Events with $\theta_{kink} \geq 3 \times 3.0$ *mrad* = 9.0 *mrad* [56] are selected, and they undergo further analysis (which may also include further scanning).

Several techniques are used to define the nature of daughter track. In the electronic channel, the daughter is identified through the electron showering in the ECC. The main background source are charm decays in electronic channel with an undetected primary muon (see Figure 2.7 A)

For the muonic decay mode, the presence of a penetrating (and often isolated) track allows easy identification of the muon attached to the decay vertex. In this case, the background comes from large angle scattering of muons produced in ν_μCC interactions

and from muonic decay of charm particles in the case in which the muon at the primary vertex goes undetected and muon charge assignment is wrong (Figure 2.7 B).

Hadronic decay modes have the largest branching ratio, but they are affected by high background sources:

- One-prong decays from charm particle (with muon at primary vertex undetected) - see Figure 2.7 C.
- Hadron reinteractions (see Figure 2.7 D). In a ν_μCC event in which muon is undetected or in a ν_μNC event, a hadron from primary vertex may interact in the lead plate closest to primary vertex. If the other products of this interaction are not detected, the topology found is similar to the CC – single prong decay of the τ.

Table 2.2 reports the expected background for different decay modes normalized to 10^6 DIS events.

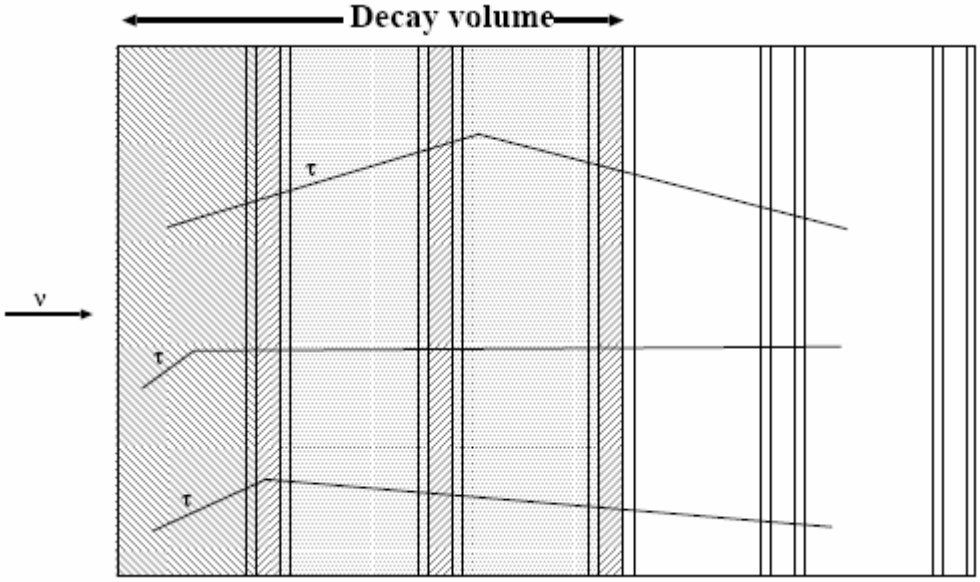

Figure 2.6: Different decay topologies; short decay (left-hatched region); long decays in base (right-hatched region); long decays outside the base (shaded region); very long decays (white region), not shown.

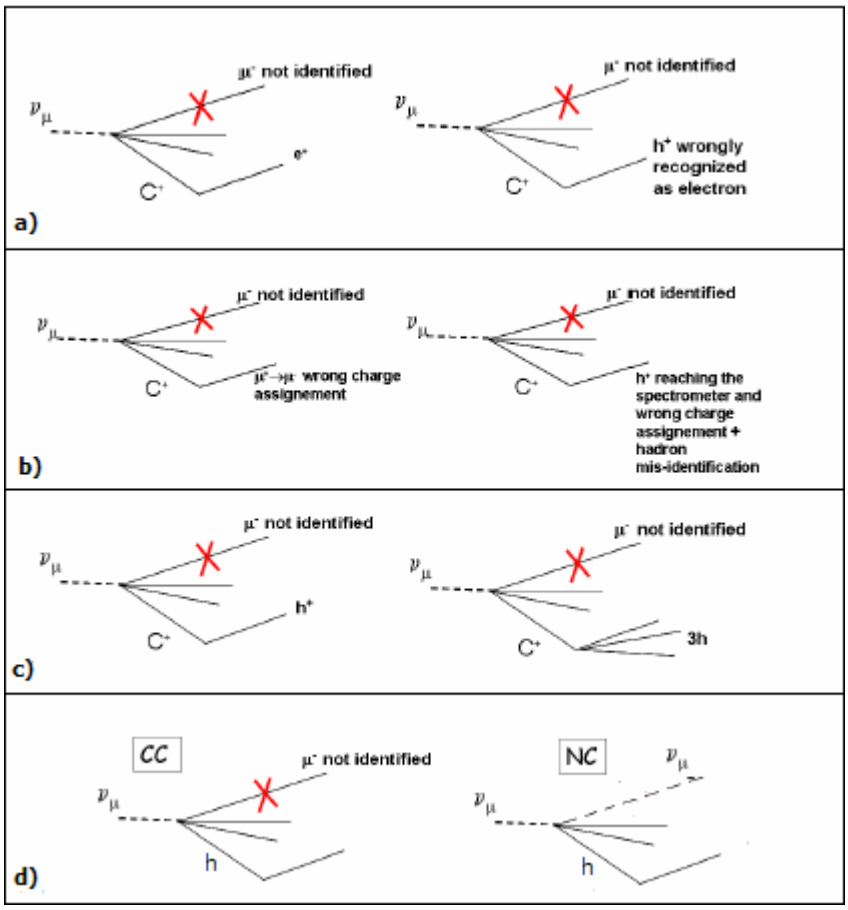

Figure 2.7: Example of charmed particles decay A) electronic channel background B) muon channel cackground C) Hadron channel decay D) Example of hadronic reinteraction in CC and NC events

	$\tau \to e$	$\tau \to \mu$	$\tau \to h$	Total	Error
Long: charm	7.0	1.4	7.0	15.4	±15%
Long: ν_eCC and π_0	0.2	-	-	0.2	±10%
Long: μ scatt	-	5.0	-	5.0	±50%
Long: had. reint.	-	-	5.0	5.0	±50%
Long total	7.2	6.4	12.0	25.6	-
Short: charm	1.1	-	(1.3)	1.1	±15%
Short: ν_eCC and π_0	0.1	-	-	0.1	±10%
Short: had. reint.	-	-	(6.1)	(6.1)	-
Short total	1.2	-	-	1.2	-
Total	8.4	6.4	12.0	26.8	-

Table 2.2: Expected background for different channels. The numbers are normalised to 10^6 DIS events [56].

2.2.2. Tau detection efficiency

The signal detection efficiency reported in this section was estimated on the basis of tests and simulations performed in 2000, when the OPERA project was proposed [56]. Several of these numbers need to be re-determined in the following years.

Below are listed the factors involved in efficiency evaluation:

- trigger and brick finding efficiencies (related to electronic detectors only);
- geometrical acceptance and vertex location efficiencies (related to the procedures to find the interaction vertex in emulsion sheets);
- kinematical efficiencies (cuts are studied *ad hoc* to discriminate signal and background, depending on the decay channel and background source).

Table 2.3 reports the kinematical efficiency for different decay modes, topologies and type of events.

	$\varepsilon_{kin}^{L}(DIS)(\%)$	$\varepsilon_{kin}^{L}(QE)(\%)$	$\varepsilon_{kin}^{S}(DIS)(\%)$
$\tau \to e^-$	83	84	22
$\tau \to \mu^-$	78	76	-
$\tau \to h^-$	20	28	(2.9)

Table 2.3: Summary of the kinematical efficiencies for different tau decay modes, topologies (long and short) and type of events (DIS and QE). The value given in brackets does not contribute to the sensitivity evaluation [56].

τ decay channel	B.R. (%)	Signal	Background
$\tau \to e$	17.8	3.5	0.17
$\tau \to \mu$	17.7	2.9	0.17
$\tau \to h$	49.5	3.1	0.24
$\tau \to 3h$	15.0	0.9	0.17
All	B.R * eff = 10.6 %	10.4	0.75

Table 2.4: Expected number of tau and background events collected by OPERA in five years' data taking. Signal events are computed for full mixing and for $\Delta m^2 = 2.5 \times 10^{-3}$ eV^2[56]

2.2.3. Sensitivity to oscillations and discovery potential

The sensitivity of the experiment was evaluated using the efficiency shown in Table 2.3 and the background shown in Table 2.2. The energy dependence of the neutrino spectra and of the detection efficiencies is taken into account. The conventional two-flavour approximation is assumed.

Under the assumption of five years' running in the CNGS beam, operated in shared mode (with other beams) and with nominal beam intensity (4.5×10^{19} pot/year), OPERA is expected to collect the number of signal and background events listed in Table 2.4. The reported values are computed assuming $\Delta m^2 = 2.5 \times 10^{-3}$ eV^2 and the hypothesis of maximal mixing. Each channel has been weighted by its branching ratio. In this case the background/signal ratio is about 0.072.

Figure 2.8 gives, as function of background/signal ratio, the minimum number of events to be observed to claim for a 3σ (red points) or 4σ (blue points) evidence of oscillation in OPERA. Such values are obtained assuming $\Delta m^2 = 2.5 \times 10^{-3}$ eV^2 and maximal mixing.

In Figure 2.9 the OPERA discovery probability (in five years' run) is shown as a function of different values of Δm^2. The target mass reduction with respect to the experiment Proposal has been taken into account.

Figure 2.10 shows the sensitivity of the OPERA experiment to $\nu_\mu \rightarrow \nu_\tau$ oscillation together with the region allowed by the past atmospheric neutrino experiments: the OPERA sensitivity completely covers the allowed region.

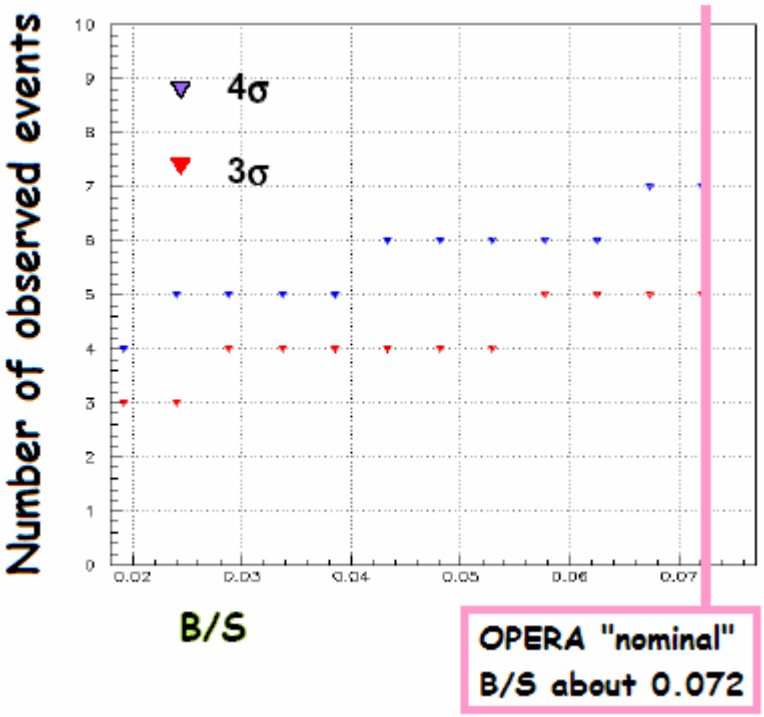

Figure 2.8: Number of observed event by OPERA in five years' running vs. background/signal ratio [68].

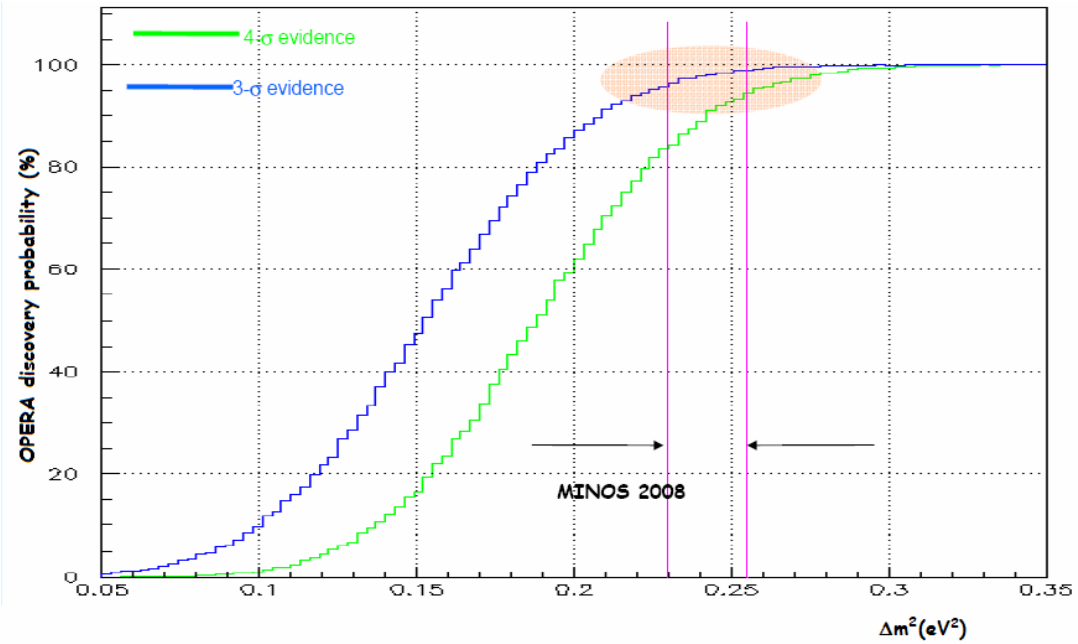

Figure 2.9: OPERA discovery probability as a function of different values of Δm^2[68]

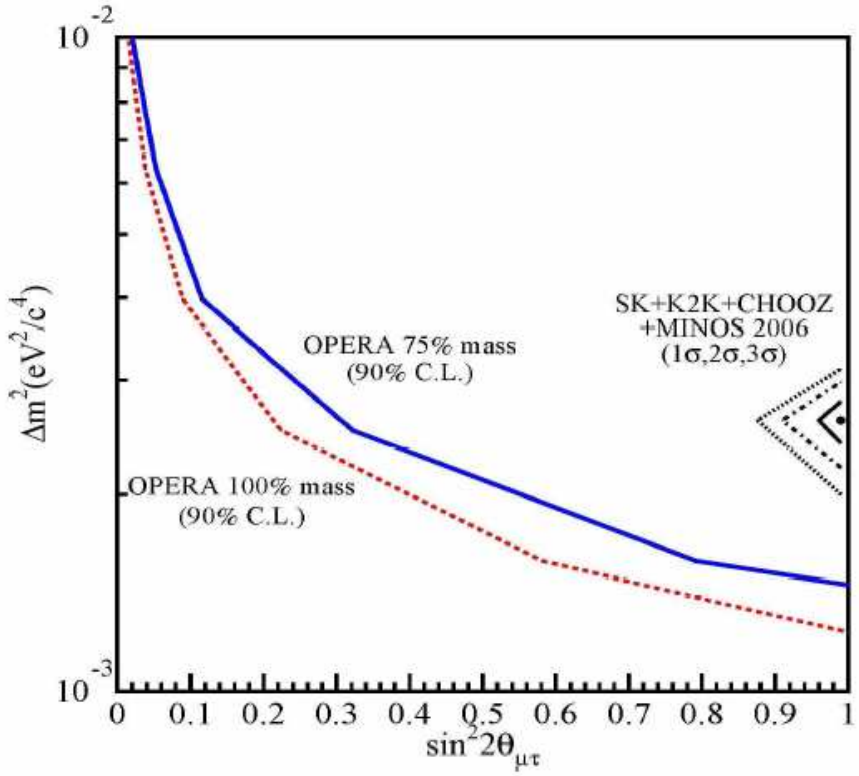

Figure 2.10: The OPERA sensitivity to $\nu_\mu \rightarrow \nu_\tau$ oscillations [56].

Chapter 3

Searching for neutrino interactions

Neutrino interactions registered in OPERA electronic detector are recorded in emulsion sheets, which are the sensing part of target. In order to obtain information about event topologies and kinematics, nuclear emulsion have to been read out. This is the goal of scanning laboratories, where several kinds of information about neutrino interaction are collected.

In order to cope with the daily analysis of the large number of emulsion sheets associated with neutrino interactions, very fast automatic scanning systems have been developed: the European Scanning System (ESS) [66] and the S-UTS in Japan [67]. The main features of these systems are: high speed, micrometric precision, high tracking efficiency and low instrumental background.

This chapter briefly describes the European Scanning System and the procedures to be applied for the location of neutrino event.

3.1. Scanning system: hardware and software

An automatic scanning system has to be able to execute all tasks usually performed by an human operator. Human eyes are replaced by a camera installed on a microscope. Motion on emulsion plates is accomplished by a workstation hosting a motor controller; a dedicated software allows to recognise and reconstruct tracks showing the particle passage.

3.1.1. Nuclear emulsions

Nuclear emulsions are devices able to record charged particles; their working principle is similar to the one of photographic films. They are a mixtures of silver halide micro-crystals (typically AgBr) and a gel consisting mainly of a variable quantity of water, a small amount of glycerol and possibly other organic substances.

Two emulsion layers, 43 μm thick, coat both sides of a 205 μm thick triacetate base (see Figure 3.1). A thin (~ 1 μm) protective film (gelatine) protects both emulsion layers to avoid chemical reaction between lead plates and the silver ions contained in emulsion layer.

The energy released by ionizing particles to the crystals produces a *latent image* that has a very long lifetime. Development makes such sensitized sites grow to grains of metallic Ag; fixing and washing remove the undeveloped crystals, the gel becomes transparent and by using a transmission optical microscope it is possible to see the paths of charged particles, showing up as sequences of dark silvers grains on a light background.

The average diameter of developed silver grains in the OPERA emulsions is ~0.5 μm. A minimum ionizing particle (MIP) yields about 30 grains per 100 μm; a sequence of grains in an emulsion layer is usually named "microtrack". The average residuals of the positions of microtrack grains with respect to a straight-line fit average to 55 nm; the spatial resolution of the microtrack fit is about 0.3 μm. Such resolution is suitable to detect the τ through the observation of their kink decay topology [69].

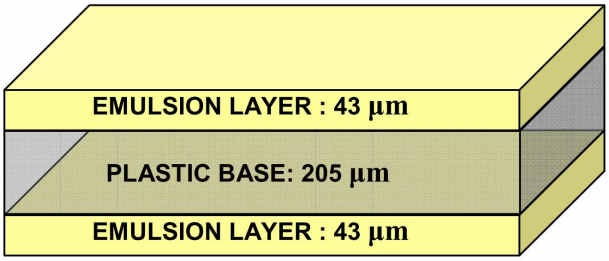

Figure 3.1: OPERA nuclear emulsion: two emulsion layers coat both sides of a triacetate transparent base.

3.1.2. Particle track reconstruction

The working principle is common to the two automatic scanning systems (ESS and S-UTS) used in OPERA. They both consist of:

- Computer-driven horizontal and vertical stage equipped with high-speed precision mechanics
- Custom optics providing achromatic images with small field depth
- High resolution and high frame-rate camera interfaced with a frame-grabber and vision processor.

In the European Scanning System, bi-dimensional imaging and tri-dimensional tracking is obtained by software; the S-UTS uses algorithms coded in the hardware of custom processors.

By adjusting the focal plane of the objective lens within an emulsion layer, a sequence of tomographic images of each field of view is taken at equally spaced depth levels; it is processed and analysed in order to recognise aligned grains produced by charged particles along their trajectories. Each 43 μm thick OPERA emulsion layer is spanned by 15 tomographic images with a pitch about 3 μm, accounting for the effective focal depth of the system [70].

The reconstruction of particle tracks in OPERA bricks takes three steps: micro-tracking, base-track reconstruction and volume tracking.

3.1.2.a. Micro-tracking

A geometrical alignments of grains detected in different levels within the same emulsion layer is named a micro-track. Starting from a pair of grains, more aligned grains are appended. A lot of time is required to examine all combinations of aligned grains in emulsion, and proper cuts are needed to discriminate random alignments from particle trajectories. Hence, two further criteria are used to selected interesting tracks. First, only tracks with $\tan\theta < 1$ (θ is the angle between the reconstructed micro-track and z direction) are selected because tracks produced in neutrino interactions are more likely to be produced close to the neutrino beam; second, given the sensitivity of the OPERA emulsion (about 30 grains/100 μm for m.i.p.'s), the number of grains of tracks in a 43-μm thick emulsion layer is a Poisson distribution with an average of 13; micro-tracks with less than 6 grains are likely to be just random alignments, while 96% of micro-tracks from m.i.p.'s exceed this cut. For each micro-track, a straight-line fit provides position and slopes.

Random alignment of grains ("*fog*") are possible because of the statistical nature of emulsion developing process: sensitized grains develop faster, but the probability for an untouched grain to develop does not vanish. Another background source comes from tracks recorded during transport to the experimental or repository area. A thermal cycle called *refreshing* deletes about 1/3 of grains sensitized before exposure to the neutrino beam, hence increasing the probability that such m.i.p. tracks be discarded by the cut on the minimum number of grains.

3.1.2.b. Base-tracks reconstruction

Minimum ionising particles have enough energy to cross an OPERA plate; hence, one expects micro-tracks to come in pairs that can be linked the plastic support; such pairs are called base-tracks (see Figure 3.2). This significantly improves the signal to noise ratio and increases the precision of track angle reconstruction by minimising distortion effects.

Each micro-track is extrapolated to the corresponding Z level of the opposite base-emulsion interface and position and slope tolerances are applied to select correlated pairs. One usually computes the following quantity:

$$\sigma = \sqrt{\left(\frac{\Delta s_{t\perp}}{s_{\perp tol}}\right)^2 + \left(\frac{\Delta s_{t\parallel}}{s_{\parallel tol}}\right)^2} + \sqrt{\left(\frac{\Delta s_{b\perp}}{s_{\perp tol}}\right)^2 + \left(\frac{\Delta s_{b\parallel}}{s_{\parallel tol}}\right)^2} \qquad 3.1$$

where $\Delta s_{t\perp}$ /$\Delta s_{t\parallel}$ is the transverse/longitudinal slope difference between the top/ bottom micro-track and base-track and $s_{\perp tol}$ ed $s_{\parallel tol}$ is the corresponding tolerance ($s_{\perp tol}$ =0.04 and $s_{\parallel tol}$ = 0.04+0.3 × S). Two populations emerge from the sample (see Figure 3.3): one with large σ value and a number of grains clearly incompatible with the Poissonian law (*fake* base-tracks, top-left); the other one with small value of σ and a number of grains well within the Poissonian expectations (bottom-right). The cut represented by dashed line is applied to remove the fake base-tracks.

The resulting base-track efficiency is above 90%, over the angular range [0÷700] mrad and micro-track finding efficiency is above 95%. Correspondingly, the instrumental background is estimated to be about 1 fake base-track/ cm^2 [66] for fog < 8 grains / 1000 μm^3.

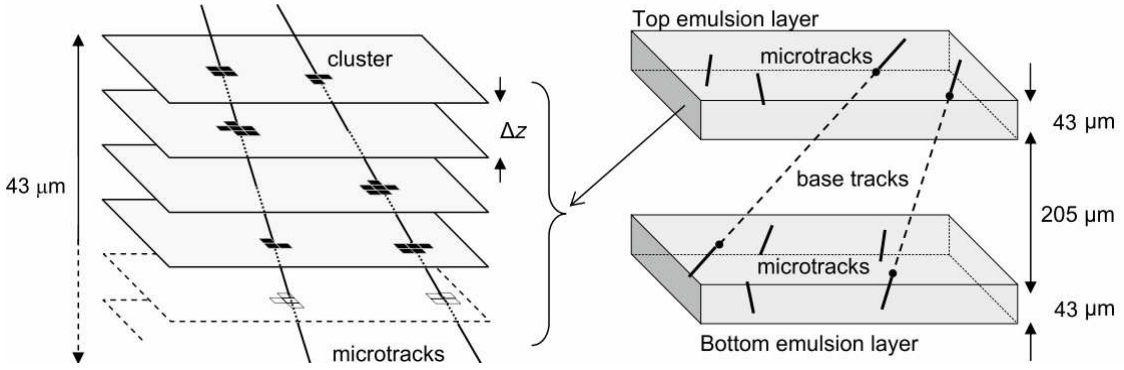

Figure 3.2: Reconstruction of a micro-track (left) and of a base track (right).

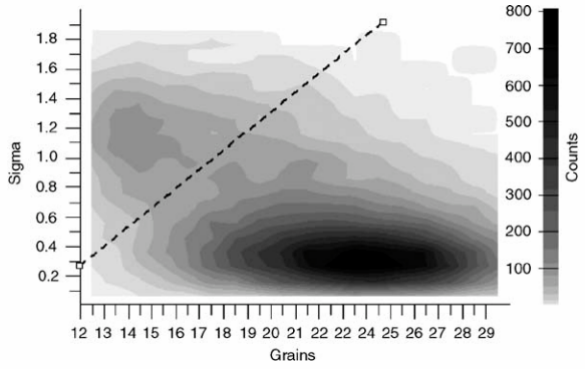

Figure 3.3: Rejection of fake base-track based on the slope agreement within the two micro-tracks (sigma) and the number of grains: the cut represented by the dashed line is applied

3.1.2.c. Volume track reconstruction

The reconstruction of particle tracks in OPERA bricks requires connecting base-tracks in several consecutive films. The crucial point of this procedure is the alignment between two consecutive plates (intercalibration). The emulsion plate intercalibration is done by performing a pattern recognition between base-tracks of two consecutive emulsion films (see Figure 3.4).

Emulsion plates are not rigid objects; the simpler mapping model between two plates that can be used over a 1 cm scale, with the precision of a few micron, is an affine deformation. The mechanical accuracy of film piling in brick assembly is indeed of 50÷100 μm, much worse that the achievable precision. Furthermore, emulsion films are affected by environmental conditions (temperature and humidity) altering their original geometry. The task of producing a set of alignment tracks for film alignment is accomplished by exposing each brick to a controlled flux of cosmic rays before disassembly. The cosmic ray spectrum is hardened by two iron shields placed just above the bricks, which remove soft particles, mainly electrons from showers.

The most general affine transformation that allows to align two consecutive films is:

$$\mathrm{X}_2 = A \cdot \mathrm{X}_1 + \mathrm{T} = \begin{bmatrix} axx & axy & 0 \\ ayx & ayy & 0 \\ 0 & 0 & 1 \end{bmatrix} \cdot \begin{bmatrix} x_1 \\ y_1 \\ z_1 \end{bmatrix} + \begin{bmatrix} dx \\ dy \\ dz \end{bmatrix} \qquad 3.2$$

where X_2 and X_1 are, respectively, the position coordinate after and before the transformation [71].

By applying the above procedure to each pair of consecutive films, relative displacements can be reduced to the level of a few μm, adequate to follow a track film-by-film while avoiding ambiguities and random background (see Section 3.2.3). The achievable precision mainly depends on the number of penetrating tracks, and the area of the measured zones. The density of passing tracks should be low enough to avoid spoiling the topological and kinematical reconstruction of neutrino events; on the other hands scanning time is a critical issue and needs to be minimised. Typically a density of the order of a few tracks/mm^2 and a scanning surface of several mm^2 are a reasonable compromise between these two conflicting requirements.

Once films have been aligned plate-by-plate, volume tracks are reconstructed. Volume tracks can be built out of base tracks only, or mixing base tracks and micro-tracks (if one micro-track is missing on one layer of a plate, the base track cannot be formed, thus reducing the efficiency). Plate-to-plate linking is performed with proper position and slope tolerance. Scattering information can be used to define whether to allow wide or tight tolerances: over the length of several plates, the slope difference may range from a few mrad to 50 or more, depending on the particle momentum.

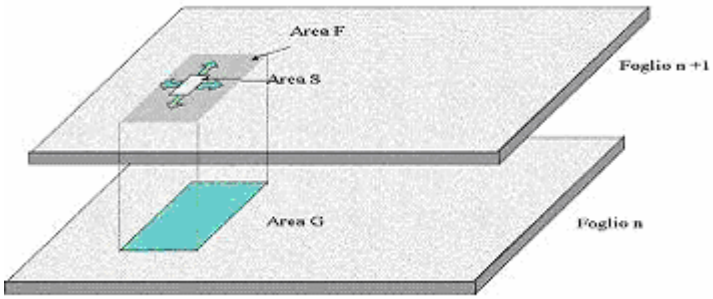

Figure 3.4: Scheme of the alignment process: on sheet n the G area is fixed, and on sheet n+1, the S area is moved several times around within the F area searching for the translation that yields the maximum number of matching tracks.

3.2. Vertex Location

The event location strategy applied for the analysis of the OPERA bricks can be sketched in the following steps:

- Changeable Sheet (CS) scanning
- CS-to-brick connection
- Scan-back / Track Follow
- Volume Scan and vertex reconstruction

In this section, the vertex location procedure is described. Section 3.4.1 reports as example the results obtained for an event analysed in the Salerno laboratory.

3.2.1. CS scanning

As explained in section 2.1.1.b, the analysis of CS doublets [61] is used to validate tracks recorded in electronic devices. The task of locating the events in the OPERA detector is equally shared between European and Japanese laboratories. CS doublet scanning is performed, for events assigned to European laboratories, in Gran Sasso laboratories (LNGS).

In order to select the sample of tracks in the CS doublet to be matched with the TT predictions, a wide area scan is performed: for events with a muon in the final state, the area is 16 cm^2 around the predicted muon; for NC events, the area is optimised according to the shape of the hadron shower, and it can span the whole area of the CC doublet.

The standard procedure requires that a CS candidate have at least 3 micro-tracks out of 4 emulsion layers. Tracks found by automatic processing are manually checked to confirm their existence; on positive result, the brick is developed. The positions and slopes of candidate measured on the CS doublet are published to the central OPERA databases, OPITA/OPFRA, accessible by all laboratories.

Sometimes, no candidates are found on CS. This can be due to brick finding efficiency and also to scanning or reconstruction efficiencies. The neutrino interaction trigger and the brick location are based on the information from the electronic detectors. A probability map of bricks is built; depending on the event position there might be an ambiguity between adjacent bricks if the event is close to an edge. In this case, the first brick extracted is sent back to the detector and a CS of the second most probable brick is analysed. The brick finding efficiency as a function of the number of bricks removed per event is shown in Table 3.1 [56].

Brick finding efficiency			
Event type	**1 brick removed (%)**	**2 bricks removed (%)**	**3 bricks removed (%)**
DIS ν_μCC	78.3	86.2	92.2
DISν_μNC	66.7	77.6	79.6

Table 3.1: Brick finding efficiency as a function of the number of bricks removed per event.

3.2.2. CS-Brick connection

Bricks developed at LNGS are sent to several scanning laboratories to apply the second step of the vertex location procedure.

All tracks found on the CS doublet are searched in brick plates. The positions and slopes of CS candidates published in central databases (DB), are downloaded to local ones (each scanning laboratory runs its own scanning DB). Each CS candidate is searched for in the first five emulsion sheets of the brick with 500 μm position tolerance; for each plate, base-tracks are selected if satisfying the following requirements:

- position difference between CS candidate extrapolation and track in brick below 300 μm.
- slope agreement between CS candidate and track in brick better than 40 mrad.
- Sigma value (see 3.1.2.b) greater than 0.8.
- Number of grain greater than 20.

Figure 3.5 shows the display used to study the quality of base-tracks found in emulsion sheets. Tracks having at least three segments are selected as to input to the next steps. Of course, neutrino events may occur also in the last lead plates. Such cases demand more visual inspection by human operators to be handled, and kinematical analysis also requires extraction of the downstream brick.

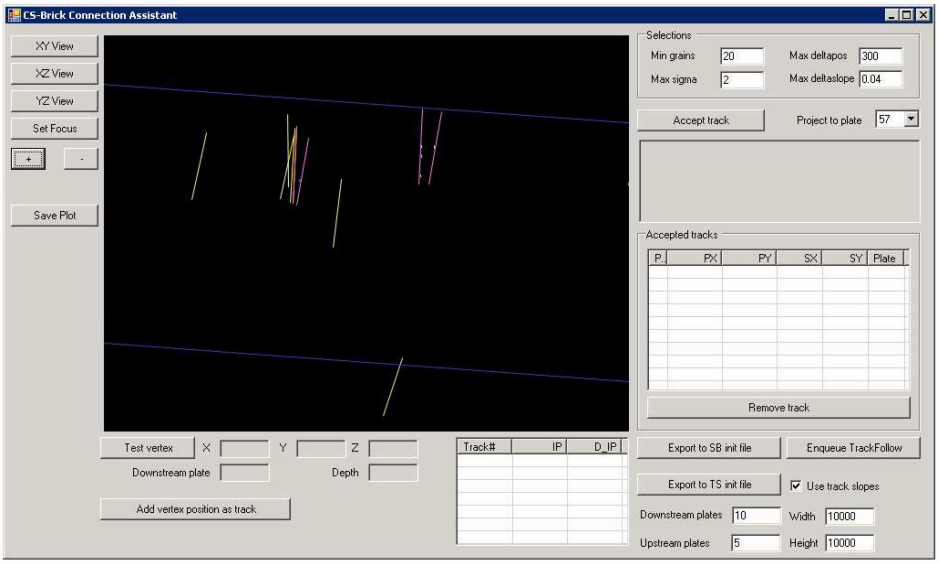

Figure 3.5: Display used to study the quality of base-tracks found in the emulsion sheets

3.2.3. Scan-Back – Track Follow

The hint for primary vertex point comes from the Scan-back procedure. CS candidates connected to bricks are followed down, plate-by-plate until their disappearance (see Figure 3.6 - Left). This condition is a clear signal that "something" happened in this point.

Starting from track position and slopes in the most downstream sheet, the track coordinates in the next upstream plates are predicted. Scanning of a single microscope view, centered at the expected point, is performed and the system, automatically, searches for micro-tracks compatible with the predicted track. Position and slope tolerances are applied (~80 μm for position and ~40 mrad for slopes) and also a cut on the number of grains (18-20, varying with the amount of fog). The newly found track is used to predict the position and slope at the next upstream plate, and the process is iterated until either of the following conditions occurs:

- No segments are found in almost five consecutive plates. This is the evidence that a possible interaction has been found. It is impossible, at this step, to obtain information about the nature of event: it might be a primary or a secondary interaction. Of course, inefficiency yields fake stopping points.
- The track exits the brick. It means that the neutrino interaction did not take place in the brick under examination, but in another one, namely the upstream one or an adjacent brick, respectively if the track exits from the most upstream plate ("passing-through") or through an edge ("edge-out"). Another brick is extracted, and its CS doublet is also scanned, searching for more tracks related to the event; the vertex location procedure is repeated as explained for the first brick. A fraction of the neutrino interactions occurs in the target frame, or in the target tracker fibers; such events cannot be used for neutrino oscillation search, because the vertex region cannot undergo topological analysis.

Another strategy, named Track Follow, has been recently developed in Salerno to locate the interaction point. It requires to scan a larger area, on all plates of the brick, in a volume skewed along the trajectory predicted from the CS-brick connection results (see Figure 3.6 - Right). After the reconstruction of all base-tracks contained in the scanned zone, volume tracks are reconstructed and tracks with positions and slopes that are compatible, within proper tolerances, with the ones of CS candidates are selected.

The size of the scanning zone is normally set to 3×3 mm^2, which is enough to account for the deviation of a 1 GeV track due to multiple scattering; after reconstruction, if the track is seen to exit the scanned area, the relevant plates are rescanned.

Although the scanning load may seem much bigger with respect to the Scan-back procedure, there are several advantages:

- the probability to find a fake stopping point is very low, because all plates are always scanned;
- the technique does not rely on visual inspection to assess the stopping point, hence non-expert supervision for microscope operation suffices;
- multi-prong vertices are often recognized at this stage, hence strengthening the definition of the stopping point;
- data taken at this step can be merged with those taken in the next steps, thus increasing the scanning efficiency in the vertex region by double data-taking;
- indeed, in Scan-back, most of the time is taken by plate setting, to the extent that, with the above mentioned area size, the effective time only increases by 10%.

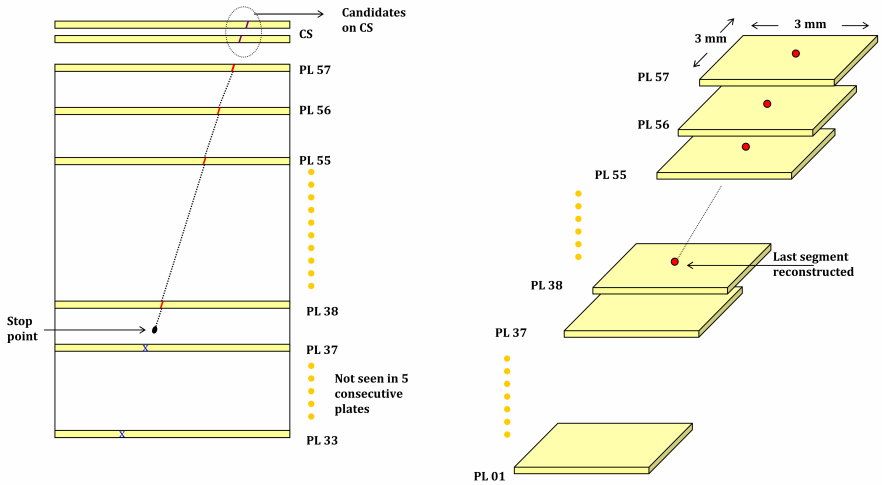

Figure 3.6: Left: Schematic representation of the Scan-back procedure. The track segments (in purple on CS doublet and in red on the brick) are seen just on the emulsion sheet (yellow) and not in the lead plate (white). When the track disappear for 5 consecutive plates the interaction point is located. Right: schematic representation of the Track follow procedure . An area of 3×3mm² around the candidate is scanned for 57 plates. The volume has the same slopes, in x and y, of the track being followed.

3.2.4. Volume Scan and Reconstruction

Once a track disappearance point is found, the volume scan procedure is applied in order to confirm the interaction and study the topology. A general scan of 1 cm^2 is performed in a predefined number of plates: typically the stopping plate (the last plate where the scan-back track was measured) plus 5 plates upstream and 10 downstream (see Figure 3.7). Track segments (base-tracks and micro-tracks) are measured within an slope acceptance of 0.6.

Emulsion films are aligned, as described in 3.1.2.c, with micrometric precision; then, tracking and vertexing are performed. Reconstruction of tracks and vertices is accomplished by an automatic software. The output is a file including all information, from micro-tracks to vertices found in the volume.

In order to perform alignment and reconstruct tracks some parameters (tolerances in slopes and positions, number of segments of a track, alignment quantities…) are used. A default configuration, that is the same for all analysed event, is applied. However, it is possible to tune these quantities if the a brick shows special features (high fog or no alignment cosmic rays) or the data quality is bad (faded images, high distortion).

Scan-back (or Track Follow) information is used to define the neutrino interaction vertex between all vertices in the volume: indeed, the software produces an unbiased reconstruction, and every geometrical crossing of tracks is considered a possible vertex; because of the high background due to refreshing remnants and cosmic ray tracks, information connected to the electronic detectors is mandatory to resolve the ambiguities.

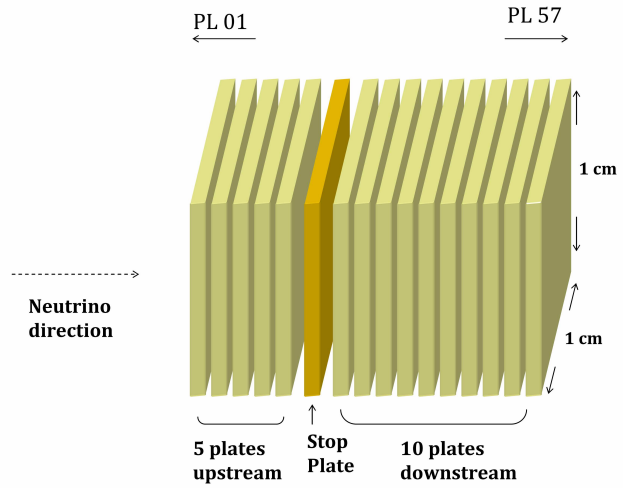

Figure 3.7: Schematic representation of a total scan volume. 1 cm^2 is scanned around the stopping point on 10 plates downstream and 5 upstream with respect to the lead plate in which the interaction supposed to be.

3.3. Primary Vertex Study

A relevant point of the study of neutrino interactions is the definition and study of the primary neutrino interaction vertex. The result of the location procedure needs to be confirmed and refined. A procedure developed on purpose, the *decay search* [72], is applied by all scanning laboratories.

3.3.1. The decay search procedure

The decay search procedure [72] allows to discriminate interesting topologies like charm or τ candidates from the majority of non-interesting ν_μCC/NC interactions. The *main vertex* definition is the first step: other tracks, in addition to the ones attached automatically at primary vertex, are searched. Disappearance of all tracks must be validated by a human operator; micro-tracks close to the vertex point are re-measured by the operator, choosing a single grain in a high magnification view: this improves the precision of measurements to the maximum quality that emulsion can offer, meanwhile removing any inefficiency from software algorithms.

Decays are searched *in-track* (small kinks) and by looking for *extra-tracks* (short decays with large kinks, secondary vertices). The former is applied to muons of primary vertex in charged current events and to all hadrons in neutral current events: the slopes of the first five segments are examined to unveil small kinks that might have been mistaken as the result of multiple scattering; single deviations are compared to the downstream scattering history of the track to check whether they are outliers in the scattering distributions (angular deviation > 5 RMS). *Extra-track* search looks for possible daughter tracks produced in the decay of short-lived particles: high momentum tracks (p > 1 GeV), disappearing close to the main vertex, but not attached to it (impact parameter > 10 μm), are examined as possible decay candidates; in this case, it is crucial to match the topological information from the emulsion to the electronic detector, to be sure that the track is really related to the event (it is worth to recall the background from refreshing remnants and cosmic ray tracks); low-momentum tracks may still show large scattering that explains the large impact parameter, and such cases are discarded.

If an interesting topology is found, the computation of kinematical quantities starts. The event is classified like a charm or τ candidate if it passes all kinematical cuts imposed by the OPERA Proposal; further studies are of course underway to improve the signal/background ratio.

3.3.2. Scan-Forth and hadron interactions search

Event analysis is completed with the Scan-forth (SF) procedure and hadron re-interaction search. The practical working principle of SF is the same as Scan-back; however, tracks are followed away from the vertex point to gather information about their momenta (from multiple scattering distributions) and to check for possible secondary interactions (see Figure 3.8). Of course, Scan-back tracks already have this

information, and SF is not needed for them; it is interesting for high-momentum hadrons attached to primary vertex, or for the muon in the few cases in which it is not among the Scan-back tracks.

The SF process stops if track exits the brick (sidewise or reaching the CS doublet), if a disappearance point is found. In the latter case, further investigation is needed to check the nature of the interaction.

A high-momentum hadron stops in the volume only if it interacts with the target (mostly lead). Another volume is scanned around the stopping point of the SF track, with 1 cm^2 area 11 consecutive films (5 upstream and 6 downstream with respect to the supposed interaction point – see Figure 3.9). Automatic reconstruction is then used to detect the topology of the secondary interaction.

SF/SB data are used to compute track momentum by using multiple Coulomb scattering as described in the next chapter. Hadron interaction search is important to estimate the background to τ decay topologies. The data collected can be used to validate or replace information from the Monte Carlo simulation. This subject will be analysed in chapter 5.

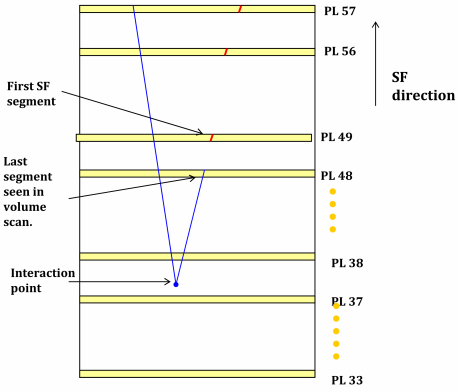

Figure 3.8: Schematic representation of the Scan-Forth procedure. Blue line depicts the track found during the Scan-Back or volume-scan procedure; red segments correspond to tracks found during Scan-Forth from plate #49 to plate #57.

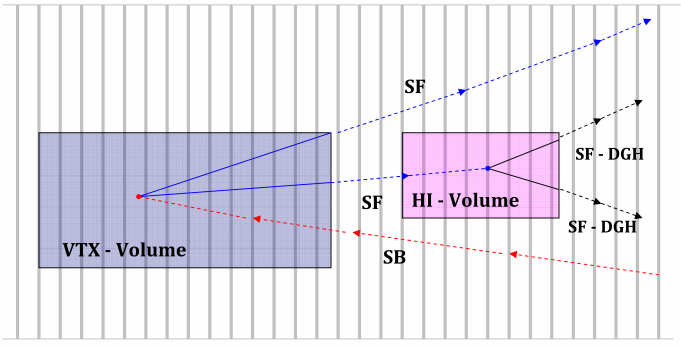

Figure 3.9: Schematic representation of scanning tasks in a brick. The dotted red line represent the SB track leading to the interaction point. The blue box represents the volume scanned around the vertex to detect more tracks, shown as solid blue lines; they are followed down through the brick with the SF procedure (dotted blue line); one stops in the brick and another volume scan to check for hadron interaction is performed (purple box); the daughter tracks of the secondary interaction are also brought by SF to the end of the brick (dotted black lines).

3.4. Sample results from the Salerno laboratory

Here the procedure explained in the previous section is shown in its practical application to an event located in the laboratory of the Salerno University. An account is given of the events located in Salerno, with the relevant quantities measured. Results from hadron interaction search are reported in chapter 5 where they are also compared to Monte Carlo simulation.

3.4.1. An example: Event #227200791

Event #227200791 was one of the first assigned to the Salerno laboratory in 2008. It is a charged current event, as shown in the display of the electronic detector in Figure 3.10. The momentum of the fitted muon (red line) was estimated to be about 18 GeV/c by the spectrometer. The brick in which the interaction occurred has number 1133734. On the CS doublets, 3 tracks were found but none of them was flagged as the muon. In Figure 3.11 the position of the tracks in the X-Y plane of the emulsion plate is reported. The magnitude and the direction of the arrows depend on the slopes of the track for which the arrow stands.

The CS-Brick connection procedure was successfully accomplished and just one track was selected to be followed upstream in the brick. The track stopped between plate 33 and 32 and a volume scan was performed as the location procedure requires. A track compatible with the muon was found in the reconstructed volume, but it stopped 2 plates upstream of the SB track. The decay search procedure was applied and the stopping points of both tracks were confirmed by human check. A track connecting the muon-candidate and the SB track was found, and, in the emulsion sheet, a “black” (highly ionising) track from the supposed secondary interaction point was seen. The SF of the muon-candidate track and also of the black track was performed: the former was followed downstream to plate 57 and its presence on the CS doublets was confirmed upon a specific request by the LNGS Scanning Station. The black track stopped after three plates in the volume and it was identified (by dE/dx compatibility) as a proton produced in the secondary interaction. Figure 3.12 displays several views of the event. SB and SF paths are also included in the plot.

The two tracks attached to the primary vertex had an impact parameter of 0.7 μm. The impact parameter of the two tracks at the secondary vertex was about 9.5 μm. The momenta of the SB track and of the muon-candidate were computed by the official algorithm. The best estimation of the momentum of the muon candidate was 10 GeV/c, to be compared to the measurement by the spectrometer, i.e. 18 GeV/c. The seemingly big difference (8 GeV/c) between the two estimates is fully justified by the resolution (actually 1/p is measured both by scattering and track bending). The momentum of the SB path was estimated to be 700 MeV/c.

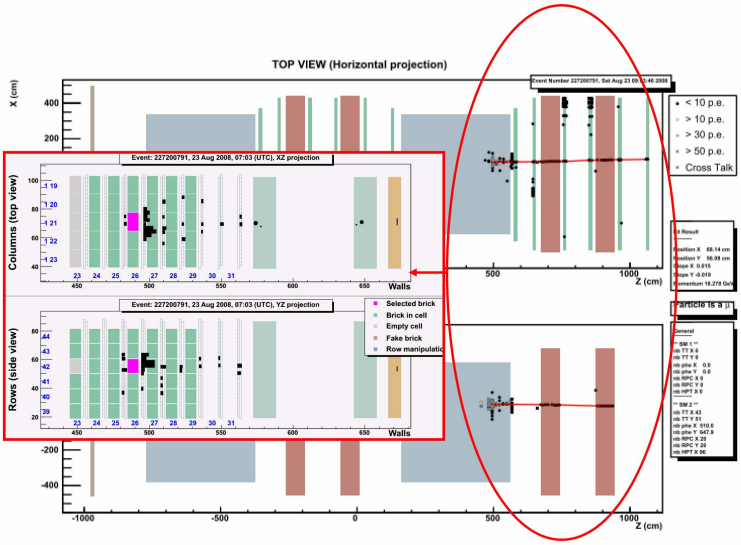

Figure 3.10: The electronic display for event # 227200791. The area encompassed by the red line is zoomed in the left part of the image.

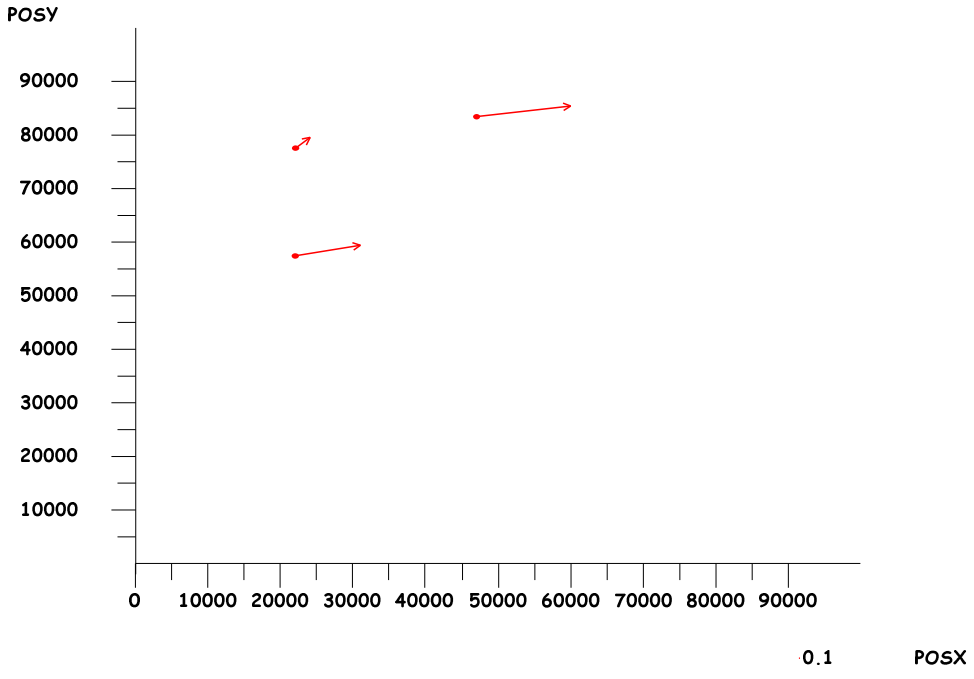

Figure 3.11: Position of the tracks found in the CS doublet for the event 227200791. The magnitude and the direction of the arrows depend on the slopes of the track.

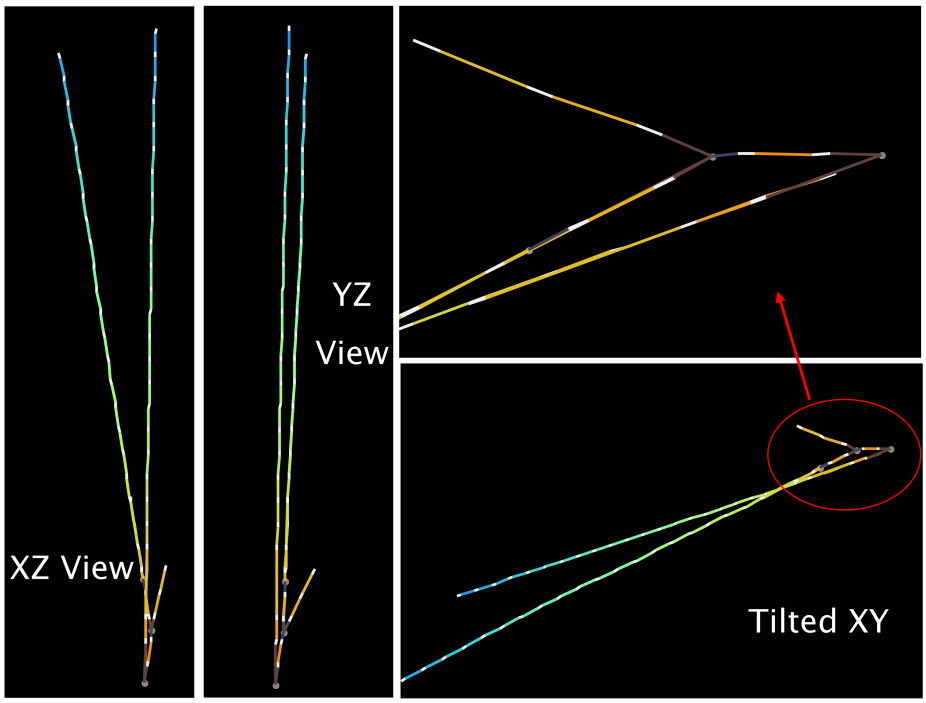

Figure 3.12: Display of the reconstructed event 227200791. Four views are shown: the XZ view, the YZ view and a tilted XY one, with a zoom on the vertex region and the secondary interaction in the top-right panel.

3.4.2. Location summary and performance

The status of the scanning activity at the University of Salerno is summarised in Figure 3.13, showing the number of events received, "connected" (recall CS-Brick connection), located and decay-searched for the 2008, 2009 and 2010 runs, as a function of time (from July 2008 until February 2011).

In Table 3.2, the status of event location in Salerno is reported for each run: not only the number of received and located events is shown, but also the number of events in "dead material" (i.e., where decay search cannot be applied, such as target tracker fibres or brick supports) or for which another brick was requested.

These data are used to compute the efficiencies reported in Table 3.3; since analysis is completed only for the sample from 2008 run, the efficiency estimates for 2009 and 2010 are expected to fluctuate around the present values in the next future.

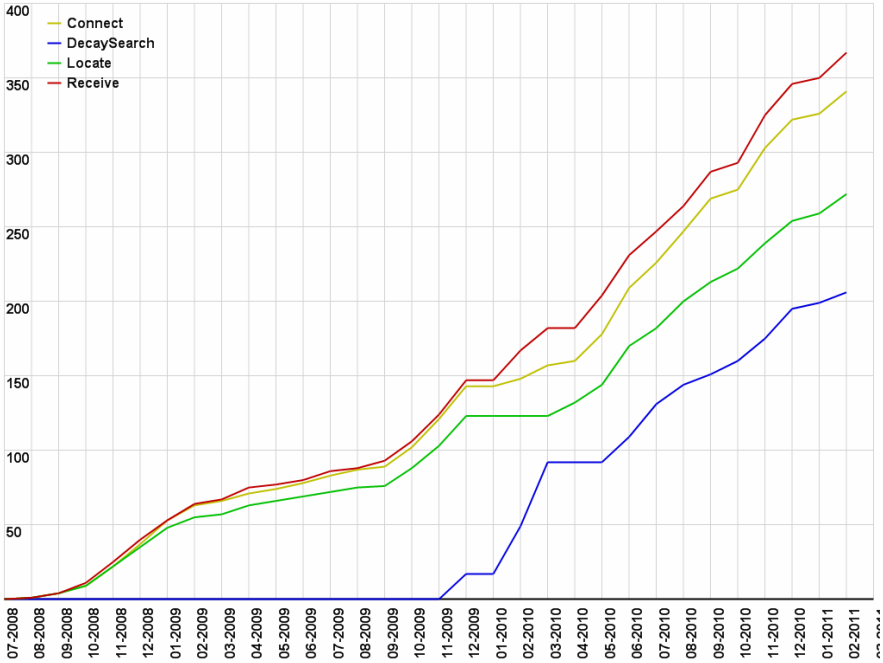

Figure 3.13: Scanning status of the Salerno laboratory

	2008		2009		2010	
	0μ	**1μ**	**0μ**	**1μ**	**0μ**	**1μ**
Received	20	103	35	181	8	50
Connected	15	92	29	172	7	44
Interactions located in ECC	9	69	18	133	6	36
Interactions in the upstream brick	0	0	0	15	0	1
Interactions in dead material	4	8	2	7	0	1
Decay search performed	9	69	16	107	2	13

Table 3.2: Event location summary for the Salerno laboratory - run 2008, 2009 and 2010

	2008		2009		2010	
	0μ	1μ	0μ	1μ	0μ	1μ
Connection fraction	0.75	0.89	0.83	0.95	0.87	0.88
Location fraction	0.65	0.73	0.57	0.77	0.75	0.74
Decay Search fraction	1	1	0.46	0.60	0.25	0.26

Table 3.3: Overall efficiencies computed by using the Salerno statistics. Runs 2008-2009 and 2010.

3.4.3. General statistics

This section illustrates the distributions of the relevant quantities measured for the events that underwent decay-search. The multiplicity of tracks at the primary vertex, the primary vertex positions and the impact parameter of primary prongs were computed using the 2008 and 2009 data. Because of the small statistics, data from the 2010 run were not used.

In Figure 3.14 and Figure 3.15 the positions of the vertices found, respectively, in the 2008 and 2009 run is displayed. In both cases, in the left plot the vertex positions in the X-Y plane is reported whereas, in the right side, the longitudinal position of the vertices (as number of plate) is shown.

In Figure 3.16 the multiplicity distributions are shown: the red histogram displays the multiplicity of CC events, the blue one stands for NC events and the black is the sum of the two samples. The shape of the 2009 distribution is slightly different from the one of 2008: in the former, a larger amount of single-prong events was found. Although the sizes of the two samples are comparable, this result is still to be considered preliminary: the primary interaction of quasi-elastic (QE) events, with a hard muon providing a tight tagging of the brick, are indeed easier to locate than DIS events with big showers that blur brick finding; hence, a trustworthy picture of efficiencies is possible only when location is complete for all events in a run, whereas the first events in the location pipeline are biased.

In Figure 3.17 the impact parameter of the tracks attached to the primary vertex is shown. The red distribution denotes muon tracks, whereas the black one is obtained using all tracks at primary vertex (excluding electron-positron pairs). The muon distribution is contained within 10 micron, which is the maximum impact parameter value allowed for muons by the decay search procedure. The distribution of all other tracks has a tail for IP values exceeding the aforementioned boundary: such tracks correspond to low momentum particles or nuclear fragments produced in the neutrino interaction.

In Figure 3.18 the track angle distributions are shown. Also in this case a difference between the muon sample and other tracks is performed. The number of tracks having a

slope > 0.5 is very low, and no muons are included in this category. This plot justifies why kinematical analysis is restricted to tracks with slope below 0.5.

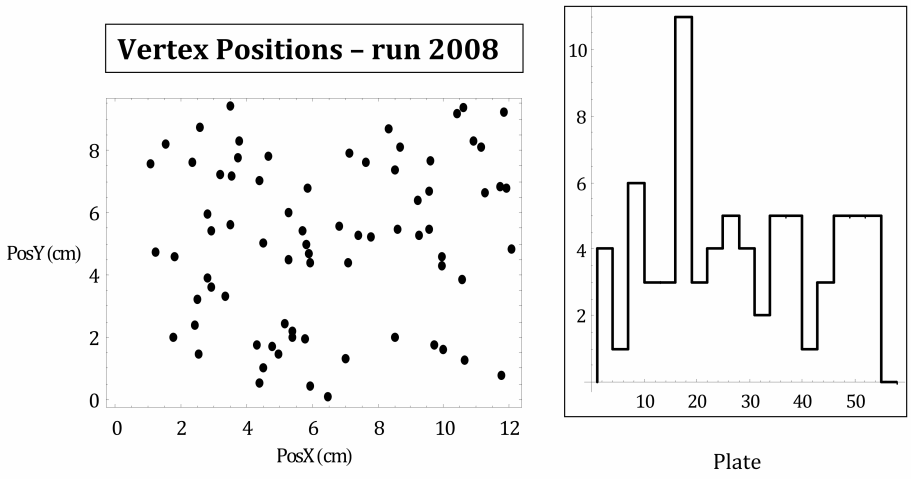

Figure 3.14: Left: The vertex position in the plane X-Y; Right: The longitudinal vertex positions (as number of plate) - Run 2008

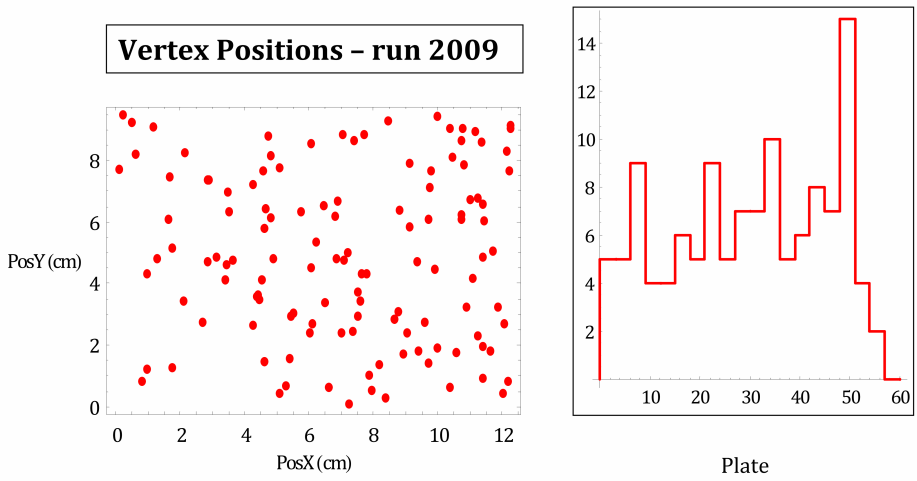

Figure 3.15: Left: The vertex position in the plane X-Y; Right: The longitudinal vertex positions (as number of plate) - Run 2009

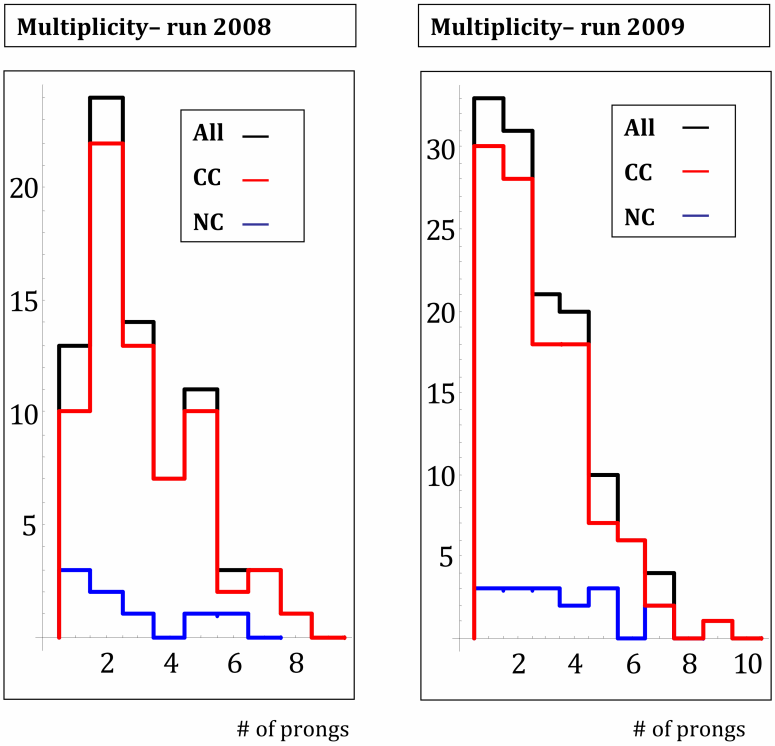

Figure 3.16: Multiplicity distributions for the 2008 run (left) and the 2009 run (right)

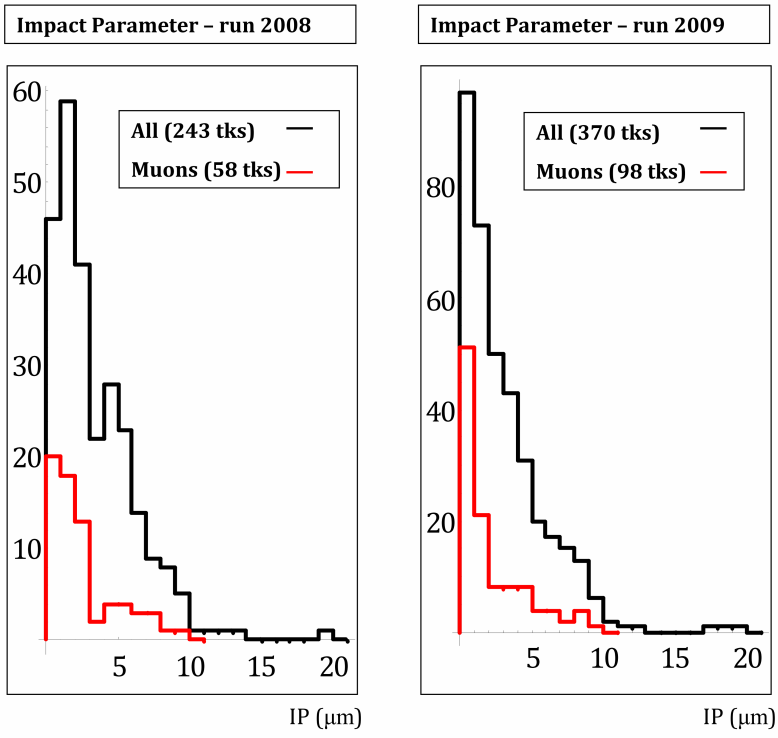

Figure 3.17: The impact parameter distributions for the 2008 run (left) and 2009 run (right)

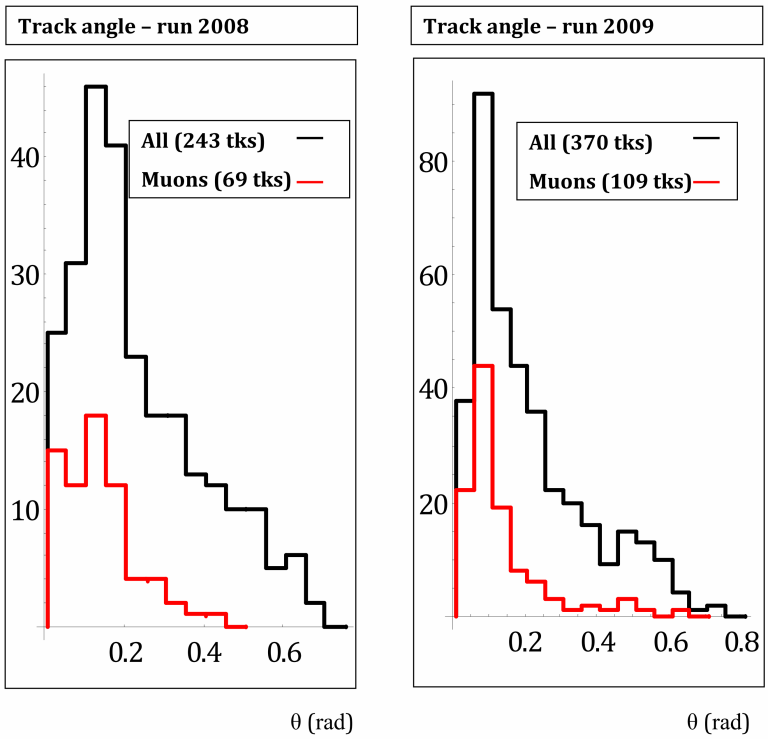

Figure 3.18: Track angle distributions for the 2008 run (left) and the 2009 run (right)

3.5. OPERA status and performance

The status of the OPERA analysis can be summarised by the plot shown in Figure 3.19 [73]: the black line stands for the number of interactions triggered in the detector since July 1st, 2008 until February 2011. All steps of the vertex location and decay search procedure are accounted for. The flat regions in the black line correspond to no-beam periods. Scanning in laboratories runs around the whole year, and it can be seen that the average slope of event location and decay search are increasing with time, thanks to improved know-how and scanning strategy optimisation.

The number of events located by the OPERA experiment is reported in Table 3.4 [73]. The efficiency reported in Table 3.5 [74] are computed by considering just the data from the 2008 run, for which the analysis is complete.

In Table 3.6 the number of peculiar topologies found in the 2008, 2009 and 2010 OPERA run is reported. The sample includes the charm events that, as explained in section 2.2.1, constitute one of the main source of background, and the ν_e - induced events originated by the ν_e ($\overline{\nu}_e$) contamination of the ν_μ beam (~1%) [56].

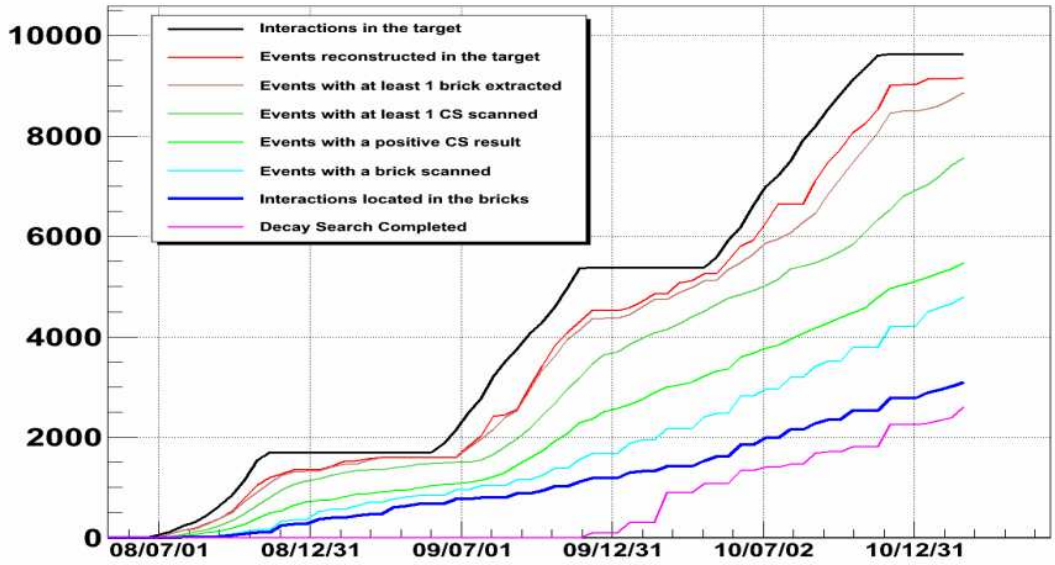

Figure 3.19: Scanning status of the OPERA experiment as of February 2011.

	2008		2009		2010	
	0μ	**1μ**	**0μ**	**1μ**	**0μ**	**1μ**
Event Predicted by electronic detector	406	1292	1097	2460	1165	2747
Found in CS	275	1053	694	2009	391	1090
Interactions located in ECC	166	825	318	1304	104	384
Located in dead material	26	92	16	102	-	-
Interactions in the upstream brick	6	37	27	142	-	-
Decay search performed	154	772	260	1098	66	232

Table 3.4: Event location summary for the OPERA experiment - the 2008, 2009 and 2010 run

Overall efficiency (run 2008)	1μ	0μ	All
Triggers	1698	406	1292
Interactions in the bricks	0.925		
Rejected bad quality CS films	0.06		
Brick identification by electronic detectors	0.78	0.65	0.815
Location fraction	0.88	0.72	0.93

Table 3.5: Overall efficiency obtained using the 2008 statistics.

Events Located	Decay Search (CC)	Charm Candidates	ν_e Candidates
3101	2121	44	13

Table 3.6: Peculiar topologies found in the 2008, 2009 and 2010 OPERA runs.

Chapter 4

Likelihood approach to momentum measurement

In the OPERA experiment, event analysis requires good knowledge of event kinematics. At several analysis steps not only the track positions but also the momentum information should be available in order to select and classify an interesting event.

The momentum of a charged particle traversing the emulsion sheets can be computed from its multiple Coulomb scattering (MCS) in ECC bricks. Two methods are described in the OPERA proposal [56]: one uses the track positions (coordinate method), the other one the track angles (angular method) measured in each emulsion film.

To compute the particle momenta, the official software uses the angular technique based on a nonlinear fit method. [75], [76], [77]. In this chapter an alternative approach is described; angular measurements are used but the momentum estimate is performed by software based on the likelihood concept.

4.1. Momentum measurement by MCS

The MCS of a particle in the emulsion sheets can be evaluated by using the angular measurements of the track: the difference of angles measured in two emulsion films gives a simple estimate of the scattering angle. The particles cross cells made of 1mm lead + ~300 μm emulsion/plastic. The distribution of the scattering angle in a plane is approximately Gaussian with a squared-RMS given by the Highland formula [78]:

$$\sigma^2 = \left[\frac{0.0136\ (GeV/c)}{p\beta} \sqrt{X} \right]^2 \qquad 4.1$$

where: p is the particle momentum (to be estimated), β is the particle velocity and X is the traversed material thickness measured in units of radiation length.

This quantity yields the "true" squared-RMS (σ_{true}^2) of scattering angle distribution, not affected by any errors; the measured squared-RMS, σ_{meas}^2 is related to σ_{true}^2 by the following expression:

$$\sigma_{meas}^2 = \sigma_{true}^2 + \delta\theta^2 \qquad 4.2$$

where $\delta\theta$ is the angular resolution on the difference of two measured base-track angles. The value for this measurement error quoted in the OPERA Proposal is about 2 mrad [56].

Angular differences are computed using pairs of reconstructed base tracks separated by a fixed number of brick cells (N_{cell}) which defines the effective lead thickness sampling (scattering in emulsion and plastic can be neglected). Several techniques aim to increase the signal/noise ratio (N_{cell} dependent method with/without offset) [75], [76], [77].

4.1.1. Determination of the momentum with the official software

To understand the method used for the estimation of the momentum with the official software it is useful to re-write the expression 4.1 as a function of N_{cell}:

$$\sigma_{meas}{}^2 = \left[\frac{0.0136}{p\beta} GeV / c \sqrt{\frac{N_{cell}}{5.6}} \right]^2 + \delta\theta^2 \qquad 4.3$$

The measured squared-RMS depends on the particle momentum p and the base-track resolution $\delta\theta$. The determination of the term $\delta\theta$ is crucial for the momentum measurements accuracy.

The first step of the momentum estimation procedure is to fit the function $\sigma_{meas}(N_{cell})$ with a set of passing-through tracks (i.e crossing all the brick) having the same momentum. It allows to determine $\delta\theta$, set as a parameter in the fit. This first step can be performed only with the same momentum tracks. This is somehow an ideal case that can be exploited either when an ECC is exposed to a charged particle beam of high intensity or in a Monte-Carlo simulation.

The second step is to fit $\sigma_{meas}(N_{cell})$, track by track with know $\delta\theta$ as a fixed parameter and p as a free parameter, to obtain the momentum measurement of the given tracks.

In general assuming a Gaussian distribution for σ, the shape of the momentum distribution is given by a function like:

$$f(p) = \frac{p_0}{p^2} \times \exp\left(-\frac{(1/p) - (1/p_1)^2}{1/p_2^2} \right) \qquad 4.4$$

where p0, p1 and p2 are free parameters.

4.2. Review of the likelihood method

The Maximum Likelihood Estimation (MLE) is a statistical method used for fitting a statistical model to data and providing estimates for the model parameters.

MLE requires that a mathematical expression, known as *Likelihood Function* of the sample data, be defined. The likelihood of a data set is the probability of obtaining that particular set of data given the chosen probability distribution model. The desired probability distribution is the one that makes the observed data "most likely", which means that one must seek the value of the parameter vector that maximizes the likelihood function.

Let us consider a set of n independent random observables $y = \{y_i\}$ from a population with a probability distribution function $f_i(y_i \mid q)$ depending on the q parameter, to be estimated. If all data are independent, the likelihood function is defined as the joint probability function of $y_1, y_2, y_3 \ldots y_n$:

$$L(\bar{y} \mid q) = \prod_{i=1}^{n} f_i(y_i \mid q) \qquad 4.5$$

If variables are correlated (not independent), the joint probability function of n Gaussian random variables is given by

$$L(\bar{y} \mid q) = \frac{1}{(2\pi)^n \sqrt{\det \Sigma}} \exp\left[-\frac{1}{2} (\bar{y} - \bar{\mu}) \bullet \Sigma^{-1} (\bar{y} - \bar{\mu}) \right] \qquad 4.6$$

where $\bar{y}$ is the vector of observations and $\bar{\mu}$ is the vector of means. Σ is the covariance matrix. Both the means and the covariance matrix may depend on q.

The method of MLE estimates the q parameter by finding a value that maximizes the likelihood function:

$$\hat{q} = \arg\max_q L(\bar{y} \mid q) \qquad 4.7$$

If the parameter q has no physical constraints (it means that it can assume all possible values), as the sample size increases, the distribution of the MLE tends to Gaussian distribution with mean $\hat{q}$.

The likelihood approach can also provide a confidence region that allows to restrict the expected values. The likely region is defined by using the following inequality (likelihood ratio):

$$2\ln\left(\frac{L(\hat{q})}{L(q)}\right) \leq \chi^2_{(1,1-\alpha)} \qquad 4.8$$

where $L(q)$ is the likelihood function for the unknown parameter vector q, $L(\hat{q})$ is the likelihood function calculated at the estimated parameter $\hat{q}$ and $\chi^2_{(1,1-\alpha)}$ is the (1-α)% point of the chi-square distribution with 1 degree of freedom. It means that all values of q satisfying the relation 4.8 are included in the (1-α)% confidence interval for the parameter of interest.

In the case of really Gaussian variables an exact coverage is assured, otherwise it is only approximate. The deviation of the coverage from the expected value is also a measurement of the quality of the model.

4.3. The MCS in the likelihood approach

In the likelihood approach to momentum estimation, the set of variables used is a sample of angular scattering between two emulsion films and the parameter to be inferred is the momentum of particle.

Since the measurement error grows with increasing slope in the longitudinal projection, just the transverse projection having a constant error is used. The slope differences $[\Delta\theta_{\perp 1},\ldots.\Delta\theta_{\perp n}]$, are not averages but differences between two measurements.

If measurements are independent, the likelihood function is written using the general form

$$L\left(\Delta\theta_{\perp 1},....\Delta\theta_{\perp n} \mid p\right) = \prod_{i=1}^{n} \frac{1}{\sqrt{2\pi}\vartheta_i(p)} e^{\frac{\Delta\theta_{\perp i}^2}{2\vartheta_i(p)}} \qquad 4.9$$

where: $\vartheta_i(p) = \frac{0.0136}{p\beta}\sqrt{\frac{l_i}{X_0}}$ and l_i is the flight length across which the i-th difference is computed. The type of material traversed (lead, plastic or emulsion) can also be taken into account. However, each measurements appears at least in two differences, correlations do exist, and it is mandatory to resort to the more general formula, which in this case reads:

$$L\left(\Delta\theta_{\perp 1},....\Delta\theta_{\perp n} \mid p\right) = \prod_{i=1}^{n} \frac{1}{\sqrt{(2\pi)^n \det\Sigma(p)}} e^{-\frac{1}{2}\sum_{i,j=1}^{n}\Delta\theta_{\perp i}\Delta\theta_{\perp j}\sigma_{ij}(p)} \qquad 4.10$$

Precise evaluation of the correlations between any two measurements is reported in the next section.

4.3.1. The covariance matrix

To study in detail the origin of the measurement correlations it is useful to "see" how this matrix is built. The matrix rank is equal to the number of slope differences computed:

$$\Delta\theta_{\perp,k} = \theta_{\perp,k+1} - \theta_{\perp,k} \qquad 4.11$$

The elements of the covariance matrix are connected to measurements correlations. The diagonal elements can be written as:

$$\sigma_{kk}{}^2(p) = \langle \Delta\theta_k, \Delta\theta_k \rangle = \sigma^2_{kk,true} + 2\delta^2_{\perp} \qquad 4.12$$

where $\sigma^2_{k,true} = \left(\frac{0.0136}{p\beta} \sqrt{\frac{l_k}{X_0}} \right)^2$.

The expression 4.12 has been obtained by taking into account that each measurement is affected by an error, with a vanishing mean and a standard deviation denoted as $\delta_{\perp}$. To show this, let us set for example k = 1 and compute the $\sigma^2_{1,1}$ term:

k = 1

$$\sigma^2_{11} = \langle \Delta\theta_{1,meas}, \Delta\theta_{1.meas} \rangle$$

$$\Delta\theta_{1,meas} = \theta_{2,meas} - \theta_{1,meas} = \theta_{2,meas} + \theta_{2,true} - \theta_{2,true} - \theta_{1,meas} + \theta_{1,true} - \theta_{1,true}$$

$$\langle \Delta\theta_{1,meas}, \Delta\theta_{1,meas} \rangle =$$

$$= \langle \theta_{2,meas} + \theta_{2,true} - \theta_{2,true} - \theta_{1,meas} + \theta_{1,true} - \theta_{1,true}, \theta_{2,meas} + \theta_{2,true} - \theta_{2,true} - \theta_{1,meas} + \theta_{1,true} - \theta_{1,true} \rangle =$$

$$= \langle -\theta_{1,meas} + \theta_{1,true}, -\theta_{1,meas} + \theta_{1,true} \rangle + \langle \theta_{2,true} - \theta_{1,true}, \theta_{2,true} - \theta_{1,true} \rangle + \langle \theta_{2,meas} - \theta_{2,true}, \theta_{2,meas} - \theta_{2,true}$$

$$= \langle \theta_{1,meas} - \theta_{1,true}, \theta_{1,meas} - \theta_{1,true} \rangle + \langle \theta_{1,true} - \theta_{2,true}, \theta_{1,true} - \theta_{2,true} \rangle + \langle \theta_{2,meas} - \theta_{2,true}, \theta_{2,meas} - \theta_{2,true} \rangle =$$

$$= \delta^2 + \sigma^2_{12} + \delta^2 =$$

$$= \sigma^2_{12,true} + 2\delta^2$$

since

$$\langle \theta_{1,meas} - \theta_{1,true}, \theta_{2,meas} - \theta_{2,true} \rangle = 0$$

$$\langle \theta_{1,meas} - \theta_{1,true}, \theta_{1,true} - \theta_{2,true} \rangle = 0$$

$$\langle \theta_{2,meas} - \theta_{2,true}, \theta_{1,true} - \theta_{2,true} \rangle = 0$$

Elements with |k-j| = 1 all have the same value:

$$\sigma_{kj}{}^2(p) = \left\langle \Delta\theta_k, \Delta\theta_j \right\rangle = -\delta^2 \qquad 4.13$$

computed, for example for k = 1 and j = 2, in the following way:

k = 1; j = 2

$$\sigma_{12}^2 = \left\langle \Delta\theta_{1,meas}, \Delta\theta_{2.meas} \right\rangle$$

$$\Delta\theta_{1,meas} = \theta_{2,meas} - \theta_{1,meas} = \theta_{2,meas} + \theta_{2,true} - \theta_{2,true} - \theta_{1,meas} + \theta_{1,true} - \theta_{1,true}$$

$$\Delta\theta_{2,meas} = \theta_{3,meas} - \theta_{2,meas} = \theta_{3,meas} + \theta_{3,true} - \theta_{3,true} - \theta_{2,meas} + \theta_{2,true} - \theta_{2,true}$$

$$\left\langle \Delta\theta_{1,meas}, \Delta\theta_{2,meas} \right\rangle =$$

$$= \left\langle \theta_{2,meas} + \theta_{2,true} - \theta_{2,true} - \theta_{1,meas} + \theta_{1,true} - \theta_{1,true}, \theta_{3,meas} + \theta_{3,true} - \theta_{3,true} - \theta_{2,meas} + \theta_{2,true} - \theta_{2,true} \right.$$

$$= \left\langle \theta_{2,meas} - \theta_{2,true}, \theta_{2,true} - \theta_{2,meas} \right\rangle =$$

$$= -\left\langle \theta_{2,meas} - \theta_{2,true}, \theta_{2,meas} - \theta_{2,true} \right\rangle =$$

$$= -\delta^2$$

All terms with |i-j| > 1 vanish because they have no measurement in common.

4.3.2. Implementation details

The algorithm uses the formula 4.1 with a correction for Monte Carlo data (see section 4.4.1.b). The input parameters of the implemented software are:

- N_{cell} *value:* is the step between two slope measurements. The best choice is the one that gives a set of difference with the maximum number of linear independently measurements. This value has been set to 1, so as all consecutive measurements are taken.
- *Minimum and maximum momentum:* the likelihood function is computed spanning this region with a momentum step of 50 MeV/c, which is known to be well below the estimation errors.
- *Required confidence level:* it is expressed as a percentage and represents how often the true value lies within the confidence interval. Usually 90% confidence level is required.
- *Geometry Configuration:* information about the geometry and material of the brick (number of plates, missing sheets)
- *Set of measurements:* Set of slopes and positions measured in each plate.

4.4. Summary of test results

The implemented software was tested on two samples of Monte Carlo (MC) data and on two samples of real data. The first set of simulated data was obtained using a *Mathematica* script as a "toy generator". The particle scattering in lead plates has been simulated; emulsion plates were neither included in the simulation nor in the configuration.

The other MC sample was generated by ORFEO [75], a simulation tool based on GEANT, developed for OPERA ECC. Particle interactions with the medium are simulated and the main effects of the scanning efficiency and resolutions are included. This MC sample does not include any background simulation of cosmic rays or fog in emulsion. The results on simulated data are reported in section 4.4.1.

In addition, two samples of real data have been studied. The first set comes from lead-emulsion bricks exposed to 2, 4 and 6 Gev pion beams during the 2003, 2004 and 2007 test beam campaigns at CERN. The bricks with 2 and 4 Gev pions were scanned in Naples and the 6 GeV sample in Bologna.

A set of *soft-muons* reconstructed in OPERA ECC scanned in Salerno, during the runs of year 2008 and 2009, makes up for the second sample of real data. The results on real data are reported in section 4.4.2.

4.4.1. Simulated data

4.4.1.a. Results on simulated data from Mathematica

The *Mathematica* software was used to simulate the scattering in lead plates of particles with a fixed momentum in the Gaussian scattering approximation, as shown by expression 4.1. This formula has been used both for the scattering angle generation and as a model for momentum estimation in the likelihood-based software; hence, in this case the model is perfectly identified.

The multiple Coulomb scattering of 1000 tracks for each momentum value (2, 4, 6, 8 and 10 GeV) in 1 mm lead plates was simulated. The measurement error, denoted as $\delta\theta$, was set to 2 mrad and the required coverage was 90%. Table 4.1 reports the median, the quantity $P_{min}/P_{max\ (\alpha\%)}$ that represents the lower/upper quantile of the population of estimated momenta and the coverage obtained. The results are also summarised in Figure 4.1. The statistical coverage is compatible (within statistical errors) with the confidence level required.

As explained in section 4.2, the maximum likelihood estimator is normally distributed if there are no constraints on the parameter. In our case, the momentum cannot assume a negative value; the distribution of estimated momenta is not Gaussian, and is also largely skewed because at high momentum values, measurement errors mask the effect of scattering, thus reducing the resolution (see Figure 4.2): the median is used because it it is less sensitive than the mean to asymmetries.

P_{True} (GeV/c)	δθ (mrad)	Median (GeV/c)	$P_{min,68\%}$ (GeV/c)	$P_{max,68\%}$ (GeV/c)	$P_{min,90\%}$ (GeV/c)	$P_{max,90\%}$ (GeV/c)	Coverage
2	2	2.07	1.65	2.65	1.75	2.35	90.6 ± 3.2
4	2	4.10	3.10	6.35	3.40	5.10	91.5 ± 3.1
6	2	6.30	4.15	12.5	4.80	8.70	87.5 ± 3.0
8	2	8.52	5.45	23.1	6.45	12.9	87.2 ± 3.0
10	2	11.0	6.60	50.7	7.80	17.7	87.1 ± 2.9

Table 4.1: The results obtained using a set of simulated tracks with P_{True} momentum. The median value, the lower/upper quantile of the population (at 68% and 90%) of estimated momenta and the coverage obtained are reported.

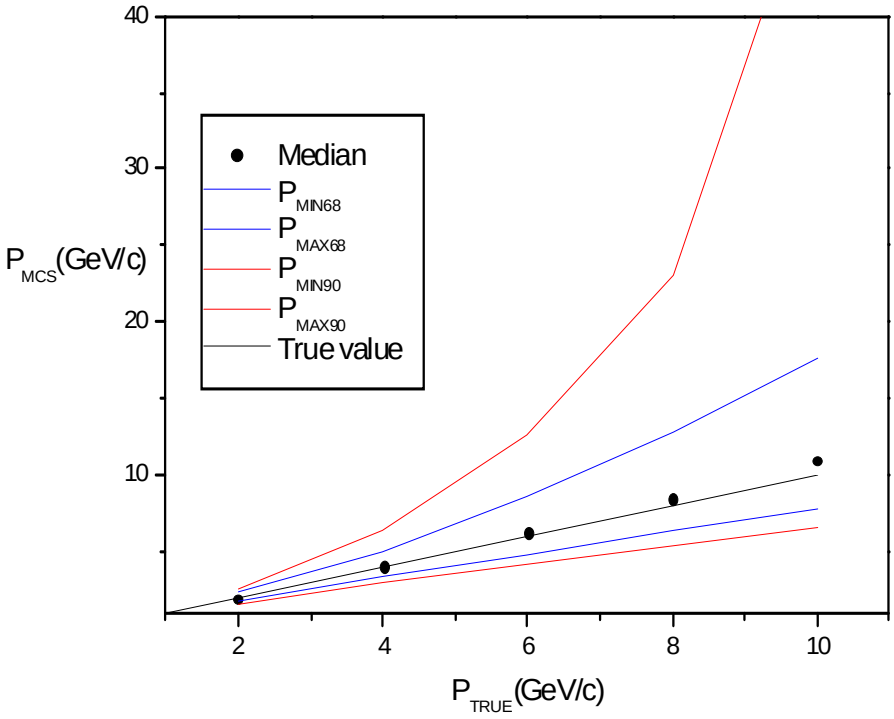

Figure 4.1: The results obtained using a set of simulated tracks with P_{True} momentum are summarized in this plot. The black points mark the median value, the black line is the bisector (where the median values should be). Blue/red lines bound the 90%/68% quantile of the population of estimated momenta.

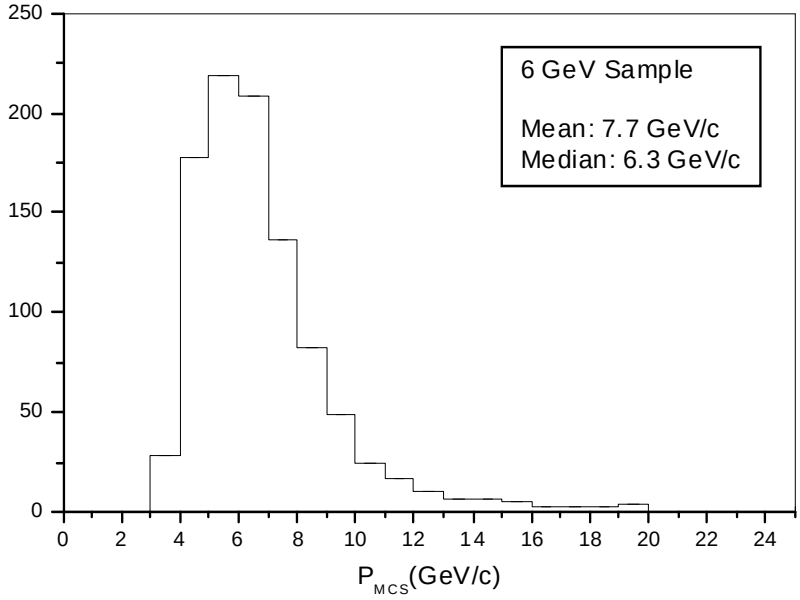

Figure 4.2: The distribution of estimated momenta obtained using a sample of 6 GeV/c simulated data. The distribution shows a long tails for high momentum tracks, which have scattering effect smaller than the measurement error.

4.4.1.b. Results on simulated data from ORFEO

Another analysis was performed on a second set of simulated data provided by the OPERA collaboration [79]. As explained, the simulation of scattering by particles with momentum of 1, 4 and 6 GeV/c is done using a tool (ORFEO) based on GEANT. GEANT [80] uses the following generation formula:

$$\sigma^2 = \left[\frac{0.0141}{p\beta} GeV / c\sqrt{X} \right]^2 \qquad 4.14$$

that is only slightly different from expression 4.1. In order to compute the likelihood function, just for this data sample, formula 4.14 has been applied. The value of the measurement error was set to 1.67 mrad [81] during the simulation and then the same value was plugged into the likelihood-based software.

Tracks with bad reconstruction were excluded from the momentum estimation sample: at least 50 measured plates out the 57 plates in the ECC brick were required; momentum estimation is known to be spoiled by reducing the amount of available measurements. 2880 tracks were selected from the 1 GeV sample, 3709 from the 4 GeV one and 3554 from the 6 GeV sample.

Results are reported in Table 4.2 and also shown in Figure 4.3. Unlike the previous case, the coverage is not compatible with the expected value of 90%, most probably because the formula used in the generator does not match exactly the one used in the momentum fitting algorithm.

P_{True} (GeV/c)	δθ (mrad)	Median (GeV/c)	$P_{min,90\%}$ (GeV/c)	$P_{max,90\%}$ (GeV/c)	$P_{min,68\%}$ (GeV/c)	$P_{max,68\%}$ (GeV/c)	Coverage (%)
1	1.67	0.9	0.6	1.25	0.75	1.1	79.5 ± 3.4
4	1.67	3.8	2.2	6.1	2.9	4.9	81.5 ± 3.1
6	1.67	6.2	3.5	11.5	4.5	8.4	82 ± 3.0

Table 4.2: The results obtained using a set of simulated tracks with P_{True} momentum. The media and the lower/upper bounds of the 90%/68% quantile of the population of estimated momenta and the coverage obtained are reported.

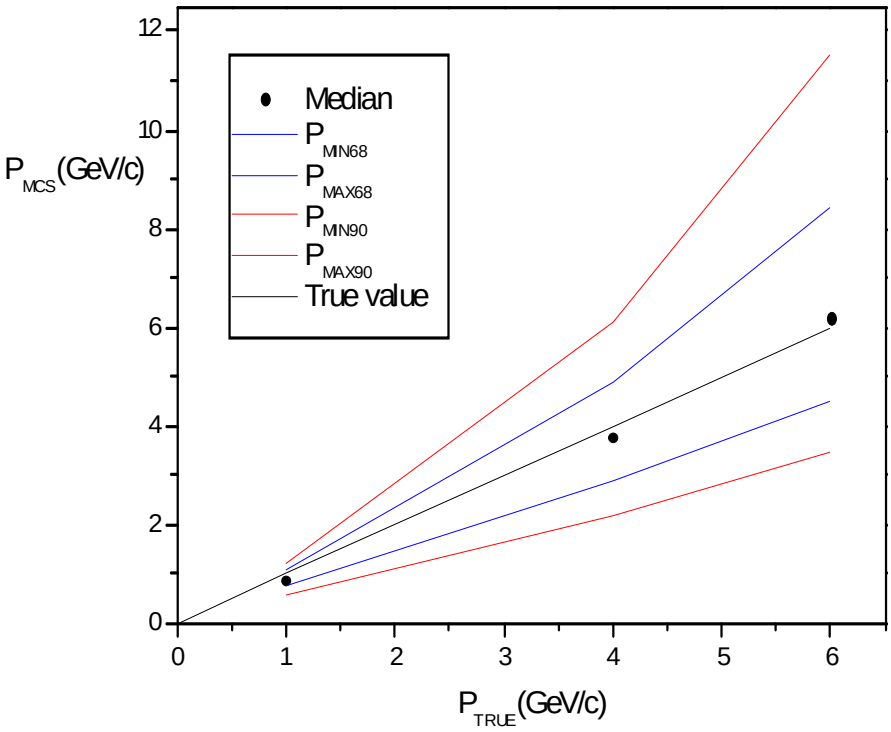

Figure 4.3 The results obtained using a set of simulated tracks with P_{True} momentum are summarised in this plot. The black points mark the median value, the black line is the bisector, where the median points should be, blue/red lines bound the 90%/68% quantile of the population of estimated momenta.

4.4.2. Real data

4.4.2.a. Results on real data from pion test beams

Three different pions beam orthogonal to the plate, having a momentum of 2, 4 and 6 GeV, impinging on lead-emulsion brick were analysed. In order to decouple track reconstruction effects from momentum estimates, only tracks traversing all emulsion sheets were selected. Figure 4.4 shows the track length distribution for the tracks having a momentum of 2 GeV/c (left), 4 GeV/c (center) and 6 GeV/c (righ). In all distributions, two peaks are visible: the first one is due to tracks having a low number of measurements, mostly unrelated to the beam; the second is due to the beam tracks traversing the brick. At least 43 segments out of 57 were required for this analysis; respectively, 3350, 4533 and 801 tracks from 2, 4 and 6 GeV/c samples have been selected.

For these real samples, the measurement error (denoted as $\delta\theta$) is unknown; the determination of this quantity is crucial for momentum estimate accuracy. Real data come from different bricks scanned using different microscopes; then the base-tracks resolution should be tuned for each sample.

To estimate the $\delta\theta$ value the method described in section 4.1.1 was applied: the $\delta\theta$ value for each data set is determined by extrapolating to zero the function $\Delta\theta_{\perp i}(l_i)$ computed considering passing-through tracks in the set. This task can be accomplished only in an ideal case in which the tracks momentum is known i.e when a brick is exposed to a charged particle beam of high intensity, like in this test beam; in the case of tracks from real OPERA data, $\delta\theta$ has to be determined for each microscope using reference plates [81].

The method to infer $\delta\theta$ has been tested on ORFEO data, since, in this case, the $\delta\theta$ parameter has been fixed to 1.67 mrad, during the simulation, then it is known. The left side of Figure 4.5 shows, for example, the fit of the function $\Delta\theta_{\perp i}$ (l_i) obtained considering a set of simulated pions having a momentum of 4 GeV/c. The extrapolation to zero of this function gives a value of 1.65 ± 0.02 mrad for the error to be applied to estimate track momenta, well in agreement with the value set in the simulation. A similar result has been obtained for the other MC samples.

The estimation of the $\delta\theta$ value for the real data was performed for all real samples. The right part of Figure 4.5 shows the fit obtained for a set of reconstructed tracks with 4 GeV/c momentum. The reconstructed value, $\delta\theta$, is 1.62 ± 0.02 mrad. The results obtained for the 2 and 6 GeV/c samples are reported in Table 4.3, and they are used in the likelihood-based software to estimate the momentum of the tracks. In the same table, the median of the momentum distribution obtained for each sample of tracks, and the $P_{min}/P_{max\ (\alpha\ \%)}$ as well as the coverage are reported. They are, also, summarised in Figure 4.6.

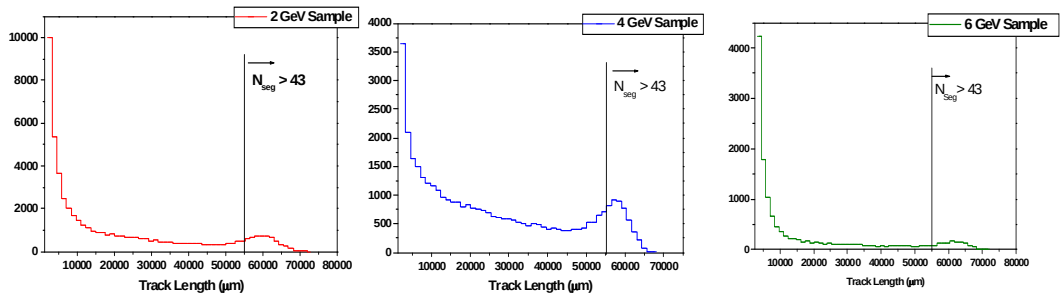

Figure 4.4: The track length distribution obtained considering the 2 GeV/c tracks (left) , the 4 GeV/c (center) and the 6 GeV/c (right)tracks. To estimate the momentum, just tracks having a number of segments greater than 43 have been selected.

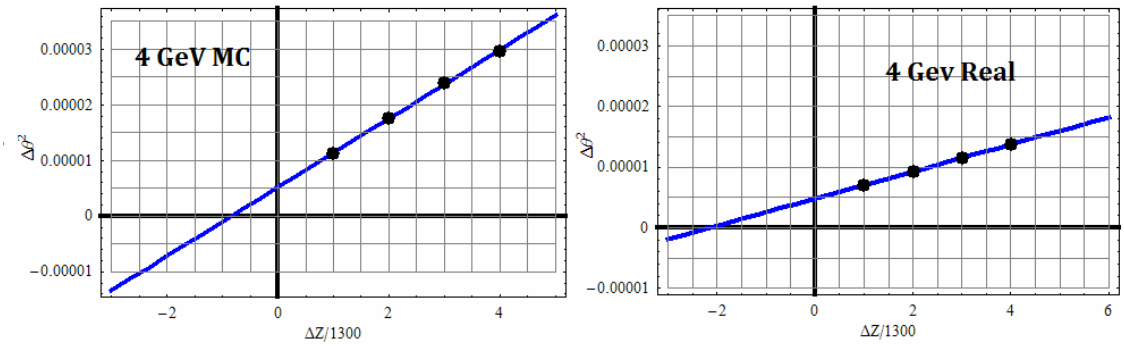

Figure 4.5: The $\Delta\theta^2$ quantity is reported as function of the $\Delta Z/1300$ for a set of simulated tracks with a momentum of 4 GeV/c (left) and for a set of tracks reconstructed in emulsion with momentum of 4 GeV/c (right). The extrapolation to zero of this function gives an estimation of the $\delta\theta$ value

P_{True} (GeV/c)	δθ (mrad)	Median (GeV/c)	$P_{min,90\%}$ (GeV/c)	$P_{max,90\%}$ (GeV/c)	$P_{min,68\%}$ (GeV/c)	$P_{max,68\%}$ (GeV/c)	Coverage (%)
2	1.99	1.9	1.35	2.85	1.55	2.4	80 ± 3.2
4	1.62	4.2	3	7.05	3.4	5.45	86 ± 3.0
6	2.2	5.8	3.5	14.7	4.3	8.7	88 ± 3.0

Table 4.3: The results obtained using a set of tracks reconstructed in the emulsion sheets. The median, the lower/upper quantile of the population (at 68% and 90%) of estimated momenta and the coverage obtained are reported.

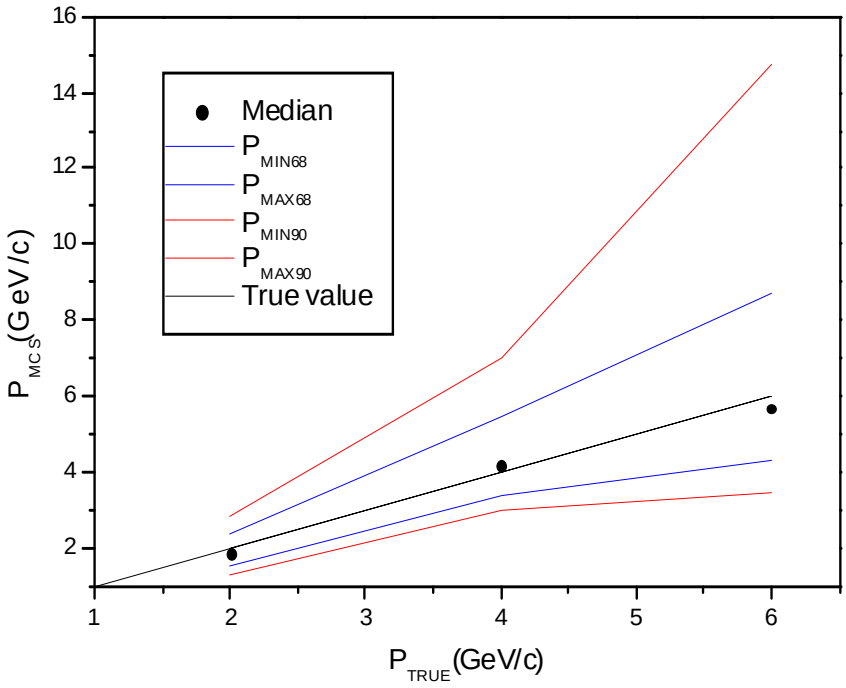

Figure 4.6: The results obtained using a set of tracks reconstructed in a brick exposed to a P_{True} pions beam. The black points represent the median value of the momentum distribution, the black line represents the line on which the point should be (bisector). Blue/red lines bound the 90%/68% quantile of the population of momentum estimates.

4.4.2.b. Results on reconstructed soft-muons

A set of muons with momentum below 6 GeV ("soft" muons) was selected from the data taken during the 2008 run. Figure 4.7 shows an image of the electronic detector for one of such events. The muon momentum was estimated using the likelihood-based software and compared to the value measured by the spectrometer and the value computed using the official software.

In the 2008 run, the Salerno laboratory collected 69 events with a muon at primary vertex; out of these, 20 muons have a momentum, estimated by the spectrometer using bending and range, below 6 GeV/c. The distribution of the number of segments of these tracks is shown in Figure 4.8. Tracks with at least 15 segments were considered in order to have a suitable number of measurements to compute the momentum.

16 muon tracks survive this selection, and their estimated momenta are reported in Table 4.4, as well as the 90% confidence limits (P_{min} and the P_{max}). Also the momentum estimated by the spectrometer and the one estimated with the official software are shown in the same table. In Figure 4.9 and Figure 4.10, these results are summarised: in both plots the points mark the values obtained with the official software (Figure 4.9) and the ones obtained with the likelihood-based software (Figure 4.10). Both sets of data are plotted versus the momentum measured by the spectrometer; the black line (bisector) shows where points should lie.

Figure 4.11 shows the difference between the values obtained with the official software and the ones obtained with the likelihood-based software versus the momentum measured by the spectrometer.

The values obtained with the likelihood-based software are under-estimated with respect to the spectrometer values. This effect is probably due to the plate misalignment.

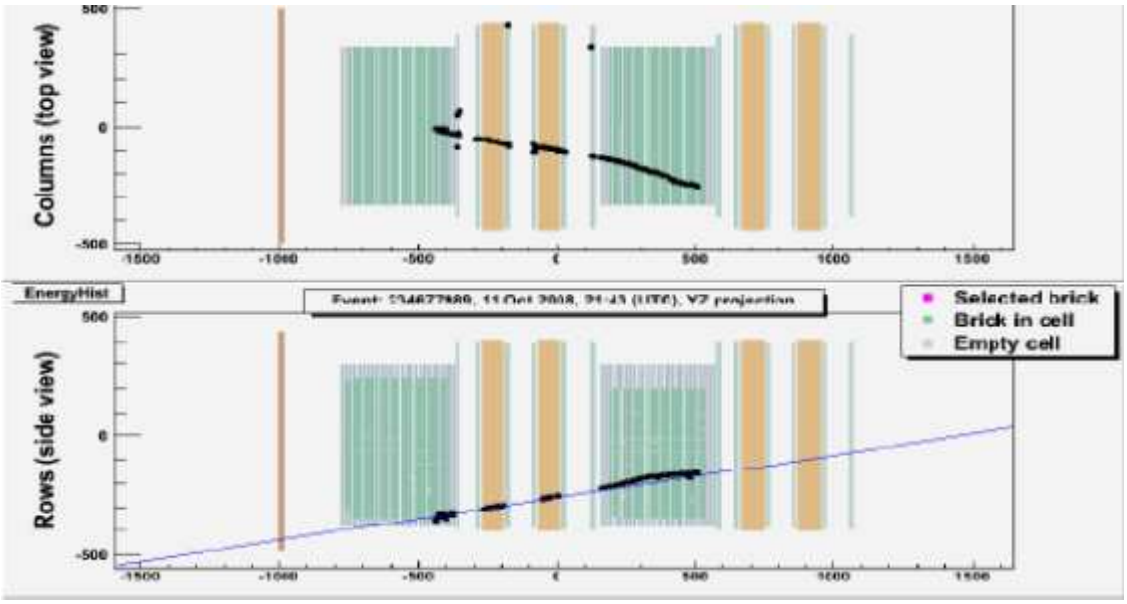

Figure 4.7: Image of the electronic detector for an event with a soft muon.

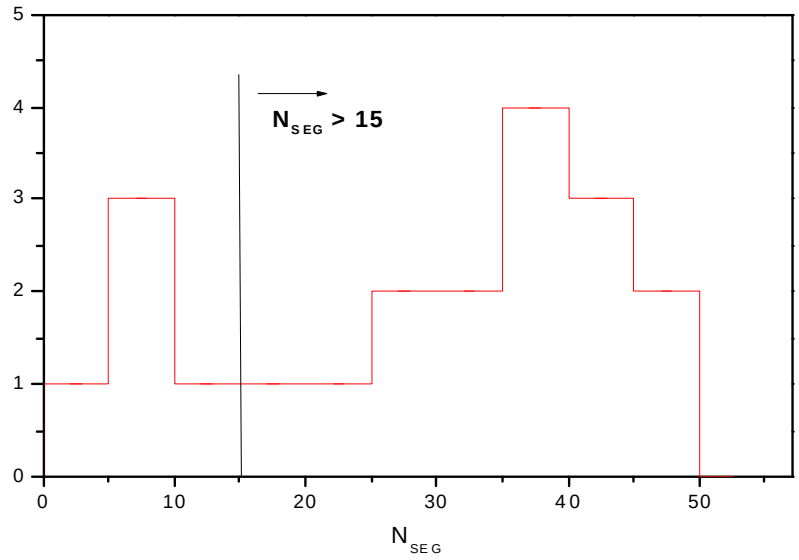

Figure 4.8: Distribution of the number of segments of soft muon tracks.

P_{spect} (GeV/c)	$P_{likelihood}$ (GeV/c)	$P_{L,min,90\%}$ (GeV/c)	$P_{L,max,90\%}$ (GeV/c)	$P_{official}$ (GeV/c)	$P_{O,min,90\%}$ (GeV/c)	$P_{O,max,90\%}$ (GeV/c)
1.82	4.95	2.7	10.6	4.78	3.14	10.6
2.03	1.6	0.5	7.45	2.94	1.7	10.6
3.21	1.2	0.6	2.3	1.58	0.9	6.63
4.75	4.55	1.5	62.65	1.41	0.77	8.71
5.95	2.7	1.2	5.75	2.65	1.42	18.8
2.80	1.85	0.5	100	5.38	2.71	336.4
3.44	1.85	0.75	3.65	0.49	0.25	13.11
3.48	5.85	1.95	100	3.69	1.93	43
3.56	0.7	0.25	1.45	2.43	1.23	151
3.66	5.8	3	14.4	3.87	2.75	6.51
5.81	3.9	3.3	4.9	7.45	3.75	465
1.77	1.25	0.4	2.8	1.51	0.8	13.9
5.82	0.95	0.65	1.4	1.44	1.1	2.09
2.99	2.65	1	6.35	1.96	1.05	14.6
3.07	0.4	0.25	0.65	2.15	1.2	10.42
3.43	1.75	0.8	3.65	1.34	0.77	5.33

Table 4.4: Some details about the soft muons found in Salerno during the 2008 run. The momentum measured by the spectrometer, the one estimated by using the official software and by using the likelihood-based software are reported. Also the confidence limits are shown.

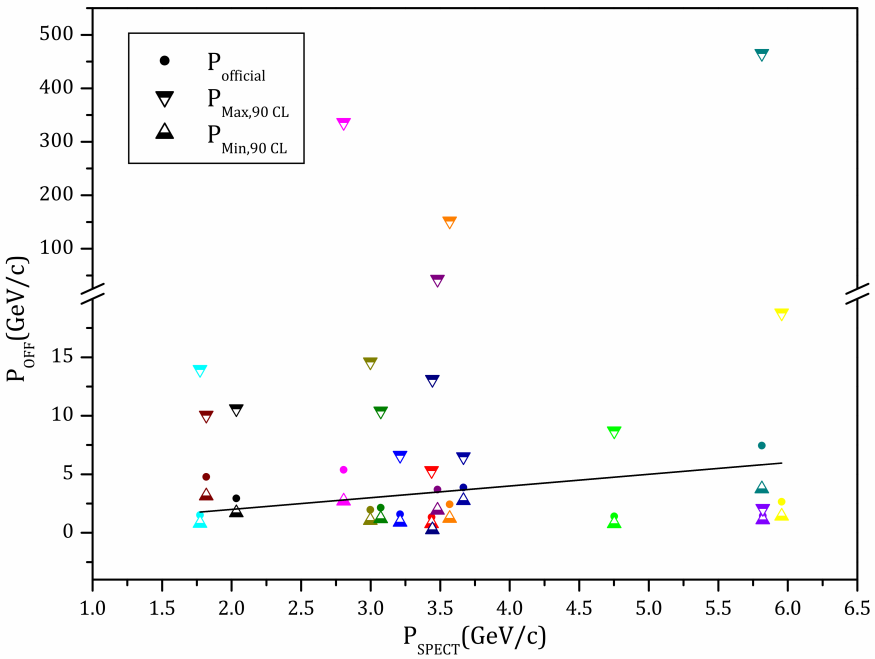

Figure 4.9: Summary of the results obtained on the sample of soft muons found in Salerno during the 2008 run. The measured momenta are plotted as a function of the spectrometer estimate. The points are the values estimated by the official software. The triangles bound the 90% confidence region.

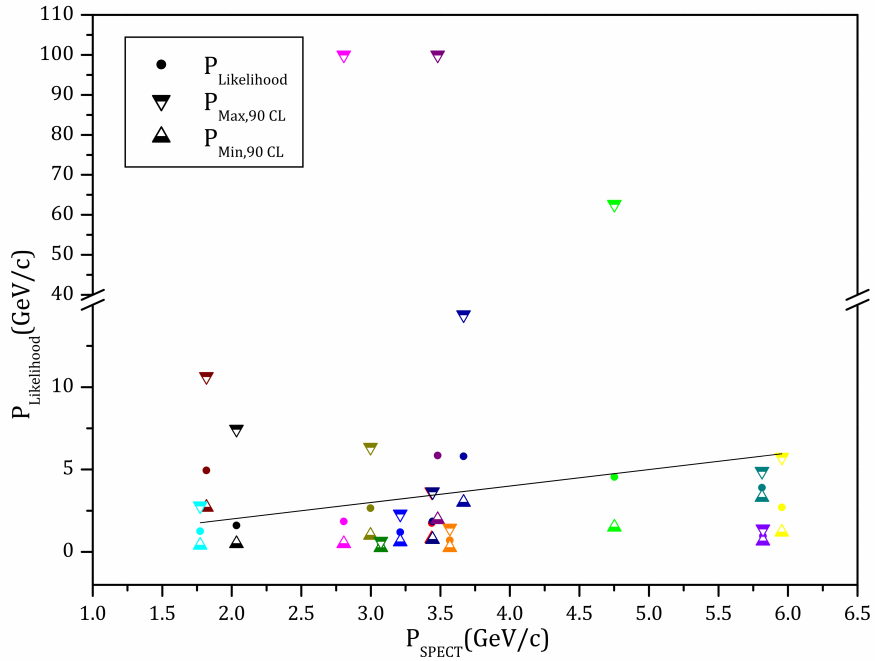

Figure 4.10: Summary of the results obtained on the sample of soft muons found in Salerno during the 2008 run. The measured momenta are plotted as a function of the spectrometer estimate. The points are the values estimated by using the likelihood-based software. The triangles bound the 90% confidence region.

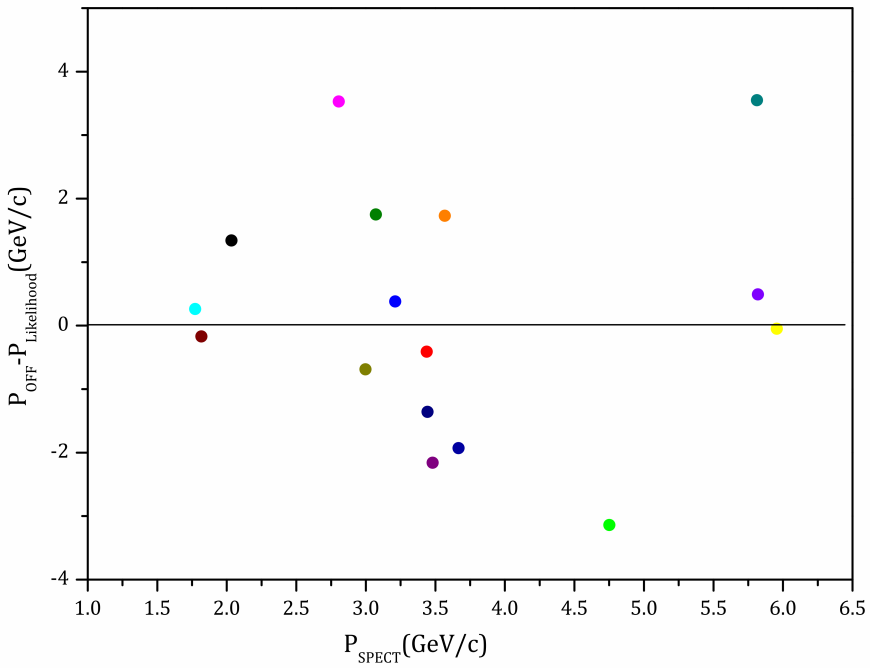

Figure 4.11: Difference between the values obtained with the official software and the ones obtained with the likelihood-based software versus the momentum measured with the spectrometer.

Chapter 5

Evaluation of background from hadronic interactions

The appearance of the τ lepton is identified in OPERA by the detection of its characteristic decay topologies, either in one prong (electron, muon or hadron) or in three prongs. In this thesis the tau-to-one-hadron decay channel was investigated. An important source of background to this channel is due to hadron re-interactions; hence understanding this background is a key to the success of the OPERA experiment.

To perform this task a large simulation sample of 160 millions of events was generated by FLUKA by shooting pions, protons and kaons onto 1 mm-thick lead plates. All particles produced in the interactions were recorded and this allowed to perform dedicated calculations by applying the same topological cuts as in the single hadronic prong tau decay channel ("signal region") and to evaluate the background. The results obtained with the FLUKA MC productions were compared with the one of the experiment Proposal.

Another important task is to prove that the simulation reproduces the experimental data outside the "signal region", so that it can be trusted for background evaluation.

5.1. Definition of the "signal region"

The main source of background to the hadronic decay channel is due to re-interactions in lead of hadrons produced in ν_μNC (neutral current) and in ν_μCC (charged current) interactions in which the primary muon is not identified. Although the muon identification efficiency is high, the latter class of events gives a background that is comparable to that from ν_μNC events (~10^{-5} N_{CC} ν_τ interactions, where N_{CC} is the total number of ν_μCC collected).

The event topology is the same both for signal and background: the re-interacting hadron attached to the primary vertex might be mis-identified as a τ; both τ decay and hadron interaction have an outgoing hadron (see Figure 5.1).

In order to keep the background as low as possible, several kinematical cuts are applied. The τ decays close to the primary vertex; given the lead plate containing the neutrino interaction vertex, 99% of τ decay before the third lead plate from the vertex. Then, the decay volume extends to two lead plates downstream of the neutrino interaction lead plate.

The kinematical cuts required to select a τ candidate that decays to hadronic channels are:

- The transverse momentum of the daughter with respect to the parent track, denoted as P_t, must fulfill $P_t > 600$ MeV/c if no γ's are attached to the decay vertex and 300 MeV/c otherwise. The harder cut is justified by the relatively small $< P_t >$ (~100 MeV/c) in pion interactions.
- P_{dgh} (the momentum of the daughter track) > 2 GeV/c. This selection cuts low energy hadrons.
- θ_{kink} (kink angle between the parent and daughter track) > 20 mrad.

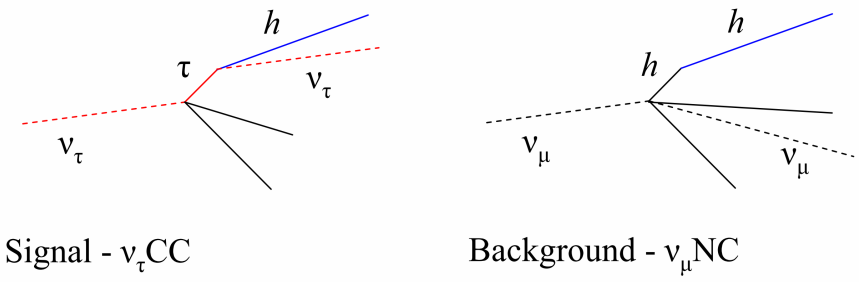

Figure 5.1: Signal and background topologies.

5.2. Results from simulations

This section reports a comparison between the experiment Proposal estimation of hadronic interaction background and a more recent evaluation obtained by FLUKA. In both cases the interesting background has been evaluated by applying the same topological cuts as in the τ→h decay channel.

5.2.1. Estimation from experiment Proposal

In the experiment Proposal [56], background was evaluated by simulating 1×10^7 NC and CC events by GEANT 3.21. The results obtained are reported in Table 5.1. The

analysis was performed taking into account only the background from neutral current events with high multiplicity (HM)[3]. The number of events expected is 2.1 that is normalized to 10^6 DIS events (including also ν_μCC events). The cross section ratio favours CC events (σ_{NC}/σ_{CC} ~ 1/3); hence the probability of having an hadronic interaction considering just HM NC events is 8.4×10^{-4}.

The computed probability includes the location efficiency, ε_{loca}, the efficiency due to kinematical cuts, $\varepsilon_{kin,}$ and the probability for an hadron at primary vertex to be mis-identified as a muon $\varepsilon_{fake(\mu).}$

$$P_{NC,HM} = \varepsilon_{loca} \times (1 - \varepsilon_{fake(\mu)}) \times \varepsilon_{kin} \times P_{fake(sign)}$$

where $P_{fake(sign)}$ is the probability for a background interaction to occur within 2 mm of lead per NC event. The Proposal gives the following estimates for the mentioned efficiencies:

$\varepsilon_{loca} = 0.53$

$1 - \varepsilon_{fake(\mu)} = 0.9$

$\varepsilon_{kin} = 0.2$

By using these values the interaction probability per event is:

$$P_{fake(sign)} = 8.75 \times 10^{-5} \text{ (4)}$$

Expected background				
Events	**HM**	**LM**	**Short[5]**	**TOTAL**
ν_μ NC	**2.1**	0.6	4.1	6.8
ν_μ CC	2.3	<<0.1	2.0	4.3
TOTAL	4.4	0.6	6.1	11.1

Table 5.1: Expected background from hadron re-interactions. The contribution as a function of the track multiplicity at the primary vertex is also given. The numbers are normalised to 10^6 DIS events [56] (HM-High Multiplicity; LM- Low Multiplicity).

5.2.2. Estimation from FLUKA simulation

The FLUKA simulation was performed considering monochromatic beams of pions/protons/kaons, impinging perpendicularly on 1 mm-thick lead plate. For each type

[3] The High Multiplicity (HM) events are the one for which at least another track besides the parent is fully measured whereas in the Low Multiplicity (LM) events only the parent track is measured.

[4] this probability decreases to 1.75×10^{-5} per NC event if one takes into account the cuts on the global event kinematics (see next chapter for more details).

[5] See section 2.2.1 for the *short decay* definition

of incoming particle, protons, pions (π^+ and π^-) and kaons (K^+ and K^-), 2 million of events for various momenta, in the range [1,15] GeV, were simulated. About 160 million of events overall were produced, equivalent to 160 km of hadronic track length [82].

By analysing the results of these interactions, the probability of having one-prong topology was estimated. Indeed, this probability depends on the incoming particle momentum, on the daughter momentum and on the transverse momentum of the daughter track with respect to the parent track (P_t). To compute the probability distribution, one needs to apply the same kinematical cuts used to select a tau candidate and described in the section 5.1. In Figure 5.2, some distributions for kinematical quantities obtained considering only interactions with a single outgoing track are reported: the hadronic spectra (left), the kink angle (center) and the P_t (right). The interesting region is to the right of the dotted red line showing the cut in the experiment Proposal [56]. The plots clearly show that the amount of the events exceeding the cuts is some orders of magnitude smaller than most common scattering events [83].

The probability of producing an interaction with the same topology as tau decays was parameterised as a function of the incoming particle momenta and the P_t cut used in the analysis. A different cut is performed on P_t depending on the presence of photons attached to the vertex. The presence of photons, being an additional constraint on the event topology, allows to release the P_t cut by keeping a constant level of background and improving the signal efficiency. The two situations related to the presence or absence of photons were separately analysed.

In the left part of the Figure 5.3 the distribution of the number of photons produced in a 5 GeV pion interactions is shown, restricted to photons having an energy greater than 0.5 GeV [83]. The mean value of photons produced in the final state is 0.32×10^{-2}. However when the kinematical cuts are applied by requiring a high P_t and when the emulsion constraints are reproduced (inefficiency for tracks at slope > 1.0 and for low momentum protons) the distribution changes significantly, since very often photons balance the scattered particle (Figure 5.3 - center and right). The mean number of photons surviving this cuts is about 2.12 (then there is an increase of about two orders of magnitude) and the mean energy of such photons is 1.56 GeV [83].

By using this sample, the probability of having an interaction was studied as a function of the energy of the incident particles, with and without photons in the final state, as shown for the π^+ sample in Figure 5.4. The red points stand for the probability values obtained considering events having one visible charged particle in the final state and passing the kinematical cuts. Since no photons are detected in such interactions, events with $P_t > 600$ MeV/c were selected. The probability distribution has a maximum for an energy value of incident pion about 4 GeV and then decreases for high energy values.

The blue points stand for the values obtained considering single prong events passing the kinematical cuts with photons in the final state. The P_t threshold applied in this case is 300 GeV/c. From the plot it is evident that it is more likely to have in the final state a configuration that includes photons when the energy of the incident pion increases.

The total probability, shown by the black points, is obtained by combining these two results, and this is reflected in the shape of the distribution: for low energy of incident pion, the contribute given by events with no photons in the final state dominates, whereas for high energy the contribute given by the events with detected photons is more significant. The same distributions are reported also for the other incident particles

considered in the simulation (see Figure 5.5) and in each of these cases the two contributes are well separated.

By using these results the probability for a background interaction to occur over 2 mm of lead, the maximum decay length considered, and to satisfy the selection criteria for the reconstruction of the kink decay topology and its kinematics is $1.9 \pm 0.1 \times 10^{-4}$ per event[6]. This estimated value is 2.2 times larger than the value of the experiment Proposal [56], but it is based on an upgraded and more reliable simulation tool. [83].

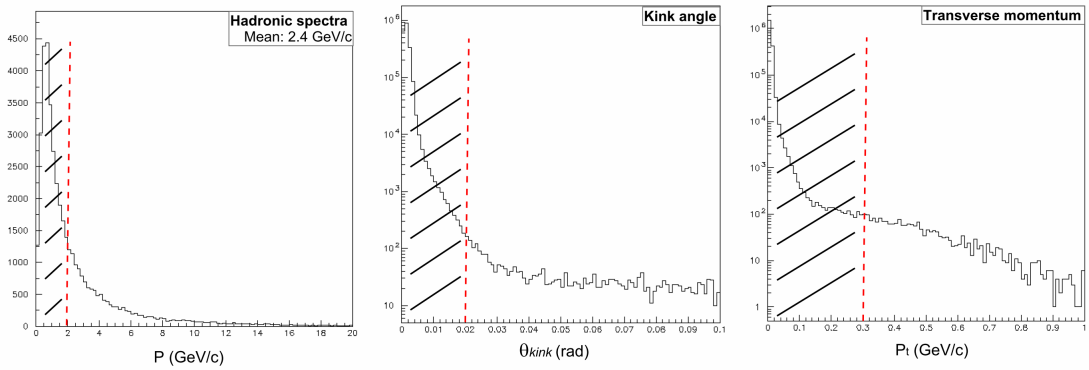

Figure 5.2: Distributions of daughter momenta (left), kink angle (center) and transverse momentum (right) induced by a beam of 5 GeV/c of π^+. The dotted red line shows the experiment Proposal cuts; the shaded area is the excluded region [83]

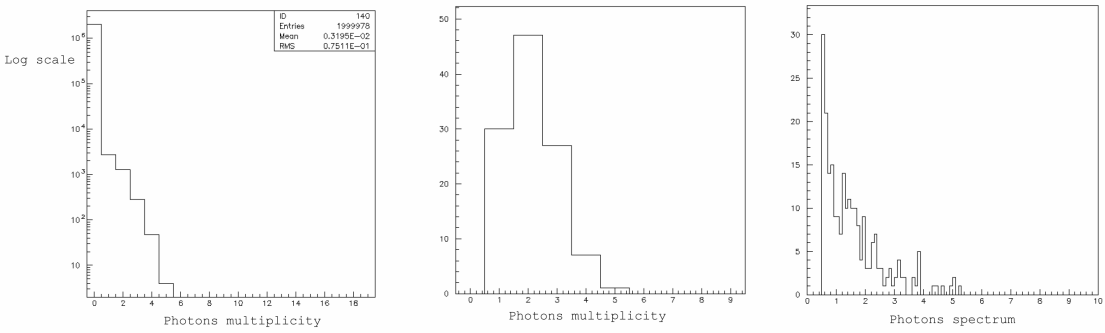

Figure 5.3: Multiplicity of photons produced in the interaction of a beam of 5 GeV pions with 1 mm of lead before (left) and after (center) the kinematical cuts and their energy after the cuts (right) [83]

[6] This probability decreases to $(3.8 \pm 0.2) \times 10^{-5}$ per event when taking into account the cuts on the global event kinematics (see next chapter for more details).

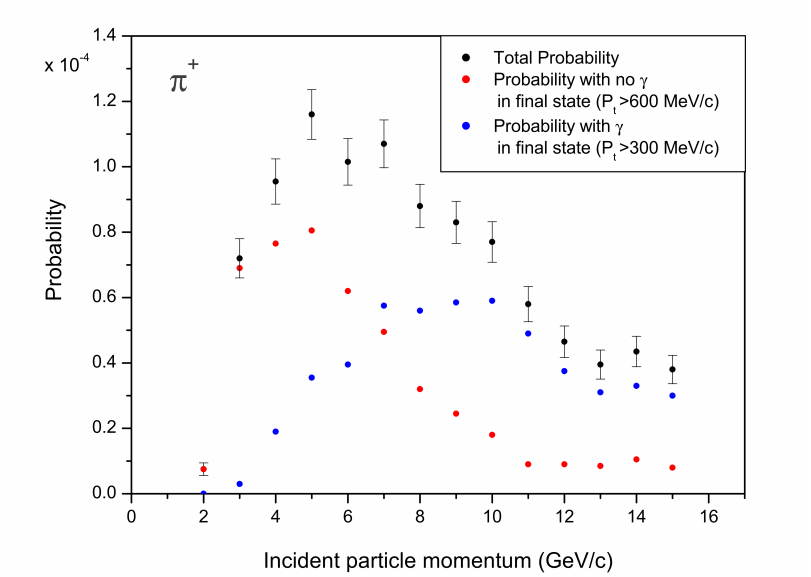

Figure 5.4: Probabilities (as a function of incident π^+ momentum) to obtain the kink topology selected for the $\tau \rightarrow h$ channel on simulated hadronic interactions.

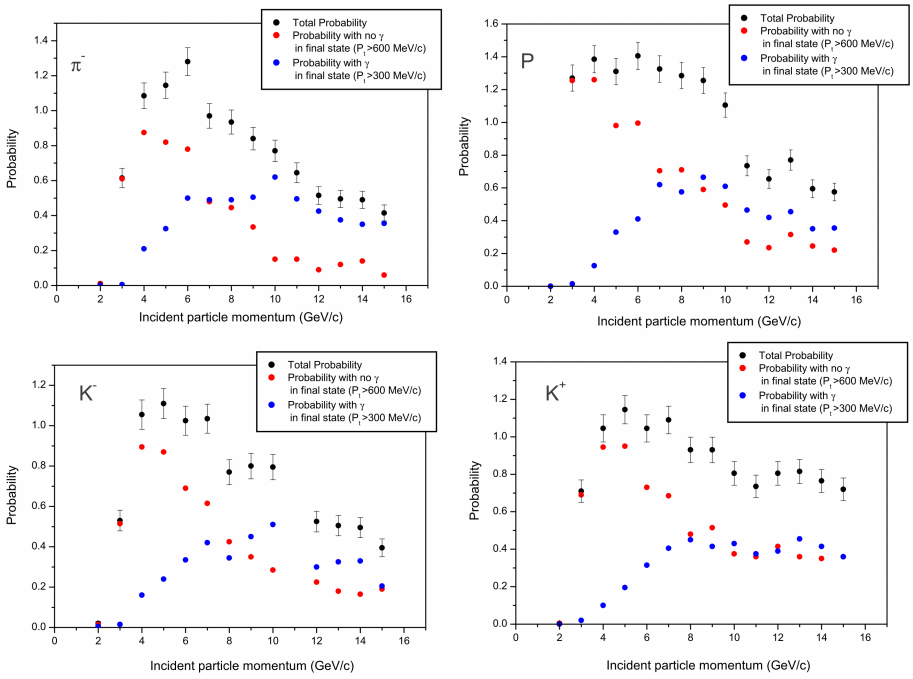

Figure 5.5: Probabilities as a function of incident particle momenta to obtain the kink topology selected for the $\tau \rightarrow h$ channel on simulated hadronic interactions for several kinds of incident particle: π^- (top left), proton (top-right), K^- (bottom- left) and K^+ (bottom right).

5.3. Cross–check with real data

Two experimental cross-checks of the one-prong hadron background calculation were performed, though with small statistics so far. The first implies the use of the Scan-Forth data collected by the Collaboration and the second is a comparison to a sample of hadronic interactions collected in a brick exposed to a π^- beam with 4 GeV/c momentum.

5.3.1. Comparison with Scan-Forth data

The procedure to locate and study a neutrino interaction was described in Chapter 3. As explained, the definition of the primary vertex is the starting point for the analysis of a neutrino interaction. In order to complete it, one needs to acquire more information about the kinematics of the event. The Scan-Forth (SF) procedure allows achieving a more precise evaluation of the track momentum (see Chapter 4) and can also find hints for a possible re-interaction of the particle followed downstream.

In the Salerno laboratory, the analysis on the 2008 run has been completed whereas the one of events from 2009 and 2010 runs is ongoing. For each primary interaction located, the tracks to be followed down were selected using the following criteria:

- Track must have almost three segments
- Track slope < 0.6

78 events from 2008 run have been located in Salerno and the number of the tracks attached to that primary vertex that were followed to their stopping point is 185 (including muons). In 42% of cases the SF is not needed: this happens for quasi-elastic interactions in which the Scan-back (SB) track stops and there are no more tracks attached to the primary vertex, or when the neutrino interaction is enough close to the downstream edge of the brick so that the vertex volume contains it.

The hadron sample includes 125 tracks; 37 of them are the SB tracks used to locate the primary interaction point. 42% of the remaining hadrons was discarded did not meet the selection criteria. Then 51 hadrons needed to be followed down, corresponding to 4.1 m of track length. In 9 cases the track disappeared, and the required additional scanning confirmed the presence of a secondary interaction. In Table 5.2 the values of some kinematical quantities computed for these interactions have been reported: the flight length (FL), the impact parameter (IP), the kink angle (θ_{kink}), the estimated momentum of the parent (P_{parent}) and the daughter ($P_{daughter}$) track as well as the $P_{t.}$ In two cases the information about the daughter track is missing because the track observed in the emulsion is black. It means that an interaction occurs in this point but the track observed (made of just by two or three segments) is probably a proton with low energy.

In Figure 5.6 an hadronic interaction reconstructed for the event #23611571, located in the brick #1124128 is shown. 4 tracks are attached to the primary vertex: 2 are the SB tracks (yellow line); 1 is a large angle track (low momentum); the last track was followed down (red line) and it is found to stop 26 plates downstream of the primary interaction point. A volume scan was performed around this point (5 plates upstream and 5 plates downstream) and a single prong interaction was found. The daughter track

was followed down to the CS doublets (blue line), where it was confirmed to belong to the event (CS doublet do not have the background due to cosmic rays that are used to produce alignment patterns on the ECC brick).

The OPERA Scan-Forth (SF) sample, taking into account also the results from the other laboratories [85], total about 8.6 m of track length, along which 23 single prong hadronic interactions have been located. The distribution on the plane $P_{daughter}$ vs. P_t is shown in Figure 5.7. Since no event has been found in the signal region, this measurement allows to set an upper limit on the kink probability of 1.54×10^{-3} kinks/NC event over 2 mm of lead. This number was computed by considering the following expression:

$$N_{eq}^{NC-like} = \frac{L}{L_{decay} \times \langle m \rangle} = \frac{8600}{2 \times 2.88} = 1493 \qquad 5.1$$

where L is the total track length, L_{decay} corresponds to the τ decay length and <m> is the mean multiplicity at the primary vertex. The relation 5.1 sets the correspondence between the number of NC events and a track of length L. The upper limit with 90% of confidence level of a Poissonian distribution with zero observed events is:

$$N_{bg}^{\tau \to h} = \frac{2.3}{N_{eq}^{NC-like}} = \frac{2.3}{1493} = 1.54 \times 10^{-3} \qquad 5.2$$

This limit is one order of magnitude larger than the kink probability evaluated from the simulation. However the size of the sample analysed is not large enough; in order to estimate the hadronic background from data a sample of about 100 m of hadronic track length will be needed [86].

Brick #	FL (mm)	IP (μm)	Θ_{kink} (rad)	P_{parent} [P_{min} - P_{max}] (GeV/c)	$P_{daughter}$ [P_{min} - P_{max}] (GeV/c)	P_t [P_{min} - P_{max}] (GeV/c)
1051282	9.98	4.7	0.060	1.25 [0.98 – 1.74]	0.83 [0.64 – 1.18]	0.049 [0.038 – 0.060]
1071446	37.40	9.3	0.518	1.70 [1.14 – 3-37]	0.59 [0.37 – 1.47]	0.292 [0.183 – 0.728]
1073104	27.08	0.1	0.544	1.50 [0.60 – 2.80]	0.51 [0.34 – 1.05]	0.264 [0.176 – 0.543]
1087210	43.19	6.3	0.435	3.60 [2.50 – 6.47]	0.48 [0.30 – 1.09]	0.201 [0.126 – 0.458]
1123551	12.79	5.7	0.111	0.75 [0.53 – 1.10]	0.72 [0.57 – 1]	0.080 [0.063- 0.110]
1124128	34.22	3.2	0.089	1.96 [1.10 – 2.67]	1.56 [1.31 – 3.91]	0.175 [0.117 – 0.350]
114776	14.69	2.4	0.418	1.00 [0.35 – 2.15]	0.43 [0.32 – 1.13]	0.174 [0.130 – 0.459]
1054668	9.61	9.0	0.039	BLACK TRACK		
1058161	7.50	6.0	0.077	BLACK TRACK		

Table 5.2: Kinematical quantities measured for the hadron interactions reconstructed in Salerno in the 2008 run: flight length (FL), impact parameter (IP), kink angle (θ_{kink}), momentum of the parent (P_{parent}), momentum of the daughter ($P_{daughter}$) and the transverse momentum of the daughter (P_t). The P_{min}/P_{max} value corresponds to the minimum/maximum value of the momentum estimated from multiple Coulomb scattering with 90% confidence level.

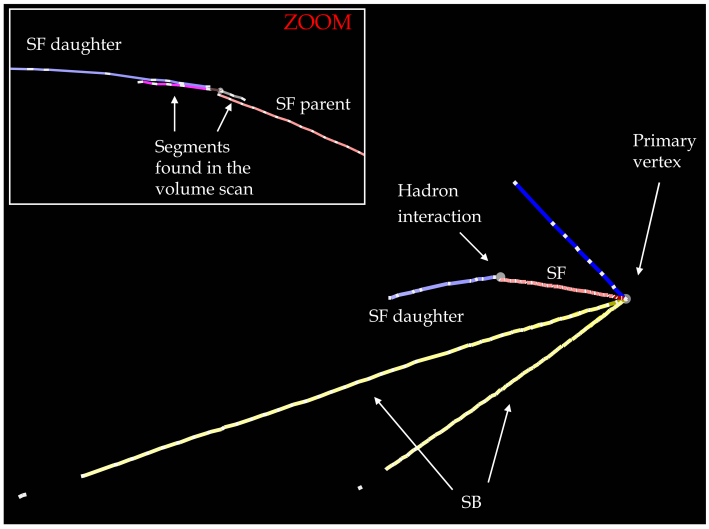

Figure 5.6: An example of an hadron interaction reconstructed in Salerno. The yellow tracks are the SB tracks, the red track is a SF track that stops in the brick and interacts with the lead producing an outgoing hadron (purple). The zoom view enhances the track segments found in the volume scan and in the SF of the parent and the daughter.

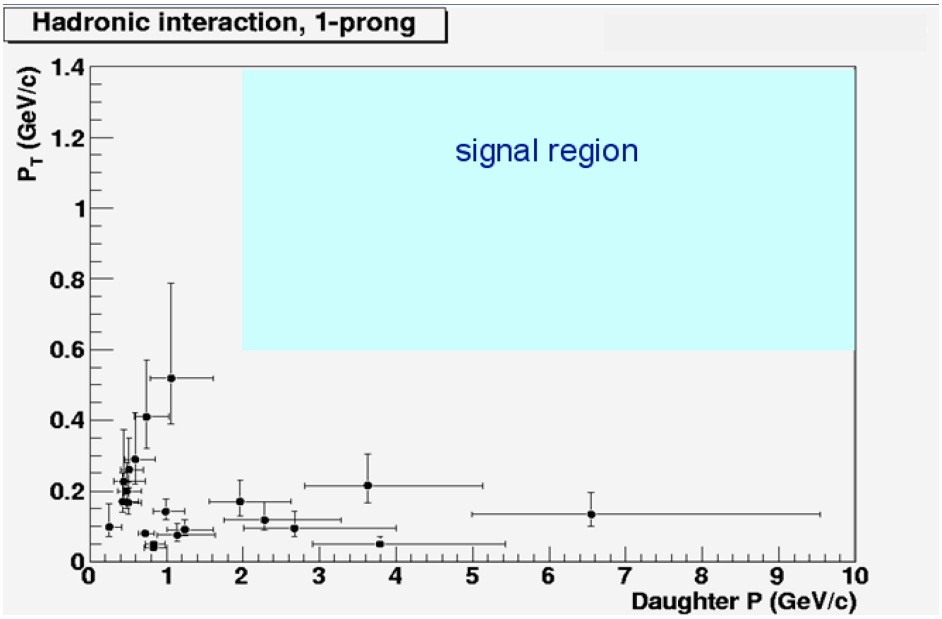

Figure 5.7: Distribution of the transverse momentum vs. particle momentum for kink candidates n the SF sample [87].

5.3.2. Comparison with pion test-beam

A brick exposed to the 4 GeV hadronic test-beam provided a data sample for which currently 20 m of track length have been scanned. 119 hadronic interactions with at least one prong greater than 20 mrad have been found out of 564 incoming pions. The fraction of hadronic interactions is (22.1 ± 1.7)% in good agreement with (22.1 ± 0.4)% expected from the FLUKA simulation. Out of the 119 events, 42 (7.4 ± 1.1)% showed a single prong topology; this has to be compared to the Monte-Carlo expectation (7.6 ± 0.3)%. For 29 out of the 42 kinks it was possible to measure the daughter momentum and determine the interaction kinematics. An example of a reconstructed interaction is reported in Figure 5.8 [88]

A comparison with the FLUKA simulation is reported in Figure 5.9 including several variables, the number of backward going tracks, the multiplicity of the daughters, the kink angle, the momentum and the P_t for kink events for which the kinematical measurements were possible, and the P_t of each single prong for multi-prong events. All these variables are in good agreement with the simulation showing the capability of FLUKA to reproduce well the general features of hadronic interactions in ECC bricks. These results are preliminary and the analysis of these data is still in progress in order to increase the statistics.

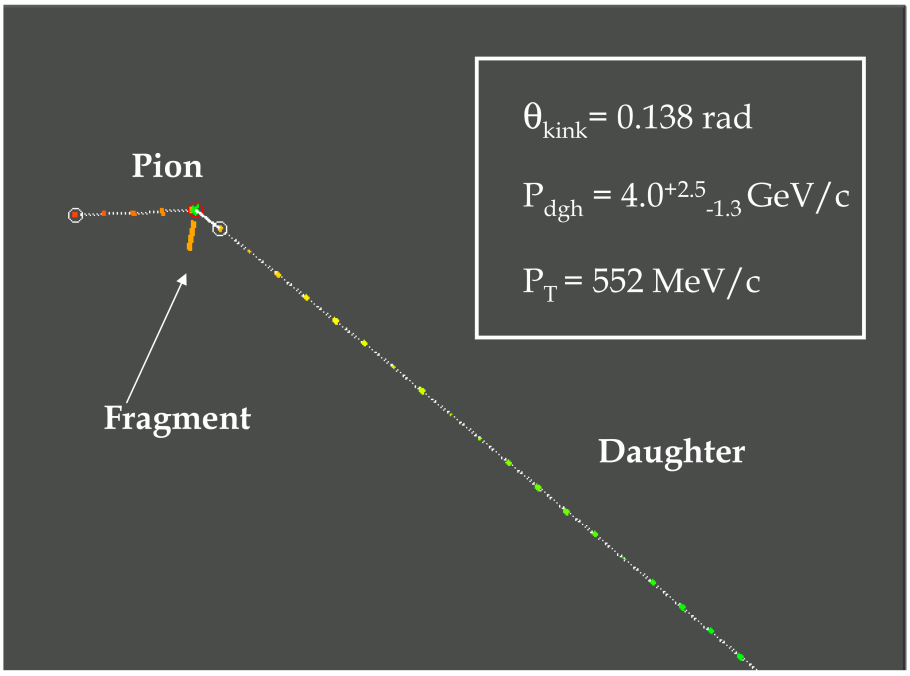

Figure 5.8: An example of a hadron interaction reconstructed in a brick exposed to 4 GeV/c hadronic beam.[88]

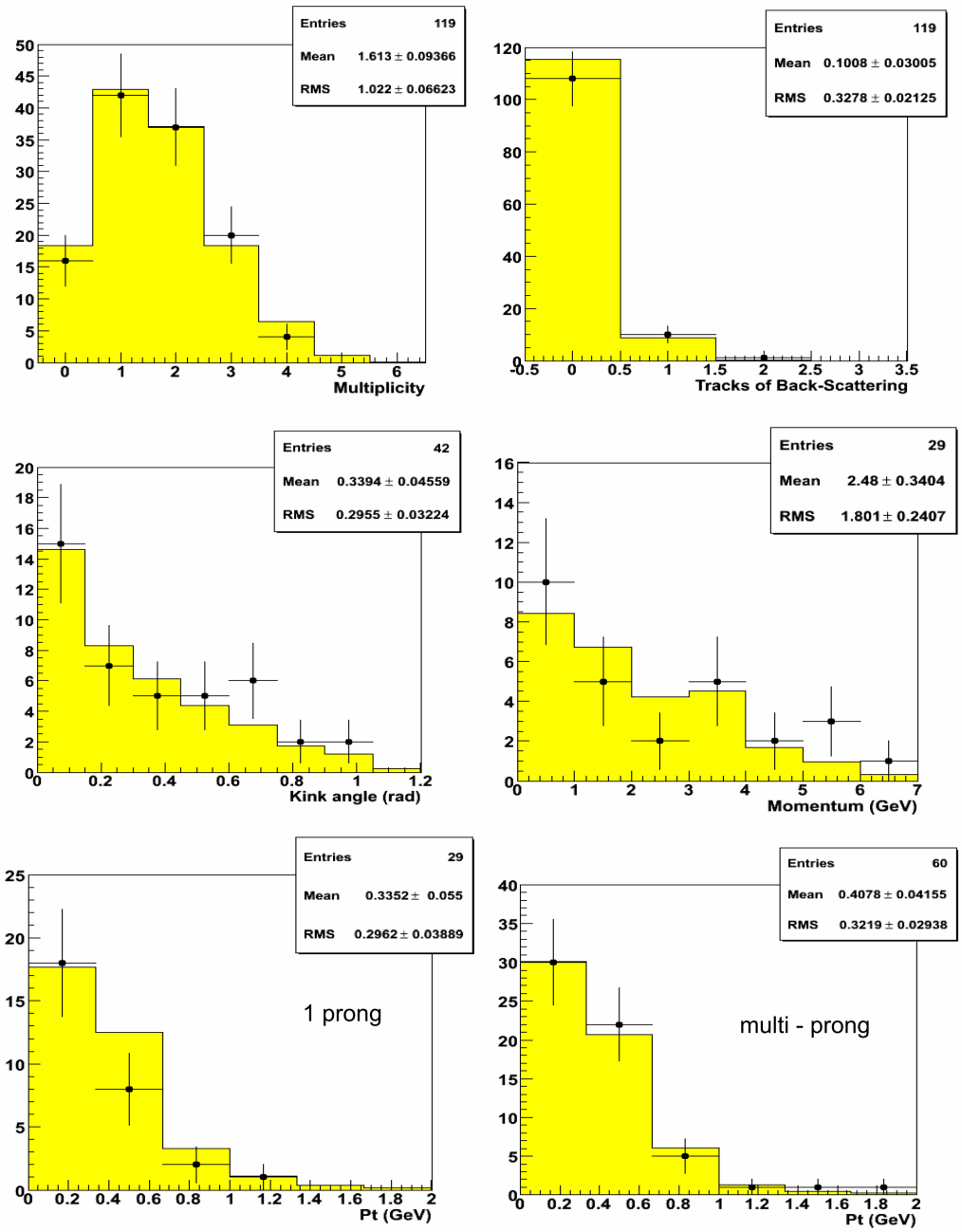

Figure 5.9: Data/MC comparisons for several distributions obtained with the hadronic interaction sample reconstructed in a brick exposed to a 4 GeV/c hadronic beam. Top - Left: multiplicy of forward tracks; Top-right: multiplicity of backward tracks; Center -left: kink angle; Center-right: Momentum of daughter track; Bottom-left: P_t of single prong for single-prong events; Bottom-right: P_t of each prong for multi-prong events.[88]

Chapter 6

Kinematical study for $\tau \rightarrow h$ decay

In the previous chapter an important source of background was evaluated for the tau to hadronic decay channel from hadronic re-interactions. A τ decay to single hadron features the same topology as the hadron re-interactions (see section 5.1); several cuts are applied both at the decay vertex and at the primary vertex to discriminate the signal from background.

The analysis at the decay vertex has been shown in detail in Chapter 5. Here the attention is focused on the kinematical analysis applied to the primary vertex: the discriminating variables suggested by the experiment Proposal will be described and analysed. In addition, in the section 6.5, other variables that might be used to discriminate the signal and the background will be taken into account.

The analysis was performed on a set of Monte-Carlo data, by including a state-of-the-art simulation of the real conditions of data taking and processing.

6.1. The primary vertex analysis

In the experimental Proposal two variables are proposed to perform the kinematical analysis at the primary vertex:

- $P_{t,miss}$, defined as the missing transverse momentum at primary vertex. The standard requirement is $P_{t,miss} < 1$ GeV. It is expected that $P_{t,miss}$ in ν_μNC events be larger than in ν_τCC.
- φ angle, defined as the angle, in the neutrino transverse plane, between the parent track and the total momentum of the hadron system. The τ and the hadronic system are back-to-back in the transverse plane whereas, in the case of

hadronic re-interactions, a hadron faking a $\tau \rightarrow h$ decay is produced inside the hadronic shower. Therefore, for the tau candidate the φ angle is required to exceed $\pi/2$. (see Figure 6.24, Figure 5.1)

6.2. Monte-Carlo sample description

Neutrino event generation, in the OPERA experiment, uses the NEGN neutrino generator, derived from the NOMAD experiment. NEGN is based on an intra-nuclear cascade model (INC) in which the propagation of hadrons produced in neutrino interactions is taken into account [89].

Some adaptations were needed for the OPERA experiment: the description of the beam, the neutrino energy, the CNGS target and the output format. Several thousands of neutrino events were created and grouped in the so-called beam-files, separating CC from NC interactions. For the tau and charm analysis a dedicated set of beam-files containing tau or charm events were produced. Each file contains also information about the secondary (decay) vertices.

This is the first step of the MC files production. Particle track propagation inside the detector is done with the electronic detector simulation software named OpRelease.

The analysis performed in this thesis is done by using the pure CC and NC interactions collected in the beam-files; track propagation in the ECC is simulated only when needed.

Three MC samples were considered:

- 50,000 ν_μCC interactions with a muon in the final state attached to the primary vertex; this sample was used as a *test sample* to tune the variables used to discriminate between signal and background.
- 50,000 ν_τCC interactions with a tau lepton attached to primary vertex. For each event analysed, information about particles produced both at the interaction vertex and at the decay vertex were used to compute the kinematical quantities.
- 50,000 ν_μNC interactions with a muonic neutrino in the final state.

The interesting variables were computed for each event of each sample by considering various scenarios: the starting point is an ideal situation in which one assumes that the momenta, the positions and the slopes of each particle are exactly known. Then, the MC information was degraded: in the first step, in order to simulate the measurement errors, particle slopes and momenta were smeared; in the second step, the effects due to the emulsion detector performance were simulated, as detailed in the next section.

6.2.1. Sample with simulation of experimental resolutions

The kinematical variables are modified by including measurement errors on momenta and slopes: the momentum of a charged particle is computed by its multiple Coulomb scattering in the emulsion sheets. A $\Delta p/p$ resolution of 20%, independent of the energy, was assumed for all charged particles [56]. Neutral hadrons were totally neglected

because they are undetectable in the emulsion, so it is impossible to give an estimation of their momenta. Pions, kaons and protons having a momentum exceeding 10 GeV/c were cut off at 10 GeV/c. This is a practical constraint imposed by the method (see Chapter 4) used to estimate the momentum in the emulsion: the multiple Coulomb scattering of a particle with high momentum is masked by measurement errors. This constraint was not applied to the muons: indeed, in OPERA the best momentum estimate for muons is produced by the muon spectrometer rather than emulsion plates.

Quantities were smeared by picking a random value from a Gaussian distribution centerd on the true value and with a width controlled by the particle energy. Figure 6.1 shows the momentum distribution of charged particles attached to the primary vertex, produced in several ν_μCC interactions. The distribution obtained with the non-smeared data (right) is compared to the one of smeared data (left): in the latter, the peak observed at 10 GeV/c is the consequence of the introduction of a cut off on the momentum value. Such momentum distributions were obtained for charged particles produced in ν_τCC and ν_μNC interactions.

Also the angular resolution has to be reproduced in the MC data. In a single emulsion sheet, tracks are reconstructed by connecting micro-tracks on both sides of the plastic base with a resolution of about 2.0 mrad. [56]. A Gaussian smearing like the one described for momenta was used to simulate the angular resolution.

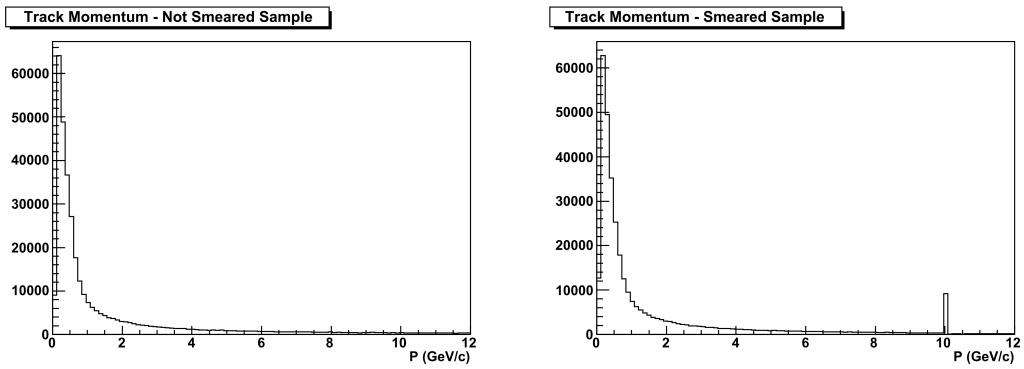

Figure 6.1: The momentum distribution of charged particles attached to primary vertex: comparison between the non-smeared (left) and smeared (right) sample.

6.2.2. The effect of undetected particles

Since emulsions detect ionising particles, neutral ones cannot be (directly) detected. In order to reproduce this constraint, neutral hadrons and photons were disregarded in the computation of physical quantities.

In Figure 6.2 it is shown how the multiplicity at primary vertex changes when these undetected particles are neglected. In the left part, the multiplicity computed with charged and neutral hadrons is displayed, whereas the distribution shown in the right part is obtained considering only charged hadrons. The shapes of the two distributions are very different: the latter is more peaked than the former and its mean value is about

5 whereas it is about 12 for the former. 54.9% of the total track sample is removed by this selection.

Particles with a track slope larger than 0.5 and protons with a kinematical energy less than 0.3 GeV/c are also neglected. The reconstruction efficiency for such particles is very low, and even when detected it is very difficult to compute their momentum with a precision suitable for kinematical analysis. This selection removes 37.5% of charged particles; the multiplicity distribution computed only with charged particles surviving to this cut is shown in Figure 6.3

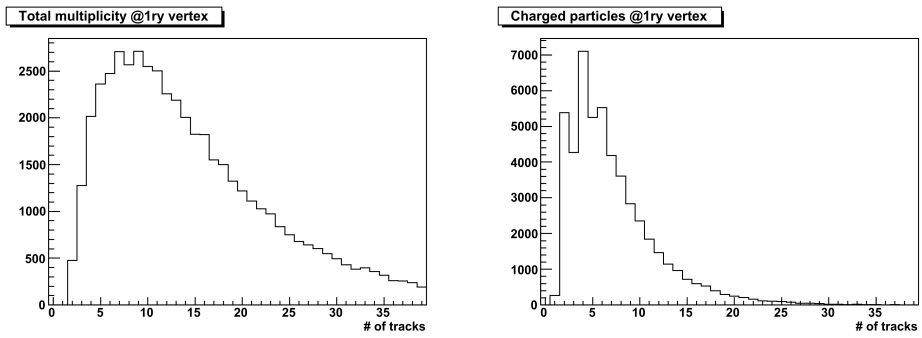

Figure 6.2: The multiplicity distributions of tracks at primary vertex computed by using all charged and neutral hadrons (left) and only charged particles (right).

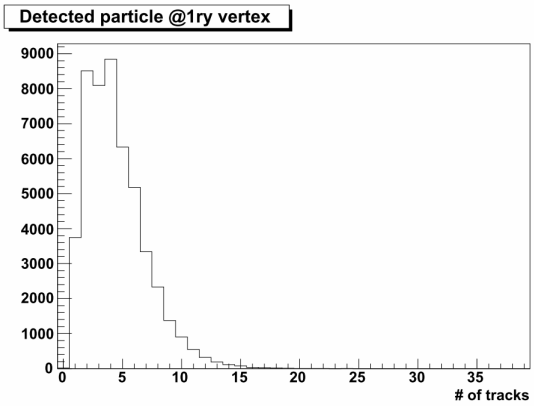

Figure 6.3: Multiplicity distribution at primary vertex computed only with detectable particles

6.2.3. Photon recovery

The contributions from photons can be "recovered" when some circumstances occur: pair production is the starting point of an electromagnetic shower that can be reconstructed in the emulsion sheets. If the shower is detected, an evaluation of its energy yields an estimation of the photon energy, actually "recovering" the photon for kinematical analysis.

Photons may convert far from the emission vertex; thus, even if the shower is reconstructed and the photon is identified, the vertex at which is had been produced is not obviously determined. The efficiency of "gamma attachment" depends on its energy, as shown in Figure 6.4 [90]. This curve was used in the MC sample to reject photons having a low attachment efficiency. This is displayed in Figure 6.5, which

shows a comparison of the photon energy and multiplicity distribution per event, before and after the rejection procedure. Without rejection, the mean photon energy is about 600 MeV and, on average, 4.5 photons per event are produced (within the brick), mostly in an even number; if the samples are restricted to non-rejected photons (*i.e.* the ones with an high attachment efficiency), the mean energy is about 2 GeV and just 1 photon per event is produced: only photons with a high energy survive this selection. This effect is due to the dependence of photon attachment efficiency on the energy: as shown in Figure 6.4, the efficiency increases with the shower energy.

A photon with a high attachment efficiency is a good candidate to be recovered, but just the one that converts one in the brick can be realistically considered in the analysis. Photon conversion in the ECC was simulated *ad-hoc* because this information is not included in MC files.

The conversion probability of a photon traversing a thickness L of matter is:

$$P = 1 - e^{L/\lambda} \qquad 6.1$$

where λ is the mean free path, set to 7/9 X_0. The average radiation length X_0 for an ECC-like material (emulsion + lead) is about 7 mm.

The ECC structure was simulated and the photon path in the brick computed. By using the conversion probability, non-converting photons were rejected. Finally, survivor photons are considered as detected particles and they are included in the computation of kinematical quantities. In Figure 6.6, the energy and multiplicity distribution of converting photons are reported. These are not very different from the ones obtained with the only requirement of high attachment efficiency. In fact almost all (98%) of photons correctly attached to primary vertex convert inside a brick.

In this analysis also the photon energy resolution was taken into account. It is given by formula [90]:

$$\frac{\sigma_E}{E} \approx \frac{50\%}{\sqrt{E}} \oplus 0.17 \qquad 6.2$$

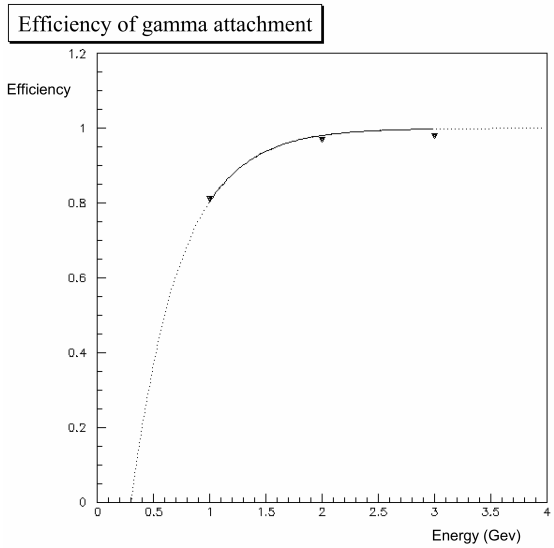

Figure 6.4: Efficiency of gamma attachment as a function of the energy

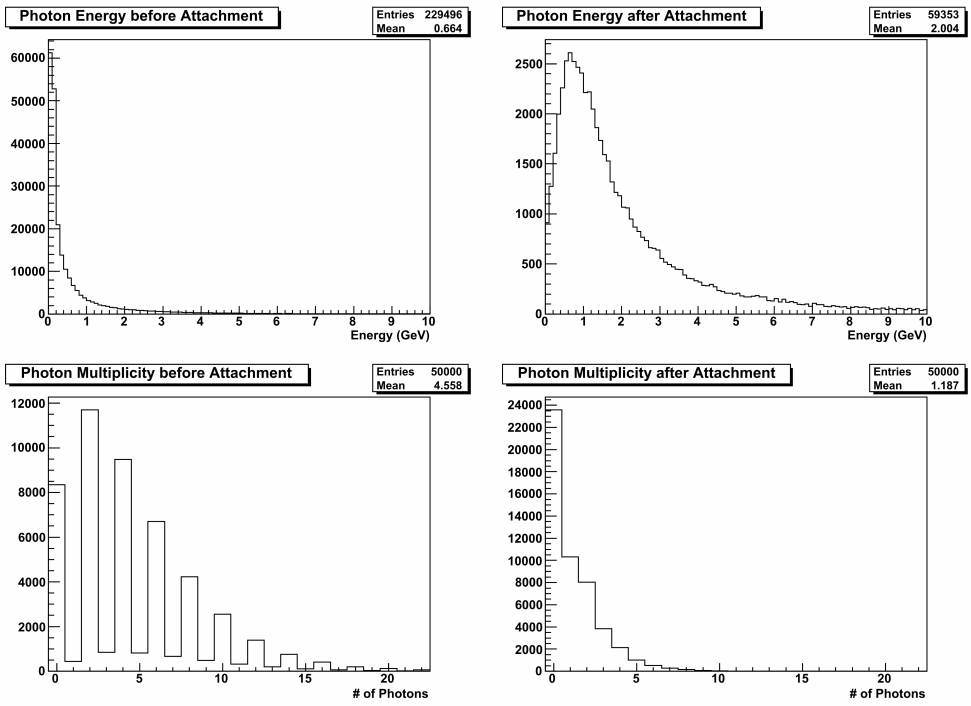

Figure 6.5: Energy distributions of photons obtained using all photons (top-left) and just photons with high efficiency of attachment (top-right). In the bottom side: multiplicity distribution at the primary vertex computed using all photons (left) and only photons with high attachment efficiency (right).

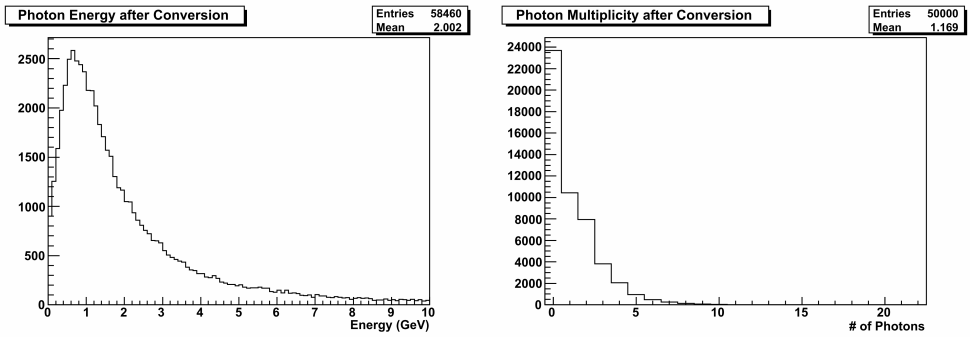

Figure 6.6: Energy (left) and multiplicity (right) distributions of converting photons in an ECC.

6.3. The missing transverse momentum

The analysis was performed by considering the kinematical variables described in section 6.1. The first one is the missing transverse momentum $P_{t,miss}$ defined as an imbalance in the total momentum at the primary vertex in neutrino transverse plane.

The main source of $P_{t,miss}$ is due to undetected neutrinos in the final state. In ν_μNC interactions, these are neutrinos produced in the primary interaction, whereas for ν_τCC events (signal), the tauonic neutrino produced at the decay vertex is an indirect source of $P_{t,miss}$: in the latter case, in fact, it is impossible to produce a precise estimation of the tau momentum (due to the small flight length, resulting in few micro-tracks), and the products of tau decay are included into the $P_{t,miss}$ computation.

Even for events without neutrinos in the final state, such as ν_μCC interactions, the $P_{t,miss}$ sizeably differs from zero because there are other sources:

- Nuclear re-interaction and Fermi motion
- Measurement errors
- Undetected particles (neutral particles or particles not detectable in the emulsion, like the ones with large angle or protons with low energy)

In order to understand the contributions to $P_{t,miss}$ given by each of these sources, the ν_μCC interactions from MC were used as a test sample. In the next sections, the results obtained from this study will be shown.

In addition, another scenario is proposed: the ν_μNC events and the ν_τCC events were treated as ν_μCC events, by considering the neutrino in the final state be detectable and measurable, to understand what fraction of $P_{t,miss}$ is not due to neutrinos. These two samples and the ν_μCC one are compared in the next section.

Finally, the $P_{t,miss}$ computed for the signal was compared to the one computed for the background. The results of this analysis have already been shown in section 6.3.2.

6.3.1. Results from ν_μCC sample

Before showing the results obtained from the analysis of the ν_μCC sample, it is useful to understand how $P_{t,miss}$ changes as a function of the number of particles detected at the primary vertex. In fact, an undetected particle is a source of $P_{t,miss}$.

Figure 6.7 is a schematic view of the particle momenta in the neutrino transverse plane for several scenarios. In this plane, the charged lepton and the hadronic system are in a back-to-back configuration. In the case in which all particles are detected and all momenta are measured without any errors, regardless of the type of interaction, $P_{t,miss}$ is non-zero. For ν_μCC events, there are no reasons for which the $P_{t,miss}$ vector should have a privileged direction, and it is randomly oriented. The sources of $P_{t,miss,}$ in this case, are the Fermi motion, and the nuclear re-interactions of hadrons produced in neutrino-neutron collisions.

When some particles of the hadronic system go undetected as, for example, the neutral ones, a contribution to $P_{t,miss}$ arises, opposite to the muon. This effect increases with the number of undetected particles and the maximum $P_{t,miss}$ is reached when also large angle particles and proton with low energy are neglected.

$P_{t,miss}$ was computed both for the non-smeared and smeared samples and the results are compared in Figure 6.8. The values obtained using the smeared samples are larger; then, also measurement errors can be considered as a $P_{t,miss}$ source. The contribution to $P_{t,miss}$ given by each source is reported for both samples in Figure 6.9[7].

Finally the procedure of "photon recovery" described in section 6.2.3 was applied and the $P_{t,miss}$ was computed considering firstly all photons with high attachment efficiency, and then selecting just the converting ones. The results are reported in Figure 6.10 and also the contribution to $P_{t,miss}$ from these sources is given in Figure 6.11. The latter scenario considered is the most realistic because the experimental resolutions and all "emulsion constraints" were taken into account.

The contributions to $P_{t,miss}$ not due to the neutrino in the final state was studied also for the ν_μNC and ν_τCC events, by treating them like CC events. The neutrino in the final state was considered like a muon for ν_μNC events. For the oscillation signal, the tau momentum was supposed measurable and it was used to compute the $P_{t,miss}$. In this way, the contribution given by the neutrino to the $P_{t,miss}$ is switched off and $P_{t,miss}$ is determined only by the hadronic systems. It is shown in Figure 6.12 that despite the small differences in the hadronic system, $P_{t,miss}$ in the three cases is very similar.

[7] The $P_{t,miss}$ distributions for this sample (as well as for the others presented in this chapter), are reported in Appendix A

EFFECT OF UNDETECTED PARTICLES ON $P_{t,miss}$ FOR ν_μCC SAMPLE

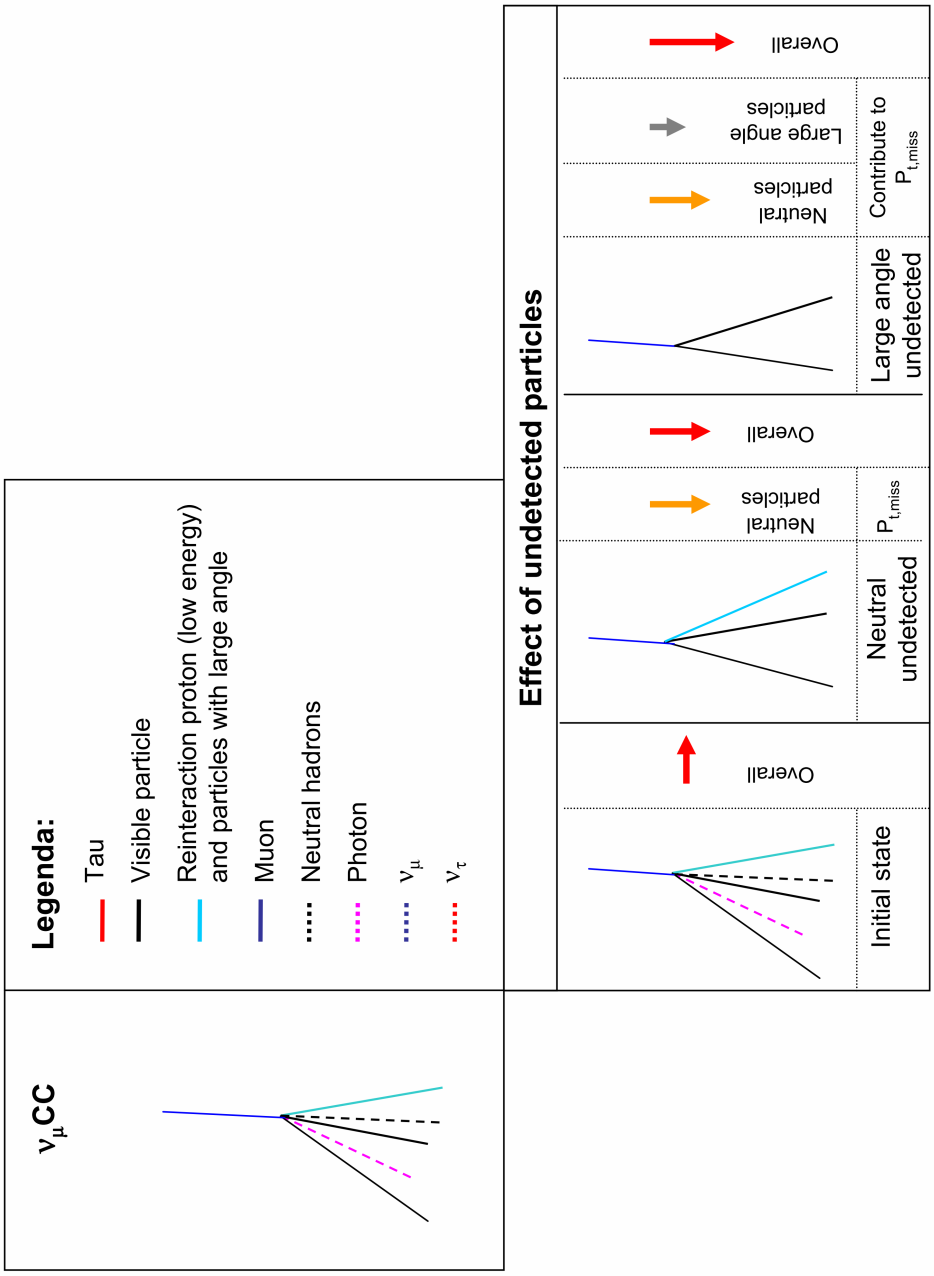

Figure 6.7: Effect of undetected particles on the value of the $P_{t,miss}$. Initially, it is randomly oriented; when particles of the hadronic system are excluded to perform its computation, its module increases because each missing particle creates a $P_{t,miss}$ oriented opposite to the muon.

RESULTS FROM ν_μCC SAMPLE

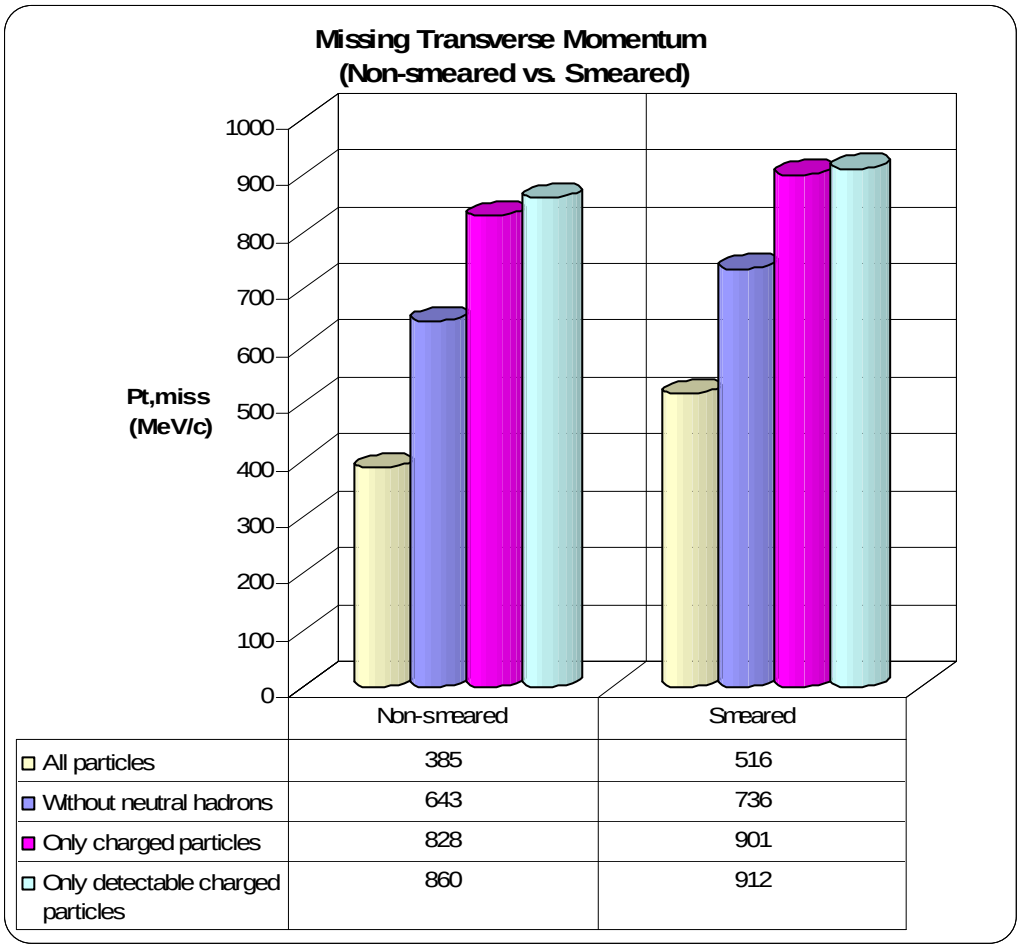

Figure 6.8: Results of $P_{t,miss}$ computed for the non-smeared and smeared samples by considering: a) all particles; b) charged particles and photons; c) just charged particles; d) detectable particles (i.e charged particles with angle less than 0.5 rad and protons with energy larger than 0.3 GeV/c)

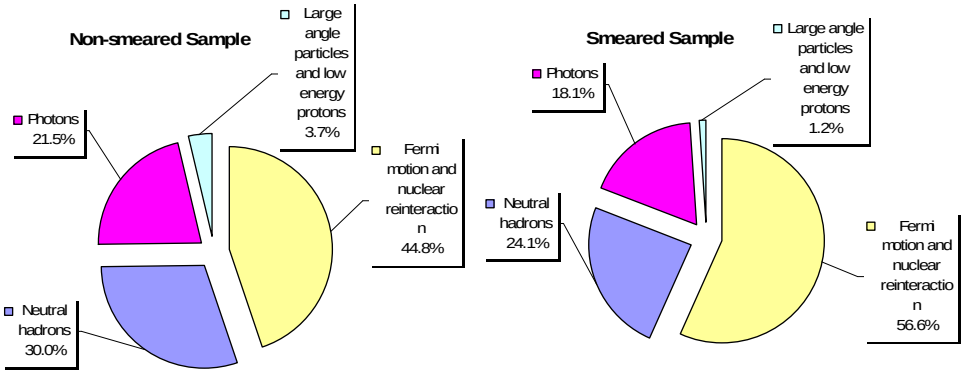

Figure 6.9: Contribution at $P_{t,miss}$ given, for non-smared and smeared samples, broken up by source: a) Fermi motion and nuclear re-interactions; b) Neutral hadrons, c) Photons; d)Particles with slope beyond 0.5 and protons with energy less than 0.3 GeV/c.

RESULTS FROM ν_μCC SAMPLE

(PHOTON RECOVERY)

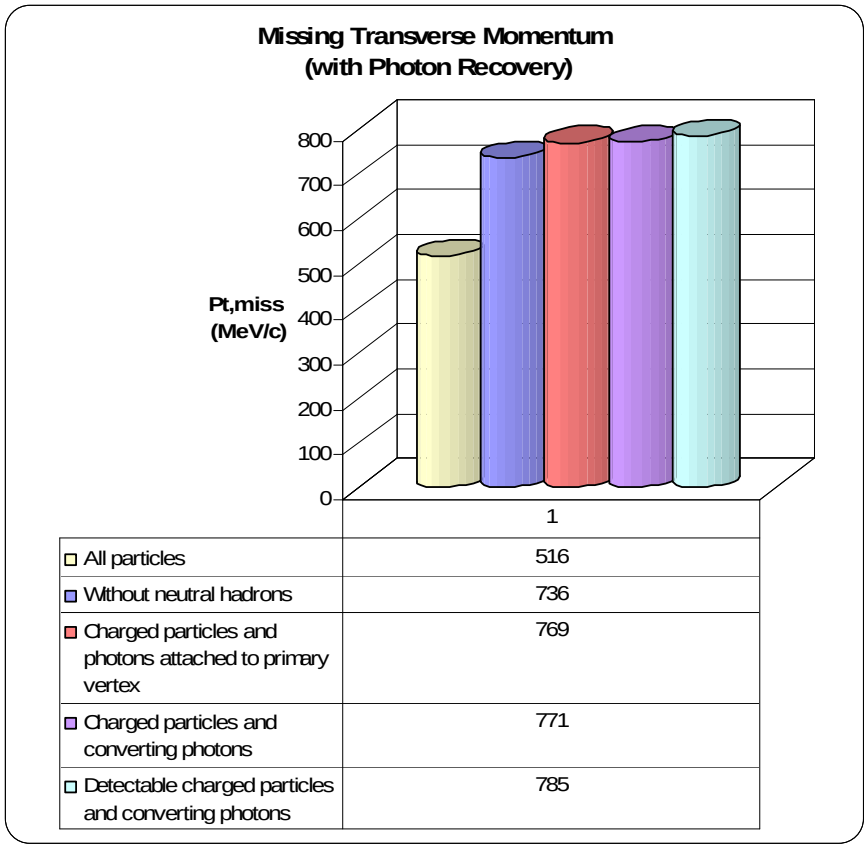

Figure 6.10: Results of $P_{t,miss}$ obtained for the smeared sample by applying the procedure of "photon recovery". The value has been computed including in the primary vertex, besides the charged particle, also: a) all photons (case "without neutral hadrons"); b) photons with high attachment efficiency; c) photons of case (b) converting in the brick

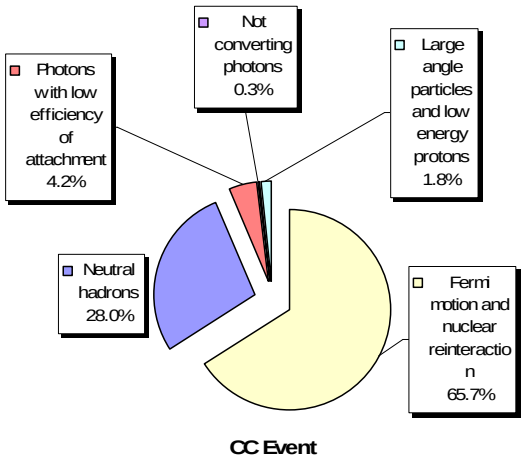

Figure 6.11: Contributions to $P_{t,miss}$ broken up by source: a) Fermi motion and nuclear re-interactions; b) neutral hadrons; c) Photons with low attachment efficiency; d) non-converting photons; e) Particles with a slope larger than 0.5 and protons with energy less than 0.3 GeV/c.

COMPARISON BETWEEN ν_μCC, ν_μNC AND ν_TCC SAMPLE

(NEUTRINO AND TAU AS MUON)

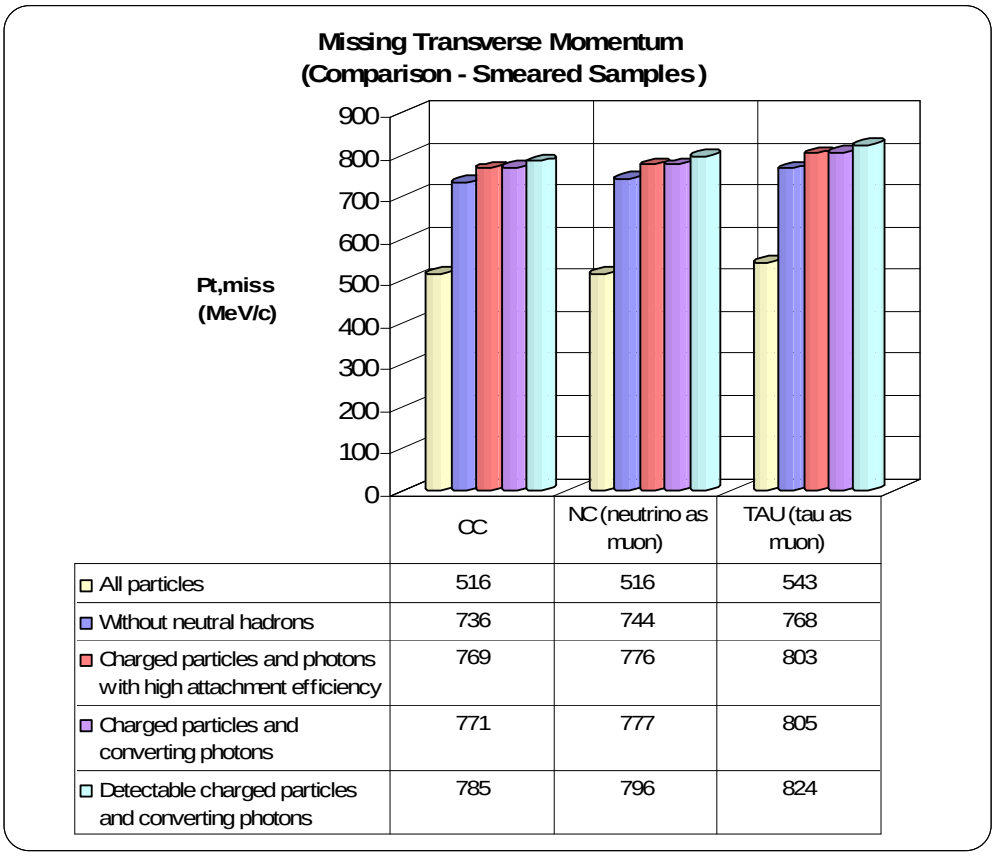

	CC	NC (neutrino as muon)	TAU (tau as muon)
All particles	516	516	543
Without neutral hadrons	736	744	768
Charged particles and photons with high attachment efficiency	769	776	803
Charged particles and converting photons	771	777	805
Detectable charged particles and converting photons	785	796	824

Figure 6.12: Results of $P_{t,miss}$ obtained for three smeared samples: CC is the ν_μCC sample, NC (neutrino as muon) is the background sample in which the momentum of neutrino has been considered measurable (then it is used in the computation of $P_{t,miss}$); TAU (tau as muon) is the signal sample (using the same spectrum as the one used for the ν_μCC and ν_μNC) in which the tau momentum is used to compute the $P_{t,miss}$.

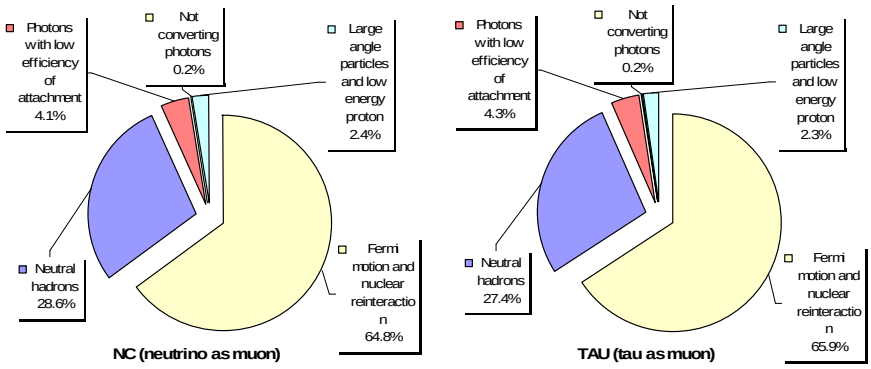

Figure 6.13: Contribution to $P_{t,miss}$ broken up by source: a) Fermi motion and nuclear re-interactions; b) neutral hadrons; c) Photons with low attachment efficiency; d) non-converting photons; e) Particles with slope beyond 0.5 and protons with energy less than 0.3 GeV/c.

6.3.2. Results from ν_μNC and ν_τCC samples

Figure 6.14 shows a schematic representation of the momentum vectors in the neutrino transverse plane for a generic ν_μNC and ν_τCC interaction. The hadronic system is back-to-back, respectively, to the neutrino in ν_μNC interactions and to the tauon, in ν_τCC interactions.

The undetected neutrino attached to the primary vertex is the $P_{t,miss}$ source for the background whereas for the signal the situation is different. Since it is difficult to estimate the tau momentum, the momentum of the daughter particle replaces it in the computations. By operating in this way, the neutrino produced at the decay vertex is not taken into account and it is a source of $P_{t,miss}$. Then, in both cases, the initial $P_{t,miss}$ is determined by the presence of the neutrino in the direction opposite to the hadronic system.

50,000 ν_τCC MC events were available but the analysis was performed just on the high multiplicity (HM) events in which at least another track besides the parent is fully measured. 84.5 % of MC interactions are HM events. Each event was weighted for its oscillation probability.

For the neutral current interactions another selection was performed. The files used for the analysis contain only neutrino interactions and no hadron reinteractions. A hadron re-interaction is a background for the tau-to-hadron channel only if the daughter track produced has a momentum greater than 2 GeV/c. Then the momentum of the parent track has to be at least 2 GeV/c. In first approximation, events with all hadrons below 2 GeV/c were disregarded (they cannot have a daughter with more than 2 GeV/c).

In Figure 6.15 the results obtained for the ν_μNC sample are reported. The smearing applied on charged particles generates a $P_{t,miss}$ back-to-back to the neutrino and so the $P_{t,miss}$ decreases. The same effect is given by the undetected particles: in fact the value of the $P_{t,miss}$ decreases as a function of the number of missed particles. Figure 6.16 shows the contribution to $P_{t,miss}$ given by each source.

Figure 6.17 shows the results from the ν_τCC sample. In this case the $P_{t,miss}$ due to the "measurement smearing" and the one due to the undetected particles are in competition. Smearing is applied to all charged particles including the daughter track that is directed back-to-back to the hadronic system. When smearing is applied a $P_{t,miss}$ in both directions arises: the contribution given by "measurement smearing" in the direction of the neutrino is larger than the one produced in the opposite direction. As a result, $P_{t,miss}$ increases when smearing is introduced. (Figure 6.19 - top).

Another contribute has to be taken into account: the one given by undetected particles. When particles are removed, a $P_{t,miss}$ arises back-to-back to the neutrino and this contribution is opposite to the one given by the "measurement smearing". The contribution of "measurement smearing" at $P_{t,miss}$ decreases with the number of particles undetected (see Figure 6.20). This effect is more remarkable in the case in which large angle particles and protons with low energy are ignored. The related contribution to $P_{t,miss}$ is larger than the one given by "measurement smearing" in the opposite direction so that $P_{t,miss}$ decreases when smearing is applied (Figure 6.19 - bottom).

The contribution to $P_{t,miss}$ given by each source is reported in Figure 6.18. If one compares these values to the ones obtained for ν_μNC events notes that the contribution to $P_{t,miss}$ given by particles with large angle and proton with low energy is different in the two cases and it is greater for the ν_τCC event. This result can be explained by considering the difference in the hadronic system for the two types of interaction: large angle particles are isotropically distributed for NC whereas they are mostly emitted back-to-back to the neutrino for the ν_τCC event.

The procedure of photon recovery was applied also for these two samples. For ν_τCC events, only photons of primary vertex were recovered. The result obtained recovering also photons attached to the secondary vertex will be shown in the section 6.6.

In Figure 6.21 the results from the ν_μNC and ν_τCC samples are compared. The values computed using just detectable particles are different for the two samples. Neutral current events feature a $P_{t,miss}$ larger than the one obtained for the tau sample, as expected.

The OPERA Proposal [56] suggests, in order to enrich the tau candidate sample, to select events with $P_{t,miss}$ below 1 GeV. The results obtained applying this cut are reported only for the most realistic case. In Figure 6.23 the $P_{t,miss}$ distribution is shown for the background (blue line) and the signal (black line). The efficiency of the cut is respectively 42.6% and 72.9%.

EFFECT OF UNDETECTED PARTICLES ON $P_{t,miss}$ FOR ν_μNC AND ν_τCC SAMPLES

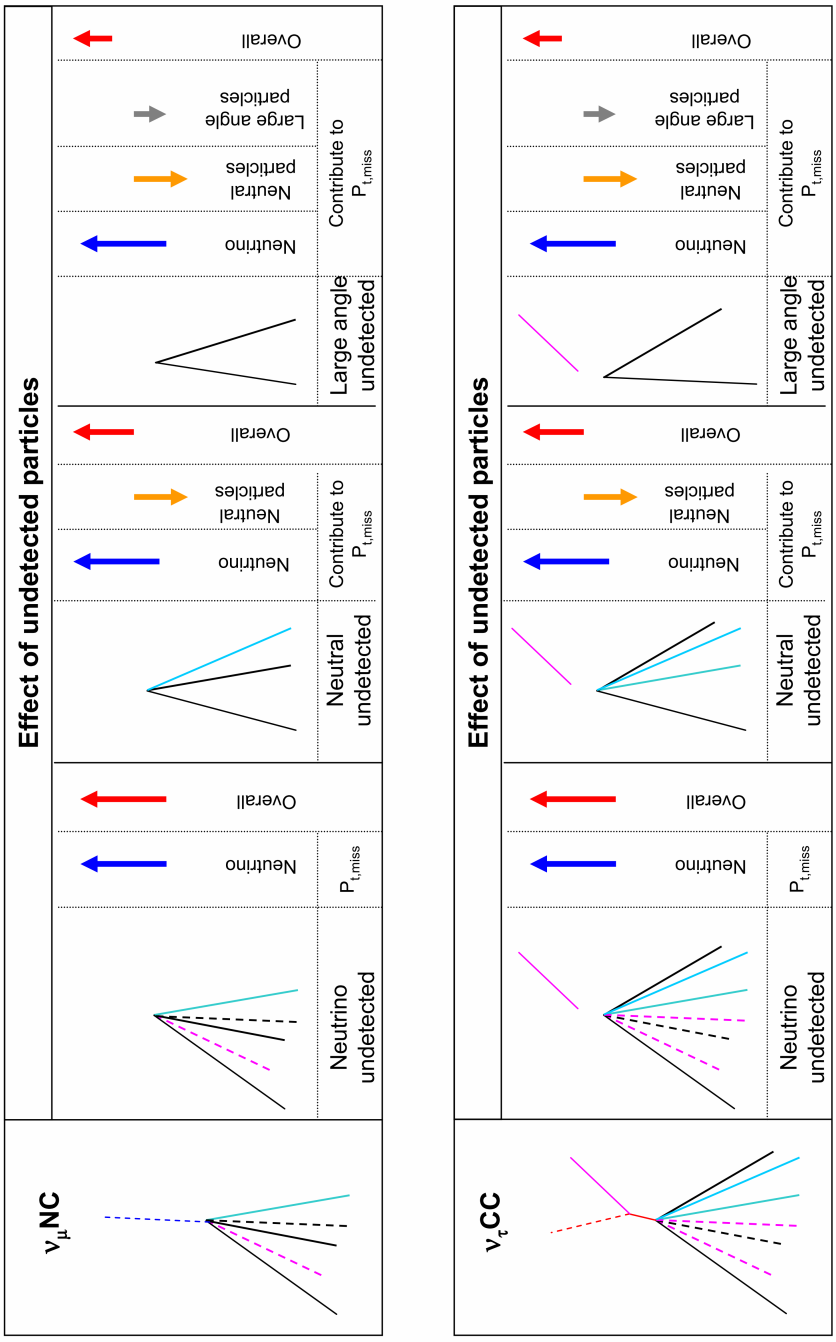

Figure 6.14: Effect of undetected particles on the value of $P_{t,miss}$ for background and signal. Initially, due to the presence of the undetected neutrino, a non-vanishing $P_{t,miss}$ oriented back-to-back to the hadronic system is present; missing particles of the hadronic system excluded give rise to $P_{t,miss}$ oriented back-to-back to the neutrino and the value of $P_{t,miss}$ decreases.

RESULTS FROM ν_μNC SAMPLE

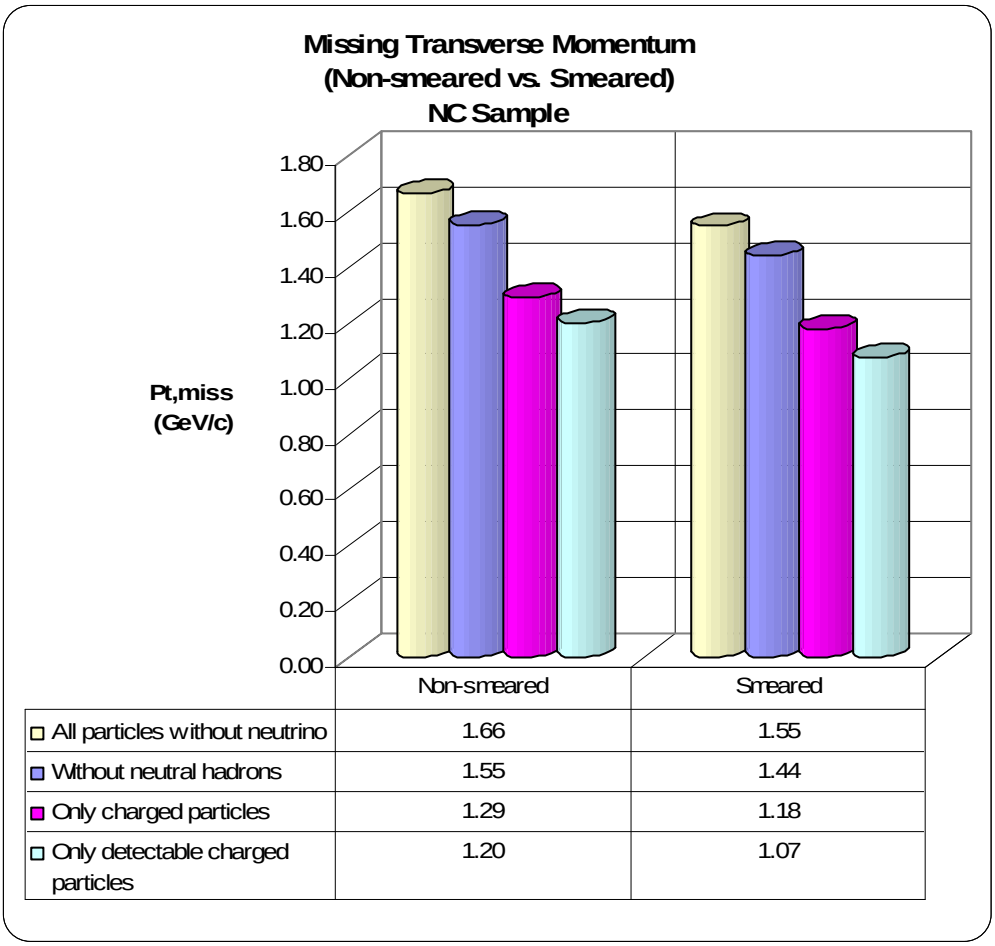

Figure 6.15: Results of $P_{t,miss}$ computed for the non-smeared and smeared samples by considering: a) all particles; b) charged particles and photons; c) just charged particles; d) charged detectable particles (i.e particles with slope below 0.5 and protons with energy larger than 0.3 GeV/c)

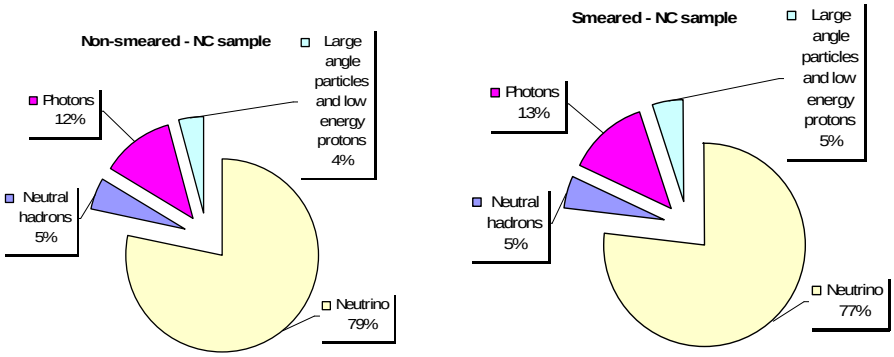

Figure 6.16: Contributions to $P_{t,miss}$, for the non-smeared and smeared samples, broken up by source: a) Fermi motion and nuclear reinteractions; b) Neutral hadrons, c) Photons; d) Particles with slope above 0.5 and protons with energy below 0.3 GeV/c.

RESULTS FROM ν_τ CC SAMPLE

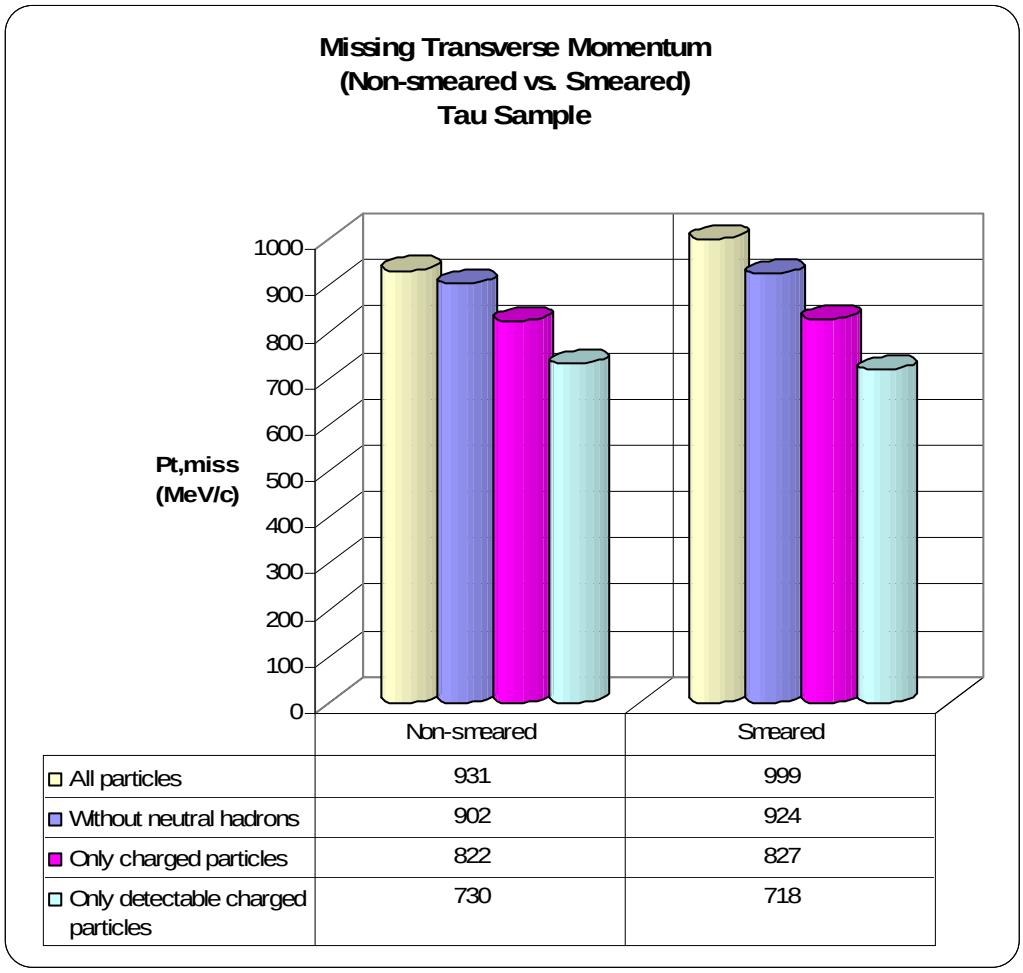

Figure 6.17: Results of $P_{t,miss}$ computed for the non-smeared and smeared samples by considering: a) all particles; b) charged particles and photons; c) just charged particles; d) charged detectable particles (i.e particles with slope below 0.5 and protons with energy above 0.3 GeV/c)

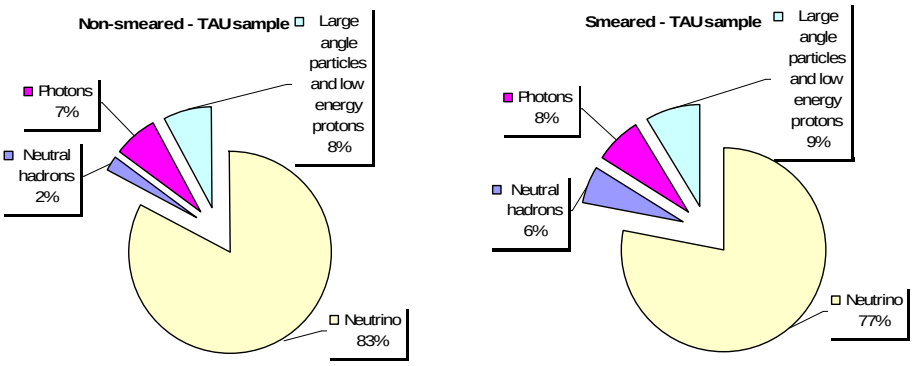

Figure 6.18: Contributions to $P_{t,miss}$, for the non-smeared and smeared samples, broken up by source: a) Fermi motion and nuclear re-interactions; b) Neutral hadrons; c) Photons; d) Particles with slope above 0.5 and protons with energy below 0.3 GeV/c

EFFECT OF SMEARING ON ν_τCC SAMPLE

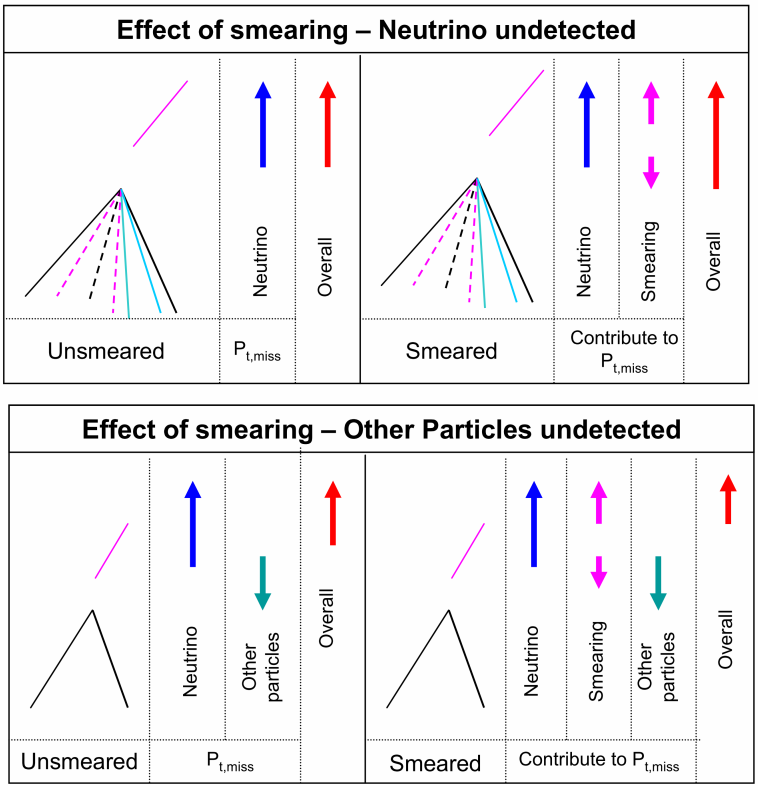

Figure 6.19: Effects of the "measurement smearing" in the case in which the only undetected particle is the neutrino (top) and in the case in which the neutrino and other particles go undetected (bottom)

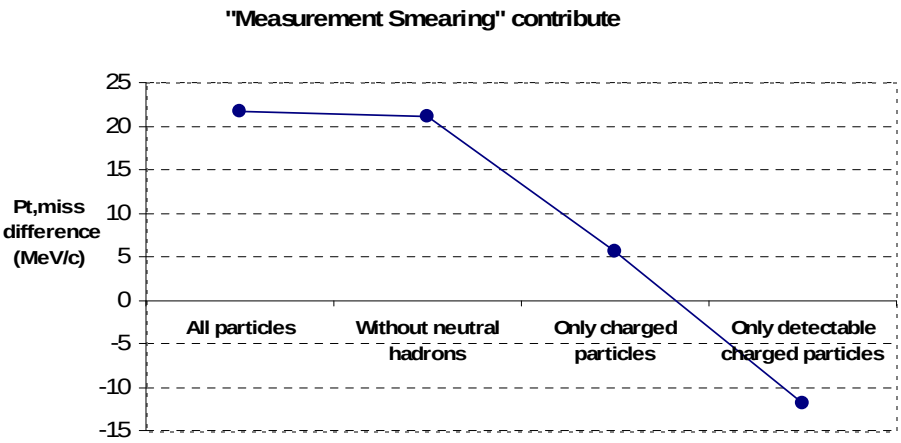

Figure 6.20: Contribution to $P_{t,miss}$ in the ν_τCC sample, given by the "measurement smearing", as a function of the number of particles removed.

COMPARISON BETWEEN ν_μNC AND ν_TCC SAMPLE

(PHOTONS RECOVERY)

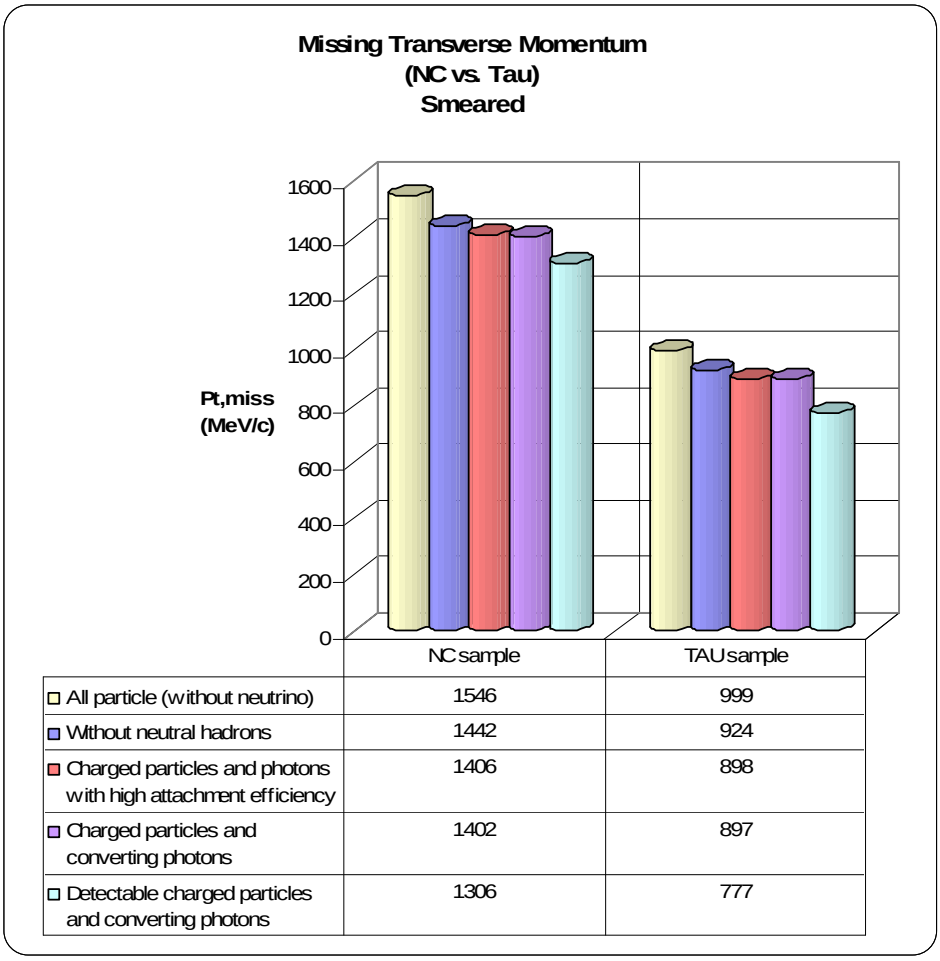

Figure 6.21: Comparison of $P_{t,miss}$ values between signal and background in several scenarios. Values were computed considering attached to primary vertex, besides the charged particle, also: a) all photons (case "without neutral hadrons"); b) photons with high attachment efficiency; c) photons of case(b) converting in the brick

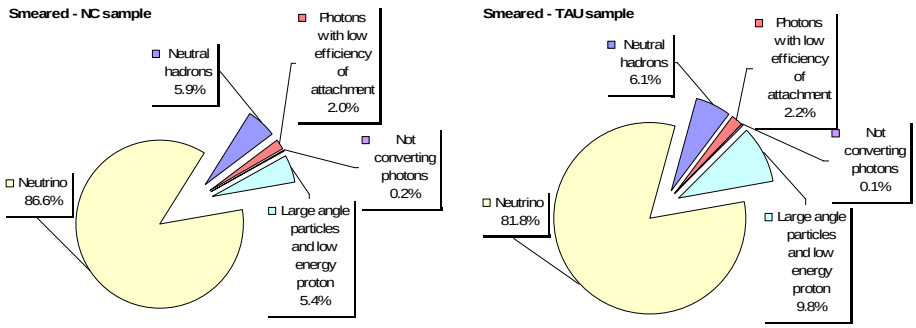

Figure 6.22: Contribution to $P_{t,miss}$ broken up by source: a) Fermi motion and nuclear re-interactions; b) neutral hadrons; c) Photons with low attachment efficiency; d) non-converting photons; e) Particles with slope above 0.5 and protons with energy below 0.3 GeV/c.

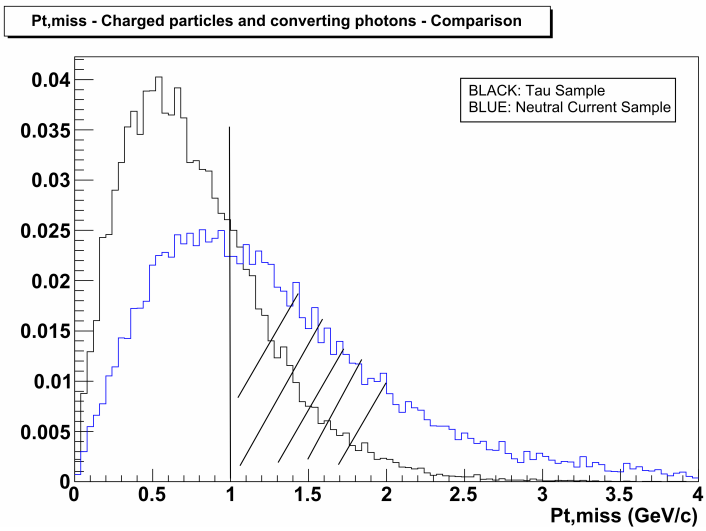

Figure 6.23: The $P_{t,miss}$ distribution obtained in the more realistic case for the signal (black line) and the background (blue line).

6.4. The φ angle

The second variable studied is the φ angle, *i.e.* the angle between the direction of the parent track and the total momentum of the hadron system in the neutrino transverse plane. In Figure 6.24 a schematic representation is shown of track vectors in the neutrino transverse plane and the φ angle for the ν_μNC and ν_τCC samples. As explained in section 6.1, the value of this angle is expected to be lower for background events because the parent track is one hadron of the hadronic system.

The φ angle was computed by using both the ν_μNC and ν_τCC interactions, degrading the MC information as described previously. In Figure 6.25 the distributions of the φ angle obtained by using the ν_μNC sample are reported, for four different scenarios, and the mean values are summarised in Table 6.1.

The number of detected particles affects the behaviour of the φ angle: when some particles (for example neutral hadrons) are neglected, the hadronic momentum vector changes its components in the neutrino transverse plane. In particular, the modified vector is closer to the neutrino vector and then the φ angle is larger than the one computed using the complete configuration. The larger the number of particles neglected, the stronger the effect. The photons recovery procedure also influences the value of this angles. A converting photon is considered as a particle of the hadronic system (they mostly come from π^0 decays) and included in the computation of the angle; since part of the momentum of the missing neutrals is recovered, the total effect is a decreasing of the φ angle.

The same analysis performed on the ν_τCC samples gives a different result: the φ angle depends always on the number of detected particles, but the dependence is reversed with respect to the one obtained for the background. In this case, the larger the number of particles neglected, the smaller the value of angle. This behaviour is consistent and expected: for a ν_τCC interaction, in fact, the parent track (the tauon) is back-to-back to

the hadronic system as well as the muonic neutrino is in a ν_μNC event. Since, as explained, the recomputed hadronic system is closer to the neutrino for an "ordinary" event, it will be likely closer to the parent track for a signal event.

Obviously the photon recovery procedure affects also in this case the value of the angle, but in a reversed way. In Figure 6.26. the distributions of the φ angle obtained by using the ν_τCC sample are reported for four different scenarios and the mean values are summarised in Table 6.2.

Finally, the results shown in Table 6.1 (background) and the ones reported in Table 6.2 (signal) are compared. As expected, the value computed using the ν_τCC events is larger than the one of the NC events. The OPERA Proposal sets a cut at $\pi/2$ rad to select the τ candidates. The efficiency obtained by using this cut is, for the more realistic case, 86.6 % for the signal and 34.9% for the background.

The efficiency $\epsilon_{pt,miss+\varphi}$ was evaluated by combining the efficiency computed for $P_{t,miss}$ and φ: the value obtained 14.8% for NC events and 63.1% for ν_τCC.

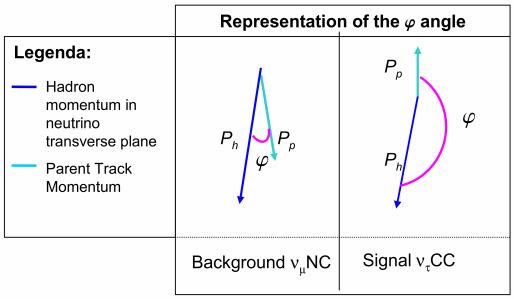

Figure 6.24: Schematic representation of the φ angle for the background and the signal.

ν_μNC RESULTS		
Detected particles	**φ (rad) Non-smeared**	**φ (rad) Smeared**
All particles (without neutrino)	1.23	1.25
Without neutral hadrons	1.27	1.28
Only charged particles	1.30	1.31
Only detectable charged particles	1.35	1.36
Detectable charged particles and converting photons in brick	-	1.26

Table 6.1: Values of the φ angle computed for the background using the non-smeared and smeared samples.

ν_τCC RESULTS		
Detected particles	**φ (rad) Non-smeared**	**φ (rad) Smeared**
All particles (without neutrino)	2.80	2.76
Without neutral hadrons	2.54	2.52
Only charged particles	2.39	2.36
Only detectable charged particles	2.32	2.32
Detectable charged particles and converting photons in brick	-	2.44

Table 6.2: Values of the φ angle computed for the signal using the non-smeared and smeared samples.

φ ANGLE DISTRIBUTION FOR ν_μNC AND ν_τCC SAMPLES

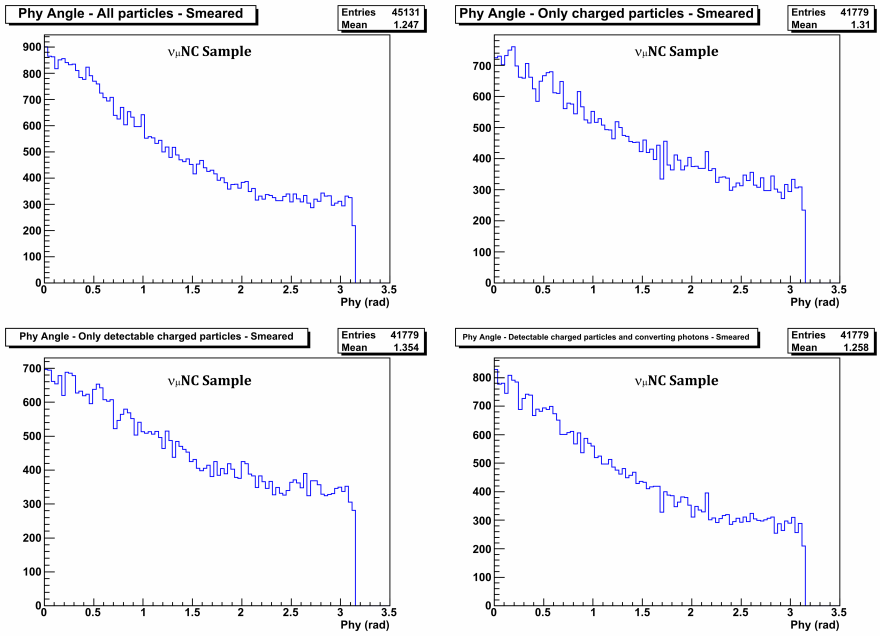

Figure 6.25: The φ angle distributions obtained for the background considering different scenarios: (top-left) all particles detected without the neutrino; (top-right) charged particles detected; (bottom-left) charged detectable particles detected; (bottom right) charged detectable particles and converting photons

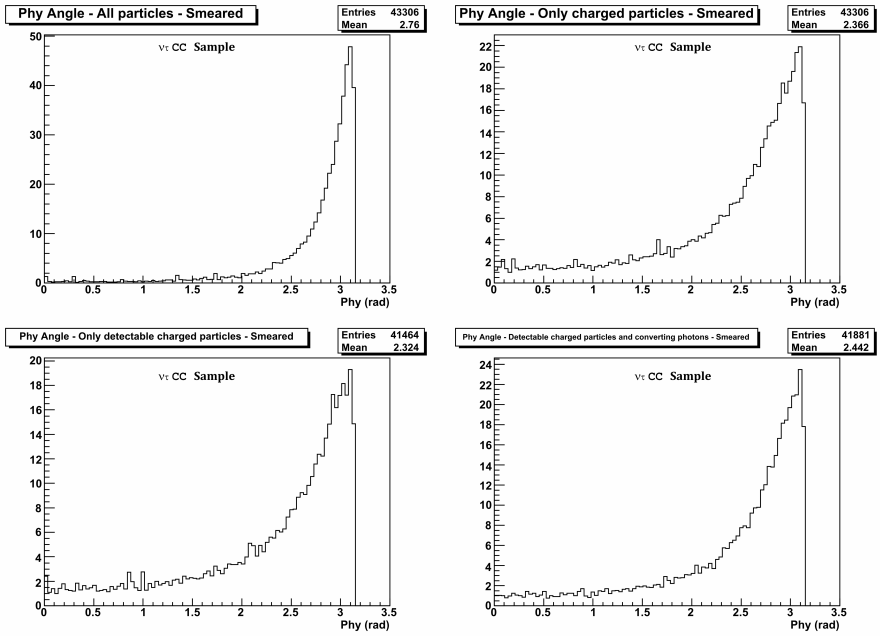

Figure 6.26: The φ angle distributions obtained for the signal considering different scenarios: (top-left) all particles detected without the neutrino; (top-right) charged particles detected; (bottom-left)charged detectable particles detected; (bottom right) charged detectable particles and converting photons

6.5. Beyond the standard analysis chain

In this section, the focus is on other variables not considered in the Proposal but that might be used to discriminate between the signal and the background: three angles, θ, α and γ and one transverse momentum Q_t. For these variables the efficiency cuts has not been yet studied.

6.5.1. The θ angle

It is useful to recall the kinematical configuration of vectors in the plane perpendicular to the incoming neutrino. In the transverse plane, the following vectors (see Figure 6.27) can be identified: P_h is the hadronic momentum, $P_{t,miss}$ is the missing transverse momentum and P_p is the parent track momentum (an hadron for the background event and a τ for the signal event). θ is the angle, in this plane, between the parent track and the $P_{t,miss}$ vector. Because these two vectors are back-to-back for the ν_μNC event and not for the ν_τCC, this angle is expected to be larger in the former case. A thorough analysis has been performed for this variable, considering all scenarios, because it is related to $P_{t,miss}$ and φ. The θ angle distributions computed by using the background sample and the signal sample, are respectively shown in Figure 6.29 and in Figure 6.30; the mean values are summarised in Table 6.3 and in Table 6.4

Both for the signal and the background, the same behaviour of this variable is observed with respect to the lack of hadronic particles: the θ angle increases its value if particles of the hadronic system are missed. This is easily understood by looking at the change in the configuration of vectors in the neutrino transverse plane as the sample is degraded by decreasing the number of particles. In Figure 6.28 the behaviours of background and signal events are compared. In both cases the black lines denote the original vector configuration (all particles detected), while the red ones stand for the configuration of vectors computed with degraded samples. For the background the $P_{t,miss}$ vector was computed by adding the total momentum of the hadronic system and the momentum of the parent track[8]. The magnitude is the same for both vectors whereas the direction is reversed.

For the background, missing hadronic particles implies a decrease of the magnitude of $P_{t,miss}$ and an increase of the φ angle. As consequence of this, also the θ angle increases (blue in the original configuration and cyan in the new configuration).

For the tau sample, the $P_{t,miss}$ was computed in a similar way; the only difference is that the momentum of the daughter track (P_{dgh}) vector was considered instead of the one of the parent track vector. The new configuration features an increased $P_{t,miss}$. The same happens for the φ angle. Also in this case the θ angle increases (blue in the original configuration and cyan in the new configuration).

For both samples, then, the increase of θ is related to the changes in $P_{t,miss}$ and φ angle.

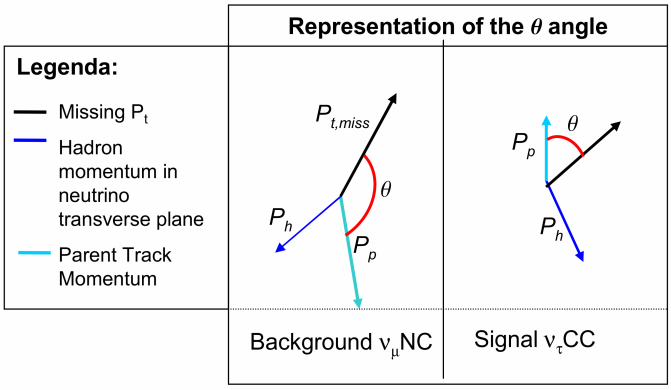

Figure 6.27: Schematic representation of the θ angle for background and signal events

[8] To compute $P_{t,miss}$ the momentum of daughter tracks should be used, but hadronic re-interactions are not present in the NC sample used to perform the analysis. Then, in first approximation, the momentum of the parent track has been used (see also section 6.6)

ν_μNC RESULTS		
Detected particles	**θ (rad) Non-smeared**	**θ (rad) Smeared**
All particles (without neutrino)	2.3	2.28
Without neutral hadrons	2.31	2.29
Only charged particles	2.33	2.31
Only detectable charged particles	2.41	2.40
Detectable charged particles and converting photons in brick	-	2.36

Table 6.3: Values of the θ angle computed for the background using the non-smeared and smeared samples

ν_τCC RESULTS		
Detected particles	**θ (rad) Non-smeared**	**θ (rad) Smeared**
All particles	0.700	0.704
Without neutral hadrons	0.965	0.968
Only charged particles	1.15	1.16
Only detectable charged particles	1.30	1.29
Detectable charged particles and converting photons in brick	-	1.15

Table 6.4: Values of the θ angle computed for the signal using the non-smeared and smeared samples

BEHAVIOUR OF THE θ ANGLE

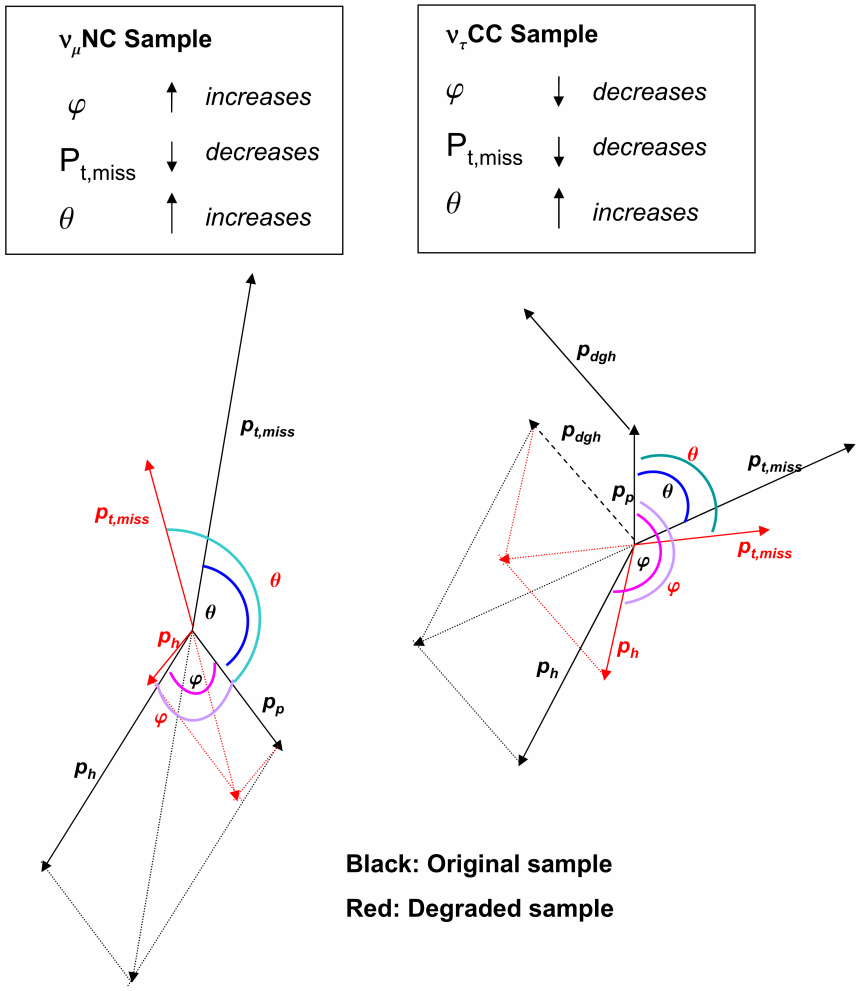

Figure 6.28: Schematic representation in neutrino transverse plane of the behaviour of the P_{tmiss}, φ and θ angles. Black vectors: all particles detected. Red vectors: some particles are missed.

θ ANGLE DISTRIBUTION FOR ν_μ NC AND ν_τ CC SAMPLES

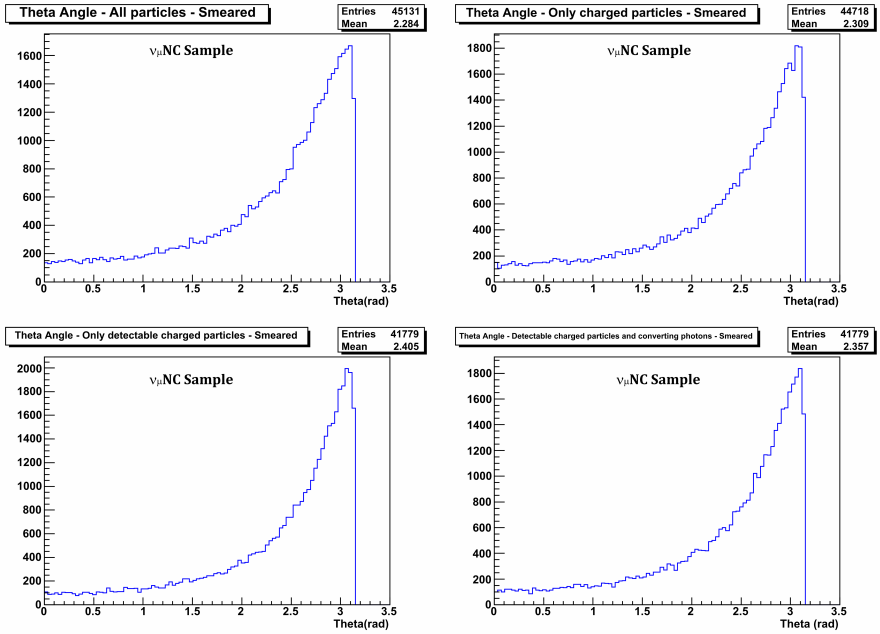

Figure 6.29: The θ angle distributions obtained for the background considering several scenarios: (top-left) all particles detected without the neutrino; (top-right) charged particles detected; (bottom-left) charged detectable particles detected; (bottom right) charged detectable particles and converting photons

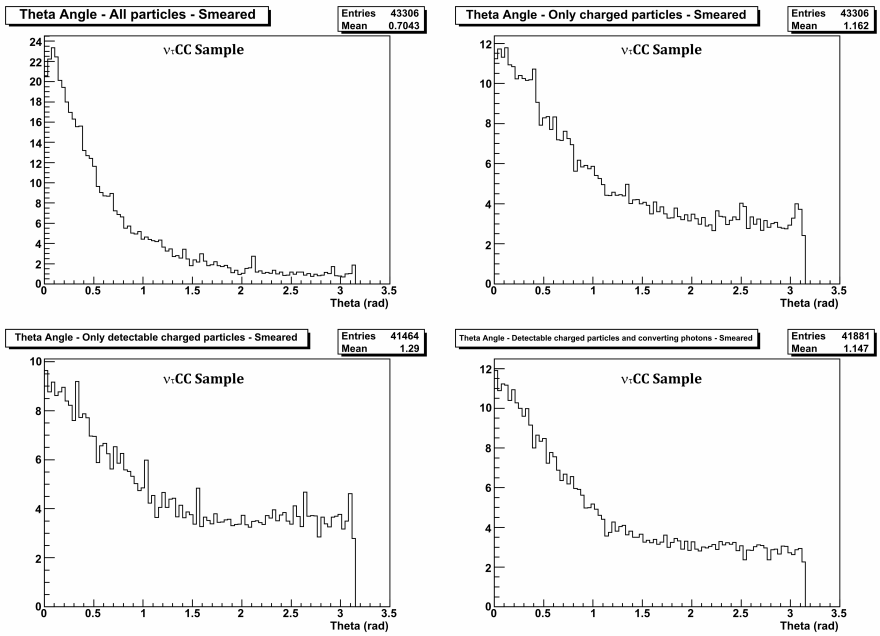

Figure 6.30: The θ angle distributions obtained for the signal considering different scenarios: (top-left) all particles detected without the neutrino; (top-right) charged particles detected; (bottom-left) charged detectable particles detected; (bottom right) charged detectable particles and converting photons

6.5.2. The Q_t variable

The Q_t is an isolation variable defined as the component of the momentum of the visible decay product perpendicular to the total visible momentum vector (Figure 6.31)

$$Q_T = \sqrt{(\vec{p}_h)^2 - (\vec{p}_h \cdot \vec{p}_{tot})^2 / p_{tot}^2} \qquad 6.3$$

This quantity is expected smaller for background events because the hadron produced at the interaction vertex is emitted in the hadronic jet. On the contrary, the hadron produced at the tau decay vertex is isolated with respect to the hadronic system, therefore the value of Q_t is expected to be larger.

The analysis was performed considering just the most realistic scenario in which, in addition to detectable charged particles, also converting photons are taken into account. The Q_t distributions for the samples of simulated ν_μNC events and ν_τCC events are reported in Figure 6.32. As expected, the average value obtained for the signal (953 MeV) is greater than the one obtained for background (633 MeV).

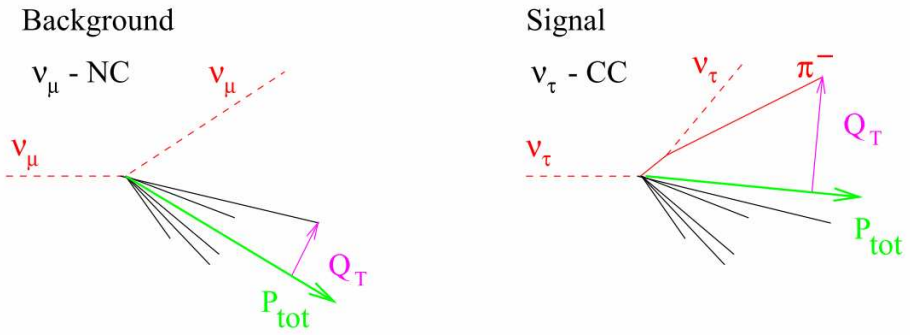

Figure 6.31: Schematic representation of the Q_t variable for the background and the signal

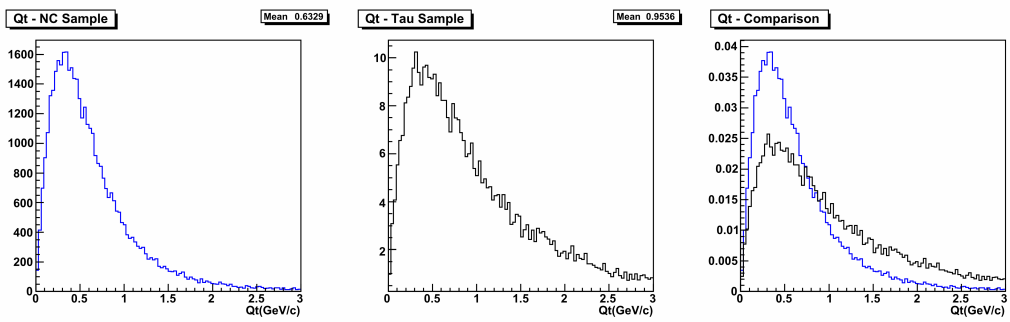

Figure 6.32: Distributions of the Q_t variable for the background (left), the signal (center) and both superimposed (background- blue line and signal – black line)

6.5.3. The α and γ angles

Two more angles might be used to discriminate signal and background; they are denoted as α and γ. The former is the angle between the parent track and the closest particle in the neutrino transverse plane. The latter is the angle between the decaying particle and the particle with the highest transverse momentum (with respect to the parent track) in the neutrino transverse plane.

For both angles signal events are expected to yield larger values than background events do. This is due, as already explained, to the configuration of involved vectors in the neutrino transverse plane *i.e.* to the different orientation of the parent track with respect to the hadronic system - see Figure 6.33.

The events on which the analysis was performed were the ones having, in addition to parent track, at least one detectable charged particle at the primary vertex. Converting photons are not taken into account. The α angle distributions for the signal and the background are shown in Figure 6.34. The ones for the γ angle are reported in Figure 6.35. In both cases the signal distribution has a peak for large value of the angles with a mean value respectively of 1.88 rad for the α angle and 2.28 rad for the γ angle. On the contrary the background distributions are peaked at zero with a mean value, respectively, of 1.41 rad and 1.34 rad.

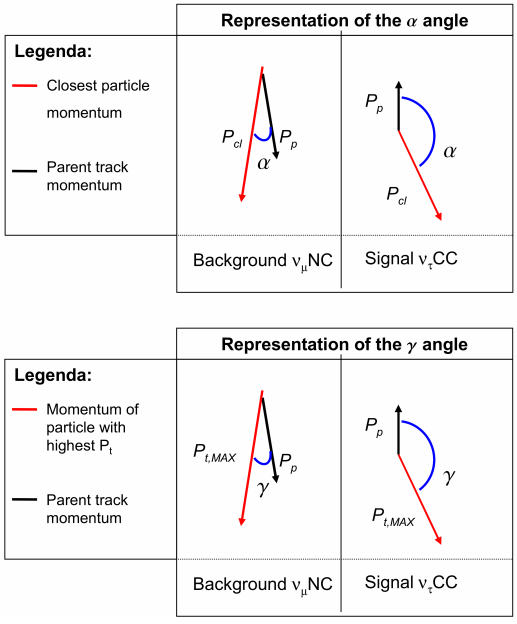

Figure 6.33: Schematic representation of the α angle (top) and γ angle (bottom) for the background and the signal

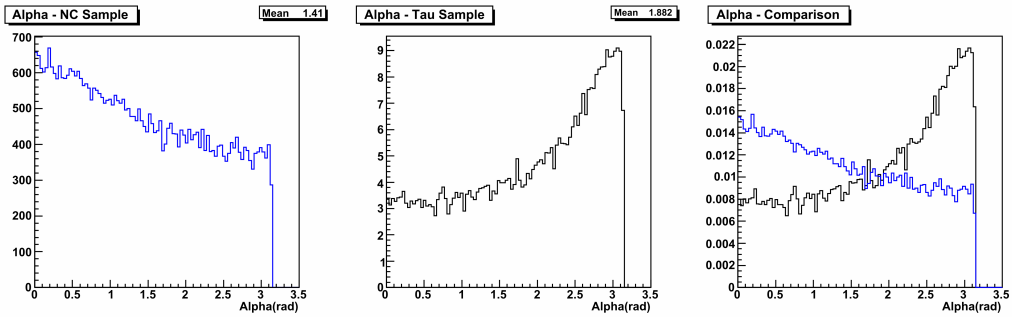

Figure 6.34: Distributions of the α angle for the background (left), the signal (center) and both superimposed (background = blue line and signal = black line)

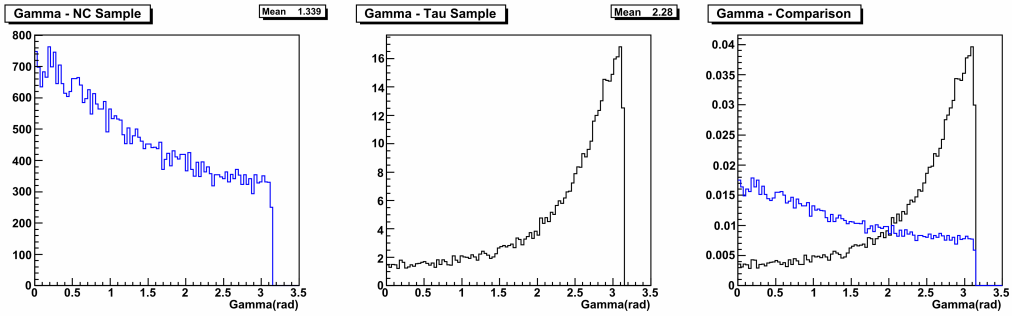

Figure 6.35: Distributions of the γ angle for the background (left), the signal (center) and both superimposed (background = blue line and signal = black line)

6.6. Hadron re-interactions study

The results presented in the previous sections are obtained by using an approximation in the estimation of the background. As explained, the hadron re-interactions were not present in the MC files used for this analysis. The effect of the secondary interactions on the kinematics was partially accounted for, by just considering events with hadrons with momenta greater than 2 GeV/s taken as possible parent tracks (the cut in the OPERA Proposal [56] on the momentum of the daughter is $P_{dgh} > 2$ Gev/c). Then the kinematics of the secondary interactions is partially inserted in the global kinematics. The background was re-evaluated using a state-of-the-art FLUKA code [82], as was described in the previous chapter. In this section, the details of the hadronic re-interaction computed with high statistics FLUKA solution are fully integrated in the global event kinematics of the neutrino events from the standard simulation in order to obtain a complete picture.

6.6.1. Integration of FLUKA simulation in the standard MC files

The results from FLUKA simulation[9] were integrated in the standard MC files by following these steps:

- From the ν_μNC MC samples only events having a momentum greater than 2 GeV/c were selected (as parent track)
- The daughter momentum and the transverse momentum were generated by considering the distribution of probability obtained in the FLUKA analysis (see chapter 5 for more details). In this way the momentum and the kink angle for the daughter particle were known.
- The two values obtained in the previous step were not enough to determine uniquely the direction of the daughter particle. Since the daughter particles are emitted randomly, a second angle was randomly generated to define the azimuth.
- The kinematical quantities were computed by using the daughter particle generated in this way.
- Each event was weighted taking into account the probability distribution obtained with the FLUKA simulation; this weight depends on the momentum of incoming particles, the momentum of the daughter and $P_{t,dgh}$

6.6.2. Comparison of the results

The information from the FLUKA simulation allows to plug the kinematics of the secondary interactions in the global kinematics of neutrino events. In this way, the interesting kinematical quantities can be re-computed using the information on the daughter particle and compared to the previous one.

The sample named "partial kinematics" is the one built by using only the parent track information. The one named "full kinematics" is the one in which the information on the daughter track was used to compute the kinematical variables. In this section these two samples are compared to each other and also to the signal sample. In addition two different values of the angular acceptance are considered: slope below 0.5 or 1.0.

6.6.2.a. Comparison between partial and full kinematics

Not all kinematical variables were influenced by the presence of the daughter track. In fact, the φ, the α and the γ angle do not change because they depend only on the hadronic system and on the direction of parent track. The variables for which an approximation was used are $P_{t,miss}$, the θ angle and Q_t.

For the $P_{t,miss}$ variable, the value computed in the partial kinematics is expected to be overestimated. In fact, in the full kinematics the momentum of the daughter tracks is

[9] More details about the FLUKA simulation are reported in chapter 5.

used to compute the $P_{t,miss.}$ This circumstance reflects the real case in which the momentum of the parent track cannot be estimated. In this case, then, another source of $P_{t,miss}$ is present, opposite to the neutrino direction and the total effect is a decrease of the $P_{t,miss}$. In the partial kinematics, because the momentum of the parent track is used to compute the $P_{t,miss}$, this source is not taken into account (see Figure 6.36).

The distribution of this variable for the two samples is shown in Figure 6.37. The mean value obtained is almost the same (for the full kinematics is 1.282 GeV/c with respect to the value of partial kinematics that is 1.306 GeV/c). The same result is obtained by setting the slope acceptance to 1.0. In this case the distributions are reported in Figure 6.38 and the mean values are, respectively, 1.348 GeV/c for the partial and 1.334 GeV/c for the full kinematics. Despite the expectations, it seems that for the $P_{t,miss}$ variable the approximation to use the momentum of the parent track instead of the one of the daughter is good.

Another variable analysed was the θ angle (the angle, in neutrino transverse plane, between $P_{t,miss}$ and the parent direction). One would expect a decrease for this variable when the daughter track is used to compute $P_{t,miss}$, due to the new source of $P_{t,miss}$ arising opposite to the neutrino. The $P_{t,miss}$ vector, computed considering also this contribute, is closer to the parent track than the $P_{t,miss}$ vector computed using the "partial kinematics" configuration. This behaviour is sizable as shown by the distributions of the theta angle reported in Figure 6.39 for the two samples. The partial kinematics sample is characterized by a distribution peaked at higher angles (blue line). Obviously also the mean values are different (2.36 rad for the partial and 2.17 rad for the full kinematics). The same result was obtained setting the slope acceptance to 1.0, with mean value of 2.34 rad and 2.16 rad (see Figure 6.40).

The third variable considered for this comparison is Q_t (the component of the momentum of the daughter track perpendicular to the total momentum). The use of the daughter track instead of the parent track implies an increase of Q_t because the angle between the daughter track and the hadronic jet is larger than the one between the parent track (that is in the hadronic system) and the hadronic jet.

The results for this variable are shown in Figure 6.41 in which the Q_t for full kinematics is peaked at 0.719 GeV/c whereas partial kinematics peaks at 0.633 GeV/c. The same behaviour is obtained setting the slope acceptance at 1.0; the mean values are respectively 0.754 GeV/c and 0.666 GeV/c (see Figure 6.42).

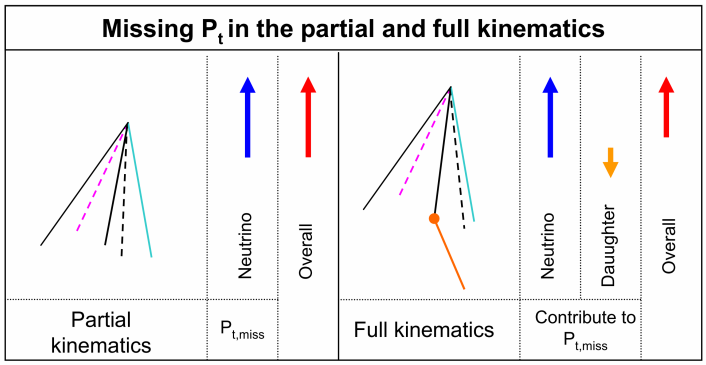

Figure 6.36: Effect of the use of the daughter in the computation of the $P_{t,miss}$ for the background sample.

MISSING PT DISTRIBUTIONS

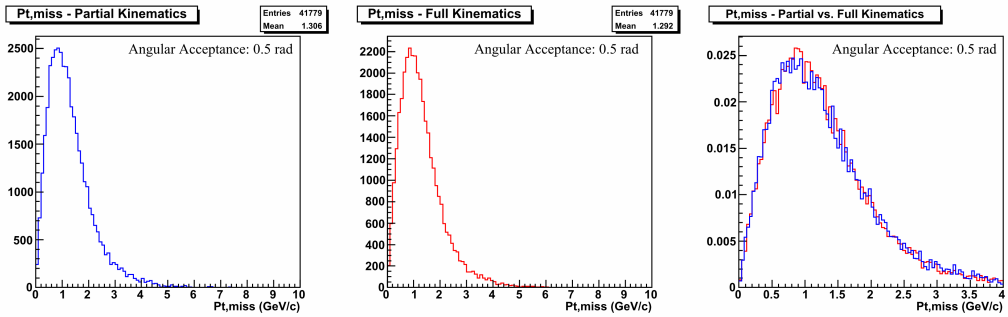

Figure 6.37: The $P_{t,miss}$ distributions for the background for the partial (left) and, full (center) kinematics. In the right the two distributions are superimposed (partial = blue, full = red). The slope acceptance is 0.5.

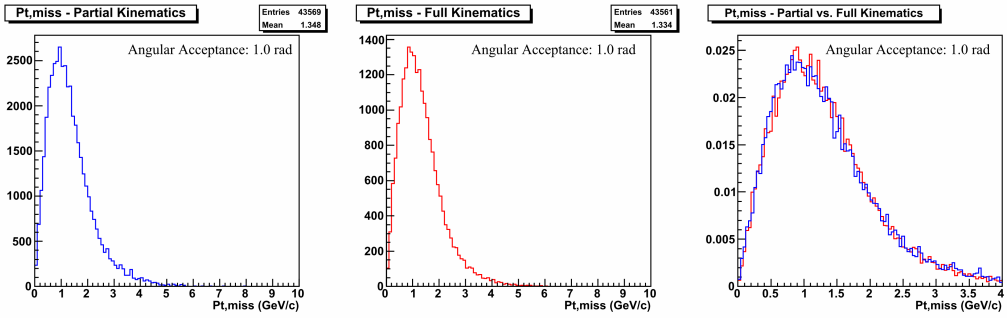

Figure 6.38: $P_{t,miss}$ distribution for the background for the partial (left) and full (center) kinematics. In the right the two distribution are superimposed (partial = blue, full = red). The angular acceptance is 1.0.

THE θ ANGLE DISTRIBUTIONS

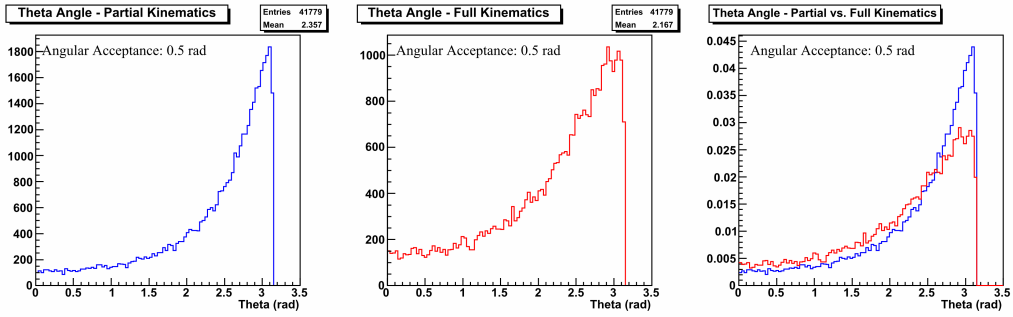

Figure 6.39: The θ angle distribution for the background for the partial (left) and full (center) kinematics. In the right the two distributions are superimposed (partial = blue, full = red). The slope acceptance is 0.5.

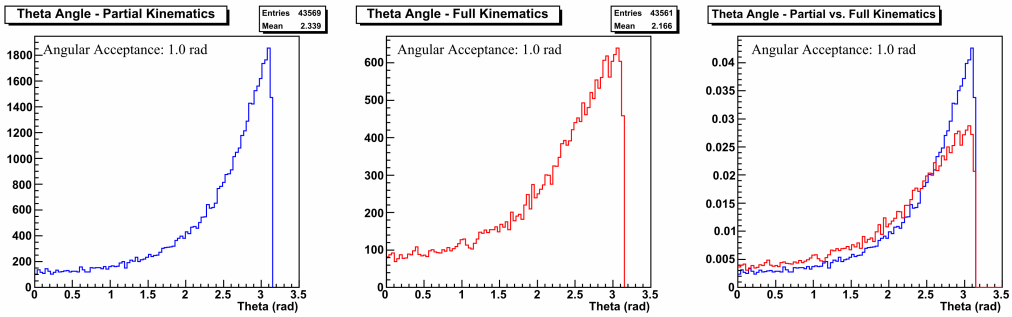

Figure 6.40: The θ angle distribution for the background for the partial (left) and full (center) kinematics. In the right the two distributions are superimposed (partial = blue, full = red). The slope acceptance is 1.0.

THE Q_t DISTRIBUTIONS

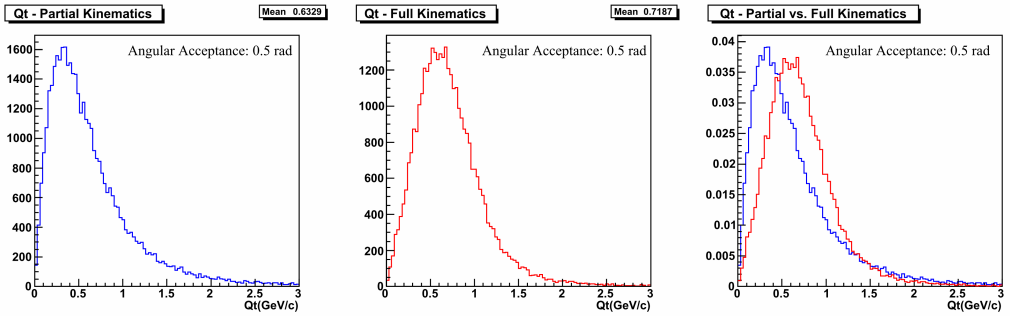

Figure 6.41: The Q_t distributions for the background for the partial (left) and full (center) kinematics. In the right the two distributions are superimposed (partial = blue, full = red). The slope acceptance is 0.5.

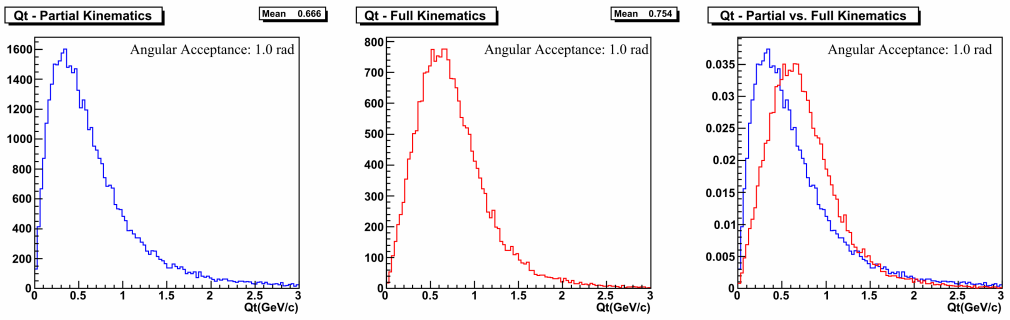

Figure 6.42: The Q_t distributions for the background for the partial (left) and full (center) kinematics. In the right the two distributions are superimposed (partial = blue, full = red). The slope acceptance is 1.0.

6.6.2.b. Comparison between the partial/full kinematics and the tau sample

The kinematical quantities computed in this new way were also compared to the ones of the signal. The $P_{t,miss}$ for the tau sample was computed taking into account also the photons attached to the decay vertex, and converting in the event brick. This is a requirement needed to perform an equal-footing comparison between the signal and the background. In fact the FLUKA simulations used to compute the probability to have an hadron interactions includes the possibly converting photons produced at secondary vertex. Figure 6.43 shows the results obtained for $P_{t,miss}$, setting the slope acceptance, respectively, to 0.5 and 1.0. In both cases, the distribution for the signal is reported in the left side; in the center and in the right side the partial and the full kinematics distributions are superimposed to the signal one. The efficiencies are recomputed and summarised in Table 6.5 (red values) where also the previous ones are reported.

The results for the other two variables are reported in Figure 6.44 for the θ angle and in Figure 6.45 for Q_t.

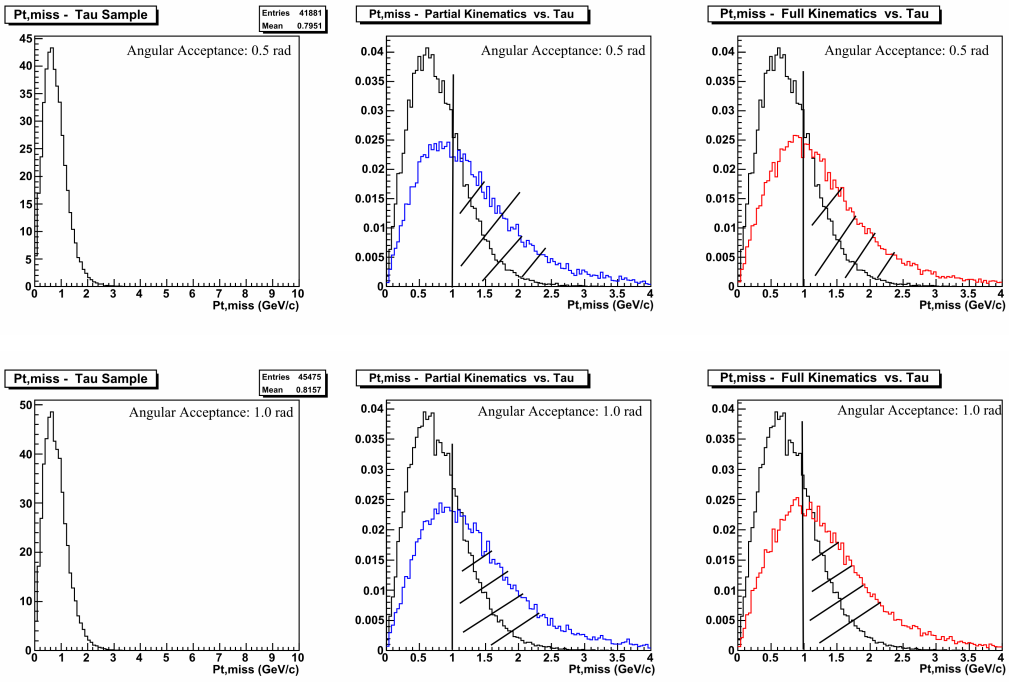

Figure 6.43: The $P_{t,miss}$ distribution for the signal (left = black line) computed considering also converting photons from the decay vertex. This distribution has been superimposed to the one of the background for the partial kinematics (center – tau = black line and background = blue line) and for the full kinematics (right – tau = black line and background = red line). The dashed area marks the excluded region corresponding to the "a priori" tau selection cuts. The slope acceptance is 0.5 for the top plots and 1.0 for the bottom ones.

Efficiencies for the $P_{t,miss}$ cut		
Slope Acceptance	**0.5**	**1.0**
Background (Partial Kinematics)	42.6 %	40 %
Background (Full Kinematics)	42.2 %	39.4 %
Signal (without photons at the decay vertex)	72.9 %	71 %
Signal (with photons at the decay vertex)	72.3 %	70.5 %

Table 6.5: Efficiency computed for the signal and the background – partial and full kinematics – by applying the Proposal cut for the $P_{t,miss}$ variable. The red values are the re-computed ones whereas the black ones are shown in section 6.3.2.

THE θ ANGLE DISTRIBUTIONS

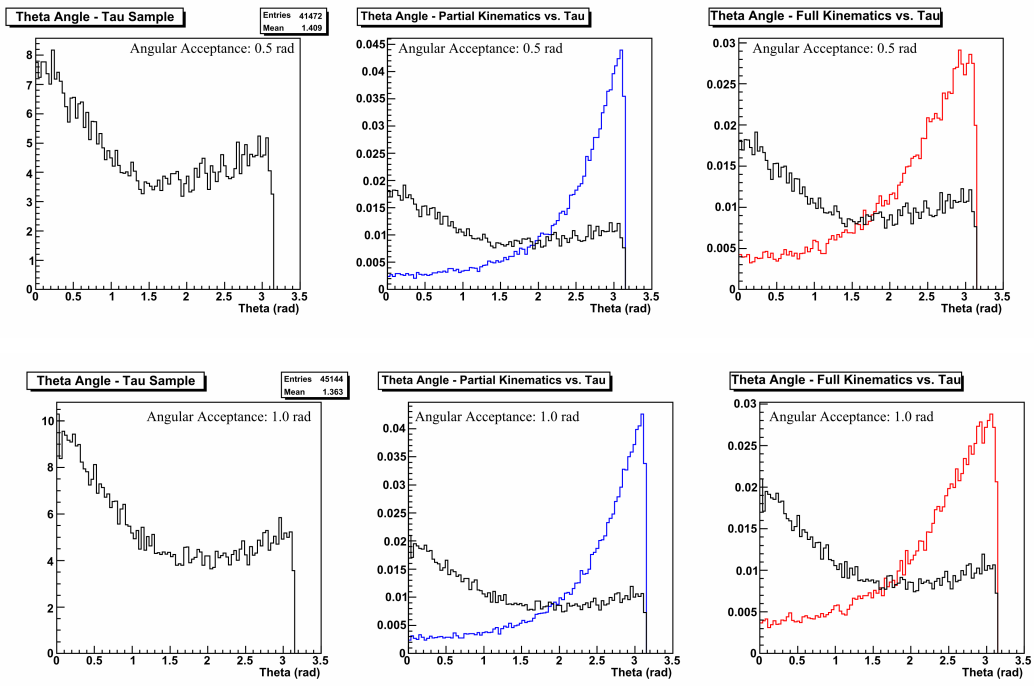

Figure 6.44: The θ angle distribution for the signal (left = black line) computed considering also at the decay vertex the converting photons. This distribution has been superimposed to the one of the background for the partial kinematics (center – tau = black line and background = blue line) and for the full kinematics (right – tau = black line and background = red line). The slope acceptance is 0.5 for the top plots and 1.0 for the bottom ones.

THE Q_t DISTRIBUTIONS

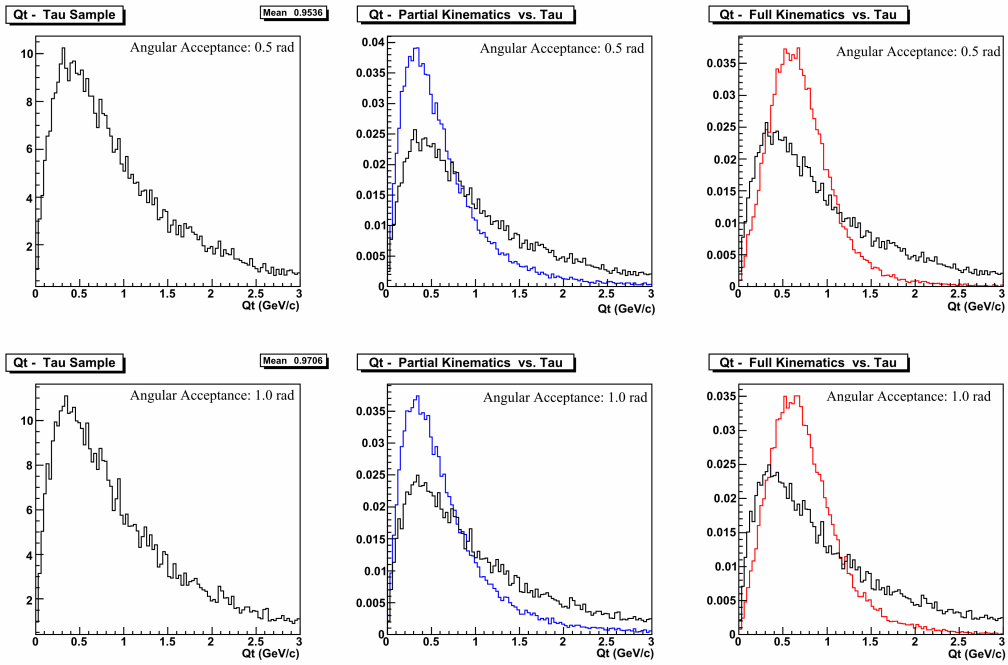

Figure 6.45: In the left the Q_t distribution for the signal is reported. This distribution has been superimposed to the one for the background for the partial kinematics (center – tau = black line and background = blue line) and for the full kinematics (right – tau = black line and background = red line). The slope acceptance is 0.5 for the top plots and 1.0 for the bottom ones.

Chapter 7

Observation of a first ν_τ candidate in OPERA

The topology and the kinematics of the first ν_τ charged-current candidate event satisfying the OPERA Proposal selection criteria are analysed in this chapter. The most likely interpretation is that the tau produced in the primary neutrino interaction decays to a single hadron.

7.1. Event topology

The decay search procedure (see chapter 3) applied to the 2008-2009 data sample yielded one candidate event fulfilling the selection criteria defined "a priori" for the ν_τ interaction search. The data sample amounts to 1088 events out of which 901 are classified as CC interactions. Taking into account the event location efficiencies, this corresponds to 1813 interactions occurring in the target, namely about 35% of the 2008 and 2009 data sample, or, referring to the integrated beam intensity, 1.89×10^{19} p.o.t..

In the next section some details about the topology of the event will be reported. It was independently measured with the European and Japanese scanning systems. Measurements are consistent and their averages are considered in the following. [84]

7.1.1. Event Tracks

The muonless neutrino interaction reported in detail here occurred in a brick situated in the wall 11 of the first supermodule and well inside the target: 3 bricks from the top and 24 bricks from the left. This allows a comprehensive study of the event: tracks could be

followed over large distances and secondary vertices including electromagnetic showers could be searched for in large volumes.

The primary neutrino interaction consists of 7 tracks, one of which exhibits a visible kink. Two electromagnetic showers originating from γ-rays that are associated with the event were reconstructed. Figure 7.1 shows a display of the event.

- Track 1 exits the primary interaction brick and is not found in the brick immediately downstream. It is left by a particle with momentum $0.78^{+0.13}_{-0.10}$ GeV/c, most likely interacting in the target tracker between both walls;
- Track 2 is left by a heavily ionizing particle. From its residual range 32 ± 0.5 g cm^{-2} and the value of $p\beta = (0.32^{+0.32}_{-0.11})$ GeV/c measured on the upstream half of the track, the particle is identified as a proton. The kaon hypothesis was rejected with a C.L. of 97%. The proton momentum resulting from the residual range is 0.60 ± 0.05 GeV/c.
- Track 3 is left by a particle which generates a two-prong interaction 4 bricks downstream of the primary vertex. Its momentum is $1.97^{+0.33}_{-0.25}$ GeV/c.
- Track 5 has been followed in wall 12 and disappears in wall 13 after a total distance shorter than 174 g cm^{-2}. The particle has a momentum of $1.30^{+0.22}_{-0.16}$ GeV/c.
- Track 7 is not directly attached to primary vertex and points to it with an IP = 43^{+45}_{-43} μm. Its starting point is separated from this vertex by two lead plates. Its origin is likely to be a prompt neutral particle. In the analysis, the momentum $0.49^{+0.29}_{-0.13}$ GeV/c has been added to the total momentum at the primary vertex.
- Track 4 exhibits a kink topology and it has been identified as a τ lepton. The expected γ factor from the kink angle is approximately 25. It is the parent track of a secondary interaction or decay.
- Track 8, the kink daughter track, is left by a particle of a high momentum of 12^{+6}_{-3} GeV/c which generates a 2-prong interactions 7 walls downstream its emission vertex. Its IP with respect to the primary vertex is 55 ± 4 μm. All the tracks directly attached to primary vertex match the vertex point within 7 μm.

Also two electromagnetic showers are reconstructed in the emulsion:

- γ-ray 1 has an energy of 5.6 ± 1.0 (*stat.*) ± 1.7 (*syst.*) GeV. The distance between its conversion point and the secondary vertex is 2.2 mm and the shower points to the vertex with a probability of 32%, the impact parameter being 7.5 ± 4.3 μm. Its probability to be attached to primary vertex is less than 10^{-3}, the IP being 45.0 ± 7.7 μm.
- γ-ray 2 has an energy of 1.2 ± 0.4 (*stat.*) ± 0.4 (*syst.*) GeV/c. It is compatible with either vertex, with a significantly larger probability of 82% at secondary vertex, the IP being 22^{+25}_{-22} μm compared to 10% and 85 ± 38 μm at primary vertex. Its distance to both vertces is about 13 mm.

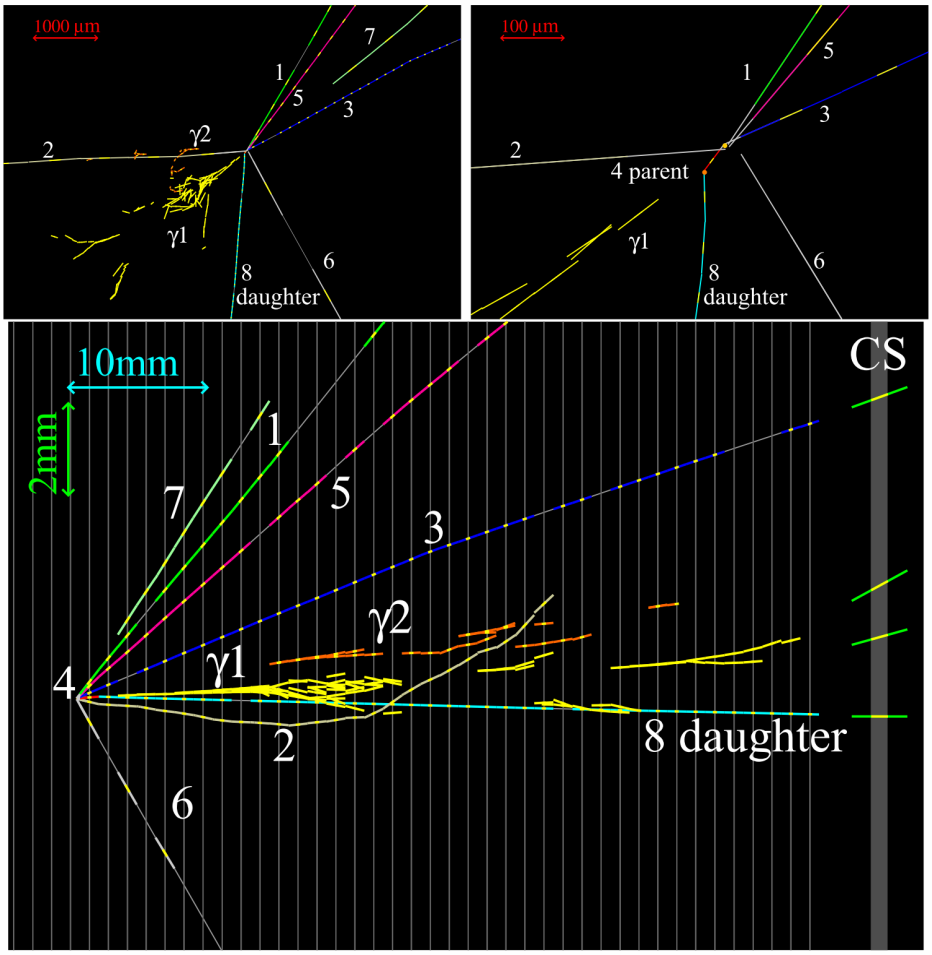

Figure 7.1: Display of the τ candidate event. Top left: side view. Top right: same view zoomed on the vertices. Bottom: longitudinal view [84]

7.2. Kinematical analysis of the candidate event

The kinematical analysis of this event was performed computing all interesting physical quantities and by comparing them to the MC simulations. The decay vertex variables studied were the kink angle, the path length of the τ, the momentum of the decay daughter and the total transverse momentum P_t of the detected daughter particles of the τ decays with respect to the parent track. The primary vertex quantities studied were the $P_{t,miss}$ and the φ angle (see chapter 6 for more details).

The MC samples used for the comparison are the ones described in chapter 6. Both for the signal and the background, the distributions obtained using the more realistic scenario were used. For the background, the sample is the one integrated with the FLUKA simulation, in which the daughter particle produced in a hadron re-interaction was taken into account.

7.2.1. The decay kinematics

In Table 7.1 the value of the decay kinematical quantities computed for this event are reported with the selection criteria used. All variables considered pass the selection cuts required to select a tau candidate.

These values were compared to the MC distribution of the signal. The MC data sample includes all high multiplicity events, with the additional requirement that the τ decay is classified as *long* (see chapter 2). In Figure 7.2 the MC distribution (black line), the variable value (red dark line) and the 68.3% domain of values allowed for the event (red bands) are reported.

The P_t value was computed by considering the most probable configuration in which both γ's point to the secondary vertex. The MC distribution was obtained performing the same consideration: all converting γ's attached to the decay vertex were included in the computation of this variable. In the low probability hypothesis where γ-ray 2 is attached to primary vertex, the systematic shift in P_t does not exceed 50 MeV/c. This small effect is included in Figure 7.2 (bottom left).

For the daughter particle, the smearing on the momentum is not applied. The cut-off (fixed to 10 GeV/c) set on the maximum momentum estimation by the multiple Coulomb scattering was removed. In fact for particles with a momentum greater than 10 GeV/c the measurement is based on the position deviations, with a resolution that is different from the one used in the simulation (which was tuned for the angular method). The comparison to the background distribution was not performed. This was due to the constraint on the simulated files on which the analysis was performed (for the background the maximum value of the daughter momentum is set to 10 GeV).

Decay kinematics value		
Variable	**Value**	**Selection criteria**
Kink Angle (mrad)	41 ± 2	> 20
Decay Length (μm)	1335 ± 35	within 2 lead plates
Momentum of daughter (GeV/c)	12^{+6}_{-3}	>2
Transverse momentum of the detected daughter particles (MeV/c)	470^{+230}_{-120}	>300 (γ attached)

Table 7.1: Values of the decay kinematical quantities computed for the τ candidate event with the respective selection criterion

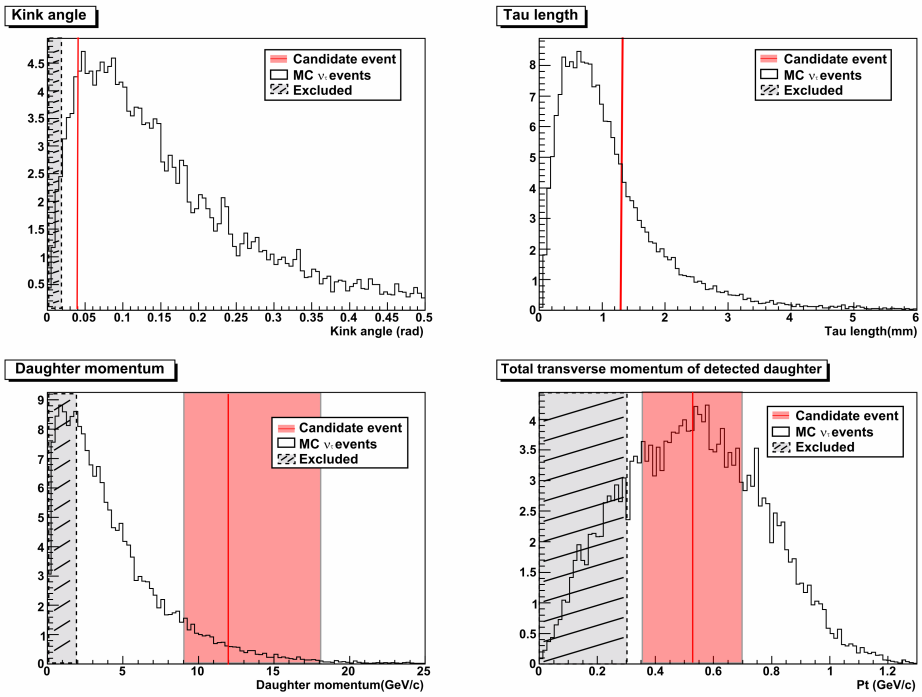

Figure 7.2: Monte-Carlo distribution of the kink angle for τ decays (top left); path length of the τ (top right); momentum of the decay daughter (bottom left); total transverse momentum P_t of the detected daughter particles of the τ decays with respect to the parent track (bottom right). The red band shows the 68.3% domain of values allowed for the candidate event and the dark red line the most probable value. The grey shaded area represents the excluded region corresponding to the "a priori" tau selection cuts.

7.2.2. The global kinematics

For the candidate event a standard kinematical analysis was performed, computing the discriminating quantities $P_{t,miss}$ and φ angle. The values obtained are compared to the MC distributions for both variables. Also in this case, for the signal, only *long decays* were selected and the converting photons at secondary vertex were taken into account. The comparison to the background distributions was performed.

The missing transverse momentum $P_{t,miss}$ at primary vertex is $0.57^{+0.32}_{-0.17}$ GeV/c. this is lower than the upper selection cut at 1 GeV/c (see Figure 7.3 - left). The φ angle between the parent track and the rest of the hadronic shower in the transverse plane is equal to 3.01 ± 0.03 rad, largely above the lower selection cut set at π/2 (see Figure 7.3 - right).

In addition, for this event, the value of the other 4 variables presented in the chapter 6 and not included in the standard analysis chain were estimated: the θ, α and γ angles and Q_t. The computed values are reported, together with the signal and background distributions (see Figure 7.4 and Table 7.2). No physical cuts were studied for this variables and no investigation on the correlation among them was performed.

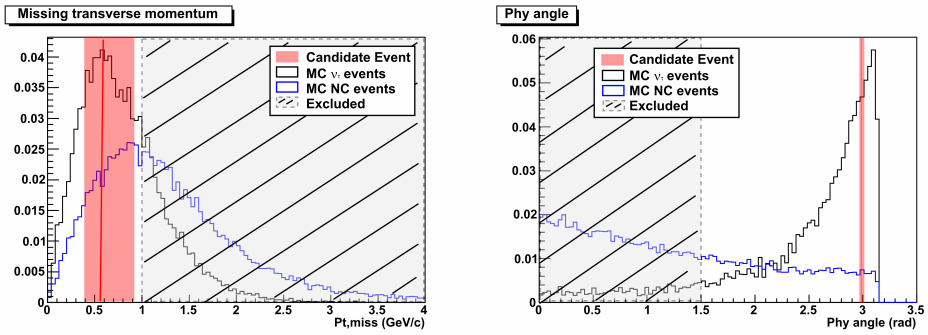

Figure 7.3: Monte-Carlo distributions of the $P_{t,miss}$ at primary vertex (left) and the φ angle between the parent track and the rest of hadronic shower in the transverse plane at the primary vertex (right) for ν_τ CC interactions (black) and for the ν_μ NC background (blue). The red band shows the 68.3% domain of values allowed for he candidate event and the dark red line the most probable value. The dark shaded area represent the excluded region corresponding to the "a priori" tau selection cuts.

Other kinematics variables	
Variable	**Value**
θ angle (rad)	2.08 ± 0.03
Q_t (MeV/c)	710 ± 12
α angle (rad)	0.85 ± 0.01
γ angle (rad)	3.11 ± 0.03

Table 7.2: Values for the other kinematics variables computed for the candidate event.

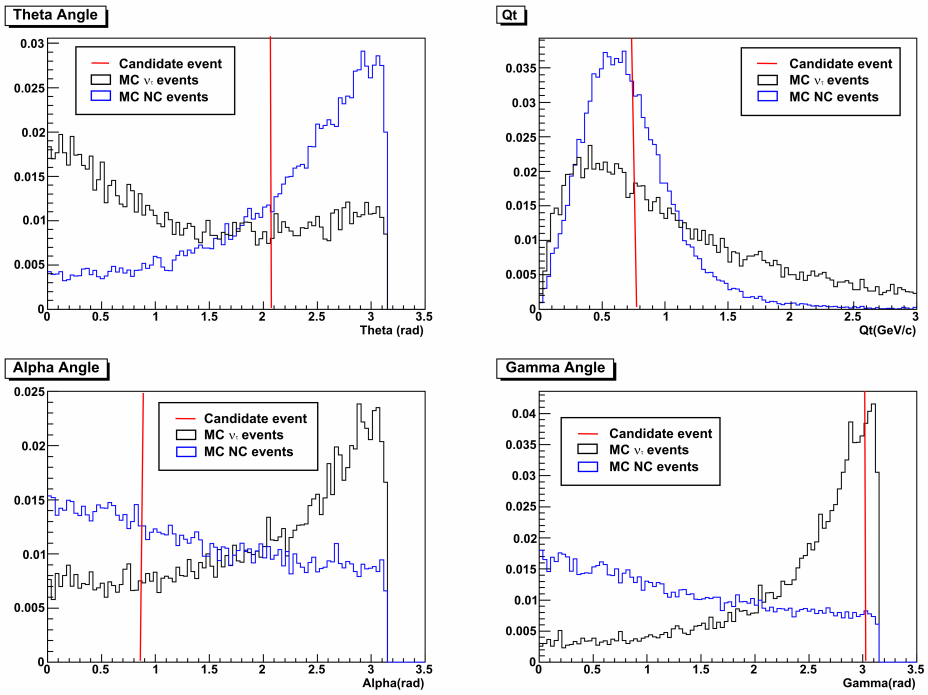

Figure 7.4: Monte-Carlo distributions of the θ angle (top - left); the Q_t variable (top -right); the α angle (bottom - left); the γ angle (bottom right) for ν_τ CC interactions (black) and for the ν_μ NC background (blue). The red line shows the most probable value.

7.3. Background estimation and statistical significance

The secondary vertex is compatible with the decay of a τ^- to $h^-(n\pi^0)\nu_\tau$. The two main sources of background to this channel are:

- the decays to a single charged hadron of charged charmed particles produced in ν_μCC interactions where the primary muon is not identified
- the hadron reinteraction.

The charm background produced in ν_μ interactions amounts to 0.007 ± 0.004 (*syst*) events. The background from ν_e interactions is less than 10^{-3} events.

The dominant background from hadron re-interactions was estimated in chapter 5. The probability that this background of the τ fluctuates to one event is 1.8% (2.36 σ). As the search for τ^- decays is extended to all four channels the total background becomes 0.045 ± 0.023 (*syst*). The probability that this fluctuates to one event is 4.5% (2.01 σ).

At $\Delta m^2_{23} = 2.5\times10^{-3} eV^2$ and full mixing, the expected number of observed τ events with the present analysed statistics is 0.54 ± 0.13 (*syst*) of which 0.16 ± 0.04 (*syst*) in the one prong hadron topology, compatible with the observation of one event.

The significance of a first candidate ν_τCC interaction does not allow to claim the observation of $\nu_\mu \rightarrow \nu_\tau$ oscillation. Given its sensitivity, the OPERA experiment will

require the detection of a few more candidate events in order to firmly establish neutrino oscillation in direct appearance mode through the identification of the final charged lepton.

Conclusions

The observation of ν_τCC interactions in the OPERA experiment could be the proof of the $\nu_\mu \rightarrow \nu_\tau$ oscillation. Each event triggered in the OPERA detector has to be carefully analysed: both the event topology and the event kinematics play an important role in this analysis.

The definition of the event topology and the recognition of the interesting ones is a task accomplished in the scanning laboratories, performed through a well-defined procedure. The working chain applied on a generic event was described and the results obtained in the Salerno scanning laboratory were reported. The location efficiencies, computed with the events of the 2008 run collected in Salerno, were estimated to be of 70%, compatible with the one obtained by the Collaboration using all data taken during the 2008 run.

The kinematical analysis of the events (including the momentum estimation with the MCS method) was another important subject presented in this thesis. In particular, the τ-to-hadron channel was investigated by considering the variables uses to discriminate between the signal and the background both at the primary and at the decay vertex.

The main background for the considered channel is due to the hadron reinteractions, because of the similar topology with the tau decay to a hadron. The data collected were used to validate the Monte-Carlo simulation and to estimate the background from hadron re-interactions. With the actual statistics, the limit on the hadron kink probability was set to 1.54×10^{-3} kinks/NC event over 2 mm of lead. This value is one order of magnitude larger than the kink probability estimated from the simulation; however the statistic is still growing.

The kinematical variables used for the analysis at the primary vertex were the missing transverse momentum, $P_{t,miss}$ and the φ angle. A τ candidate event should have a $P_{t,miss}$ below 1 GeV/c and a φ angle above $\pi/2$. The performance of the selection was computed by selecting the events satisfying such requirements both from a sample of background events and from a sample of signal events. The combined efficiency (i.e due to both cuts), $\epsilon_{pt,miss+\varphi}$, was 14.8% for the background and 62.6% for the signal.

A study was also performed on other variables that could improve the discrimination between the signal and background, but their background suppression power as well as the correlation between them is still under study. This kinematical analysis was also applied to the first ν_τ candidate event found during the 2009 run: the standard kinematical variables were computed and the event passes the selection criteria.

Appendix A

Missing transverse momentum distributions

A.1. ν_μCC sample

A.1.1. Non - smeared sample

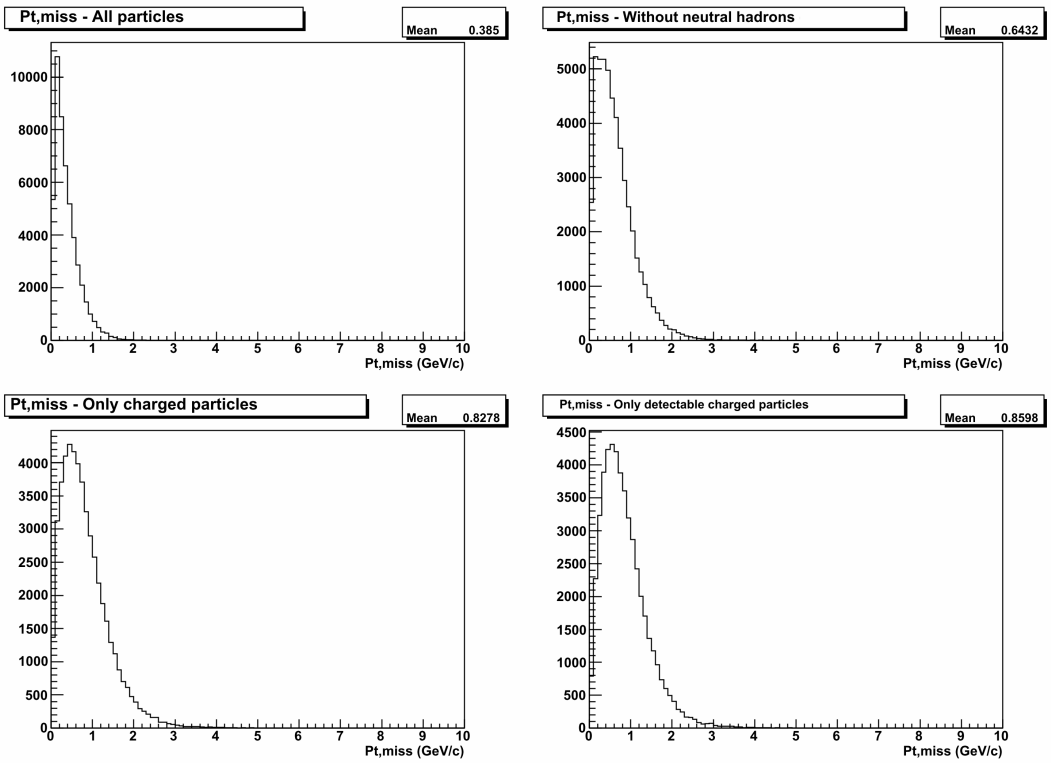

Figure A.1: $P_{t,miss}$ distributions obtained with a non-smeared ν_μCC sample - for details see section 6.3.1 and Figure 6.8

A.1.2. Smeared sample

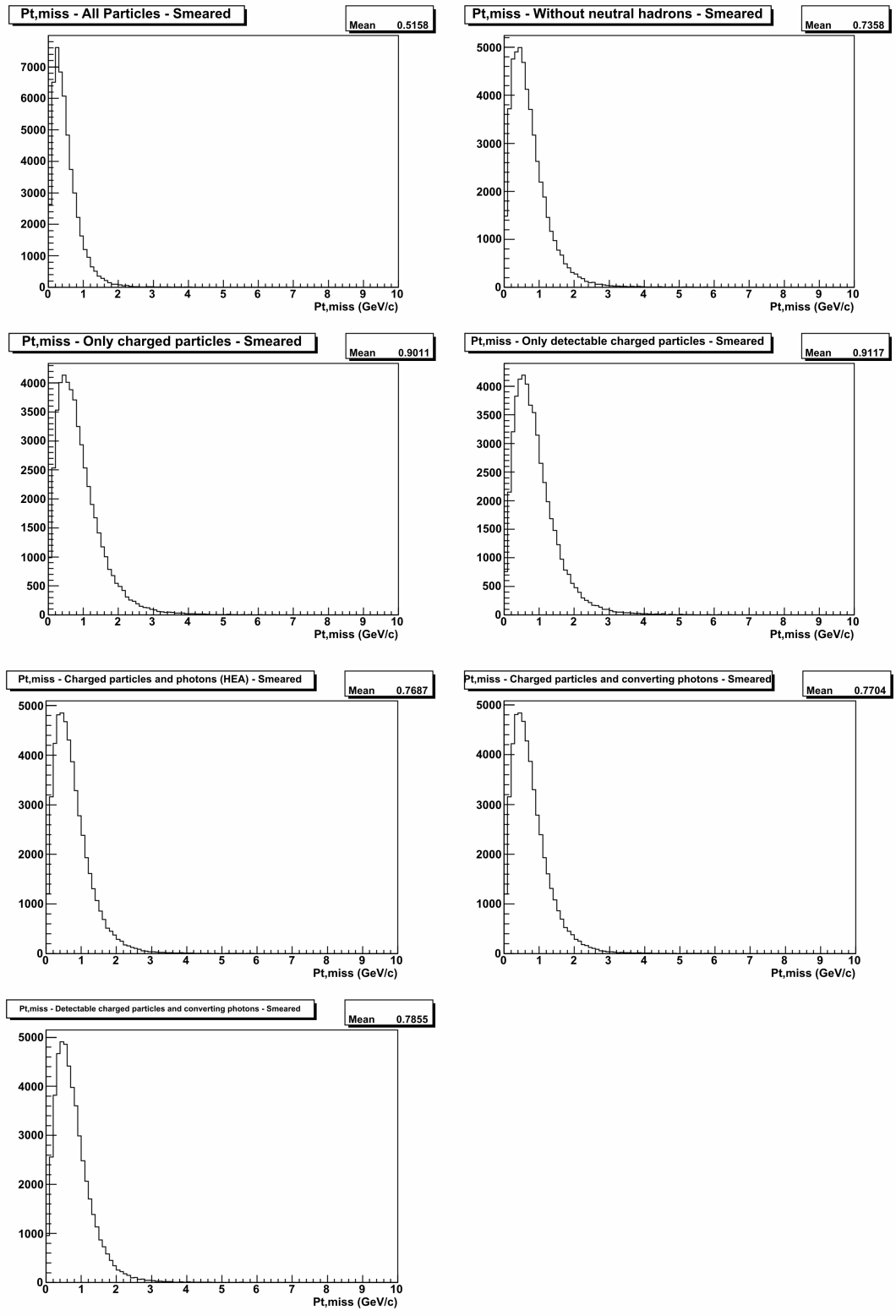

Figure A.2: $P_{t,miss}$ distributions obtained with a smeared ν_μCC sample - for details see section 6.3.1, Figure 6.8 and Figure 6.10

A.2. Comparison with ν_μCC sample

A.2.1. ν_μNC sample (neutrino as muon)

A.2.1.a. Non Smeared sample

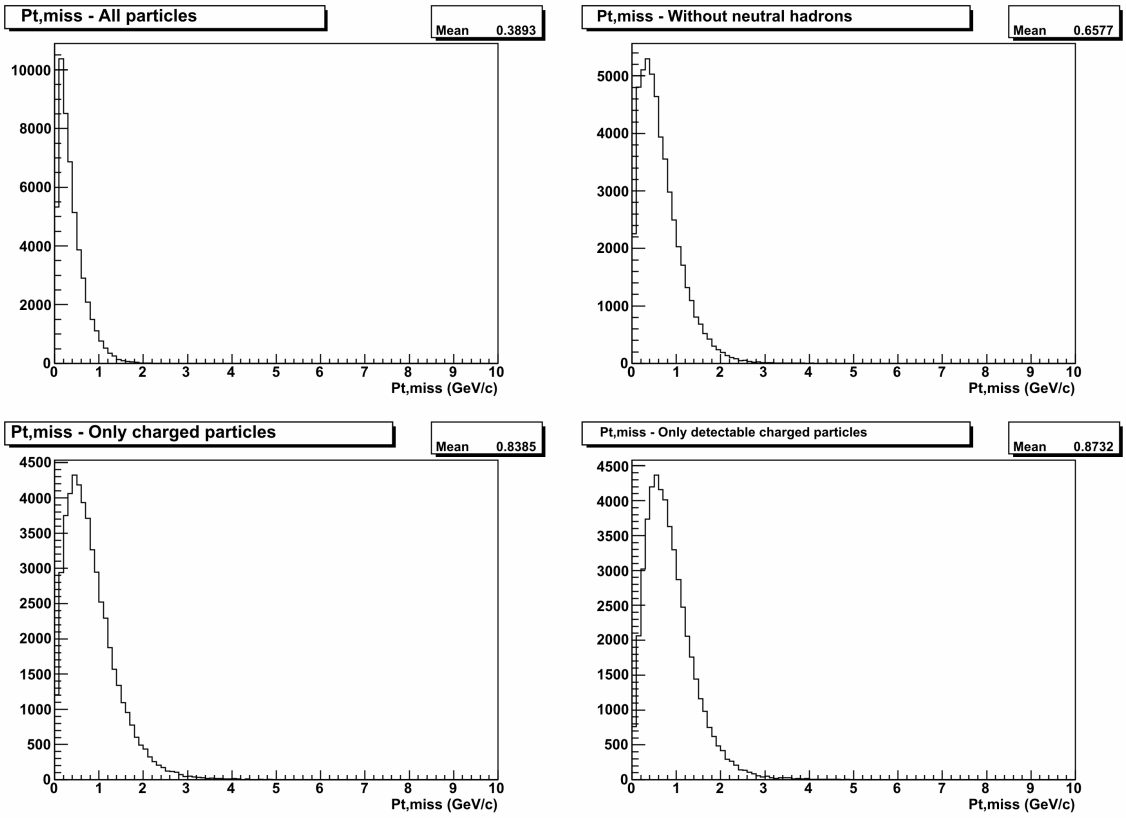

Figure A.3: $P_{t,miss}$ distributions obtained with a non-smeared ν_μNC sample - numbers not shown in previous sectios

A.2.1.b Smeared sample

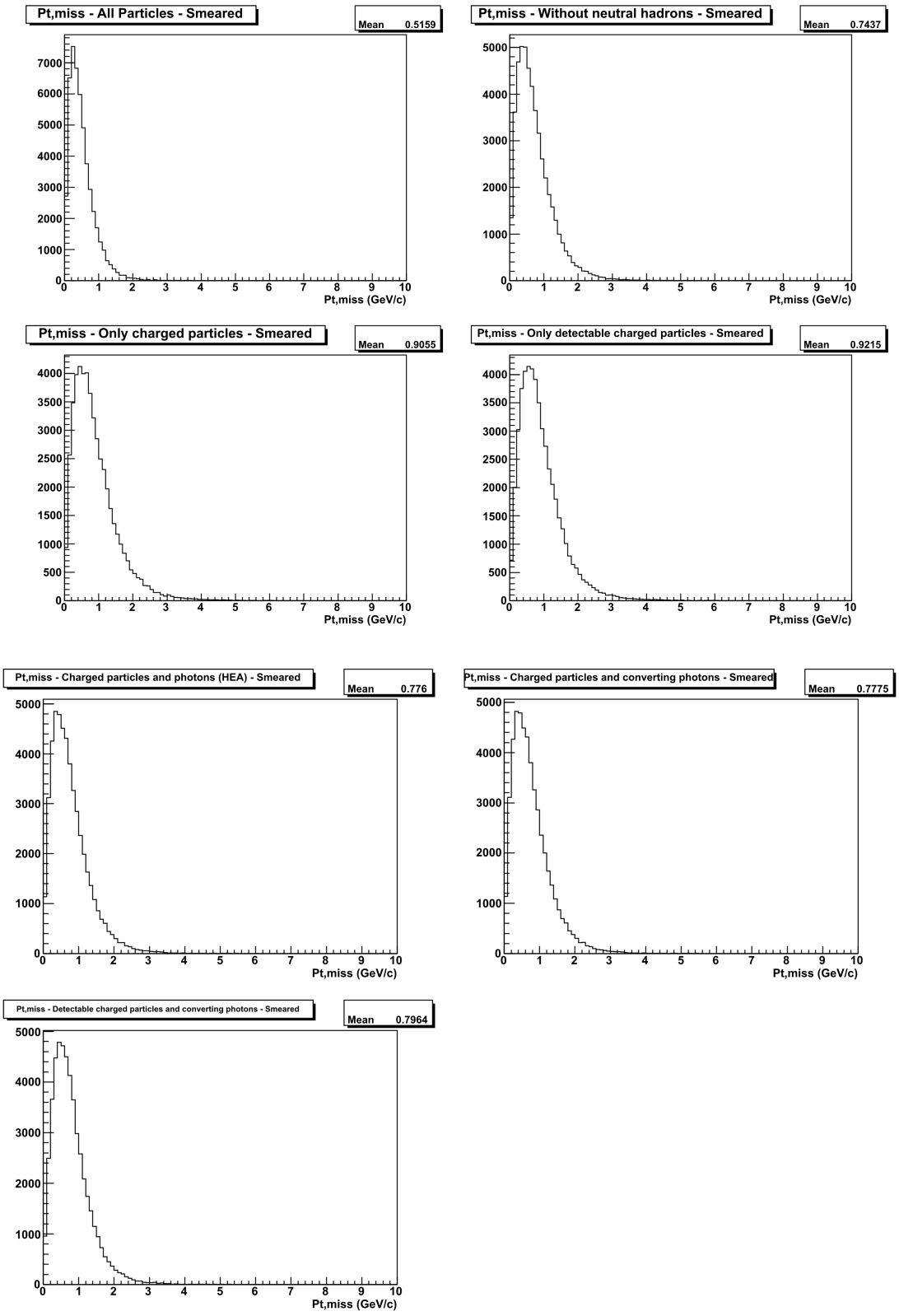

Figure A.4:$P_{t,miss}$ distributions obtained with a smeared ν_μNC sample; the neutrino is treated as a muon particle - for details see section 6.3.2 and Figure 6.12

A.2.2. ν_τCC sample (tau as muon)

A.2.2.a. Non-smeared Sample

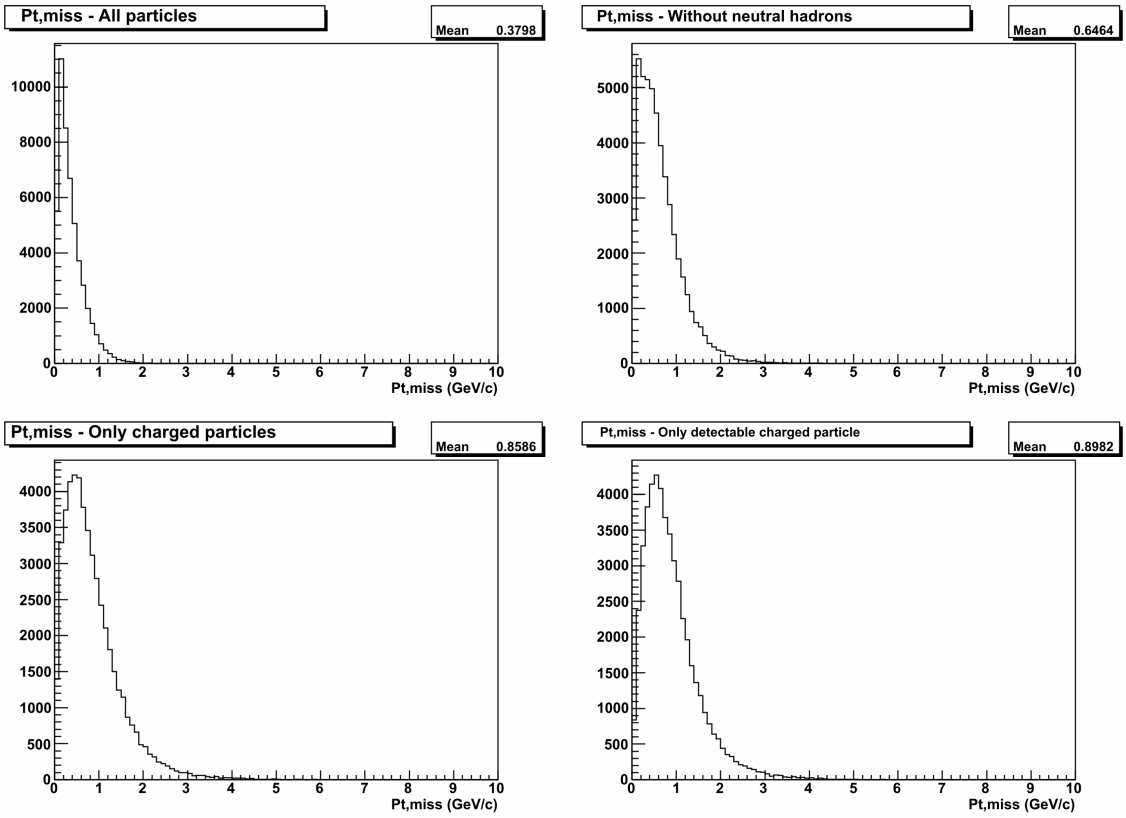

Figure A.5: $P_{t,miss}$ distributions obtained with a non-smeared ν_τCC sample - numbers not shown in previous sectios

A.2.2b. Smeared sample

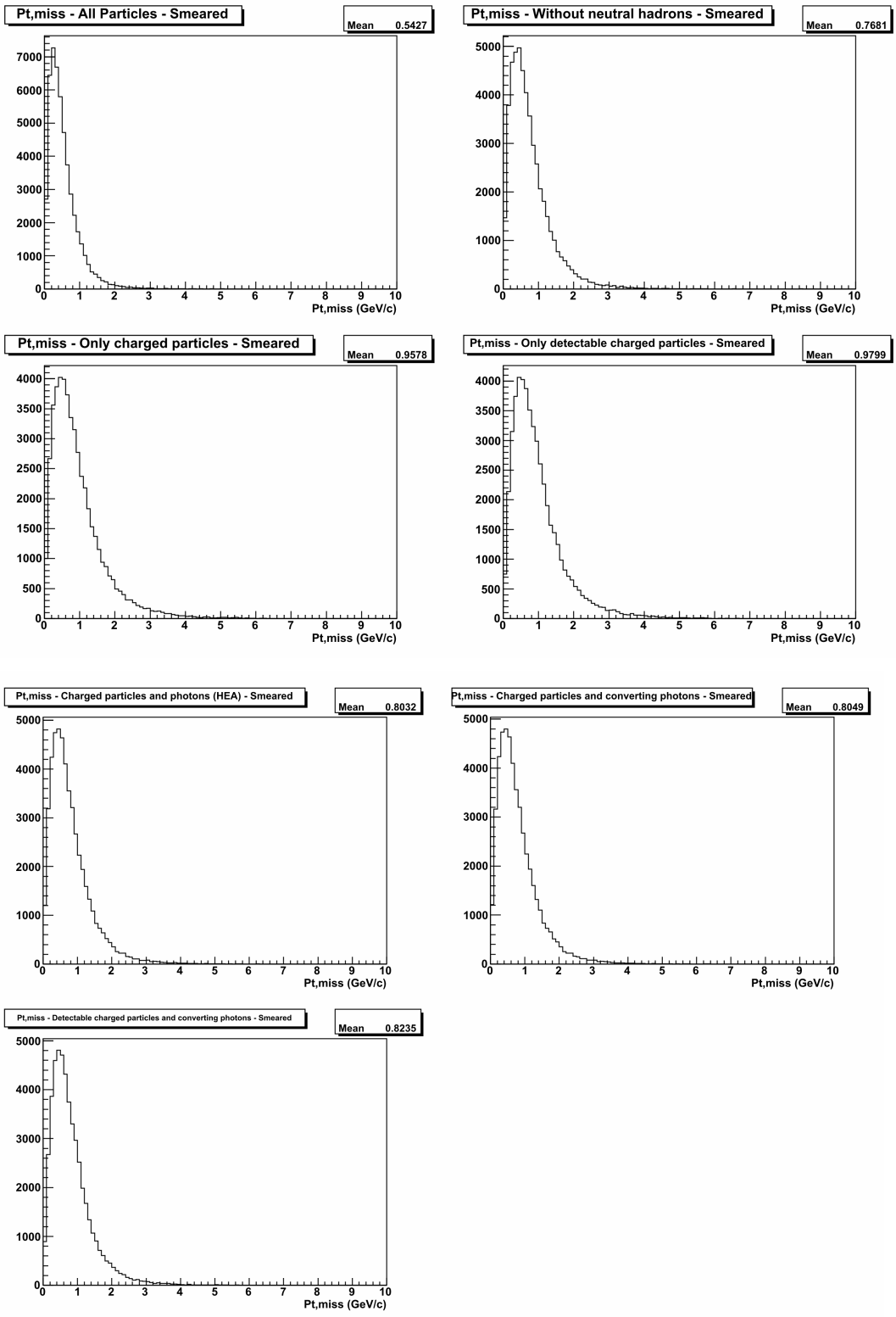

Figure A.6: $P_{t,miss}$ distributions obtained with a -smeared ν_τCC sample - the tau is treated as a muon particle - for details see section 6.3.1 and Figure 6.12

A.3. ν_μNC Sample

A.3.1. Non - smeared sample

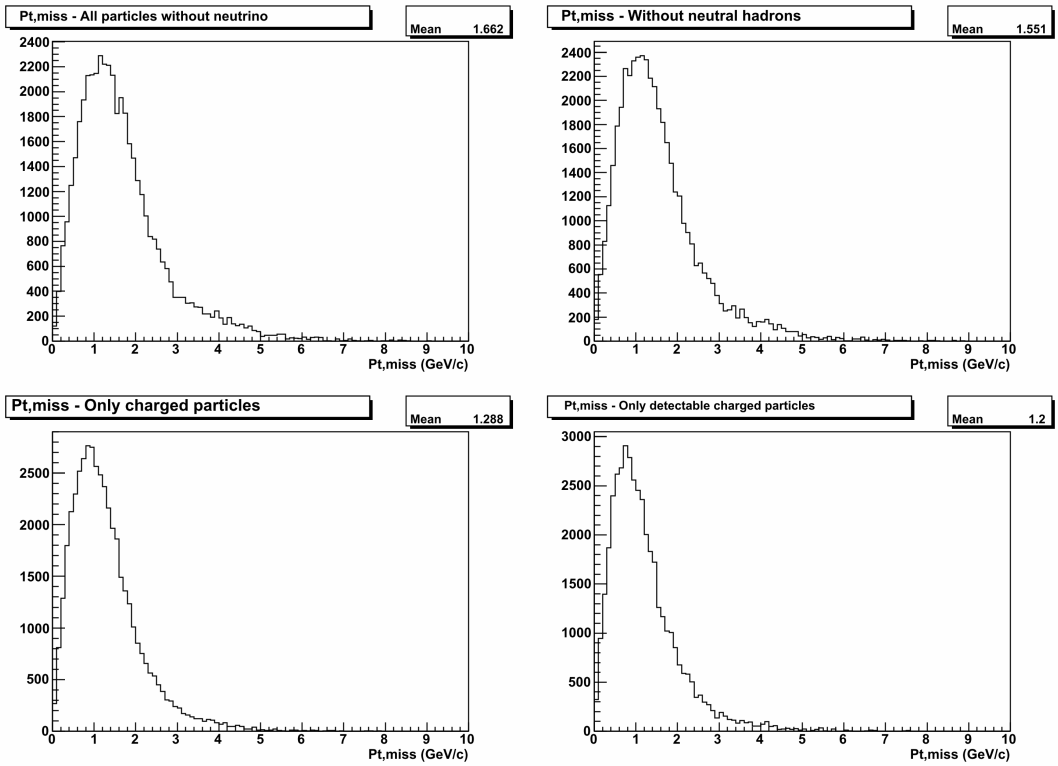

Figure A.7: $P_{t,miss}$ distributions obtained with a non-smeared ν_μNC sample - for details see section6.3.2 and Figure 6.15 99

A.3.2. Smeared sample

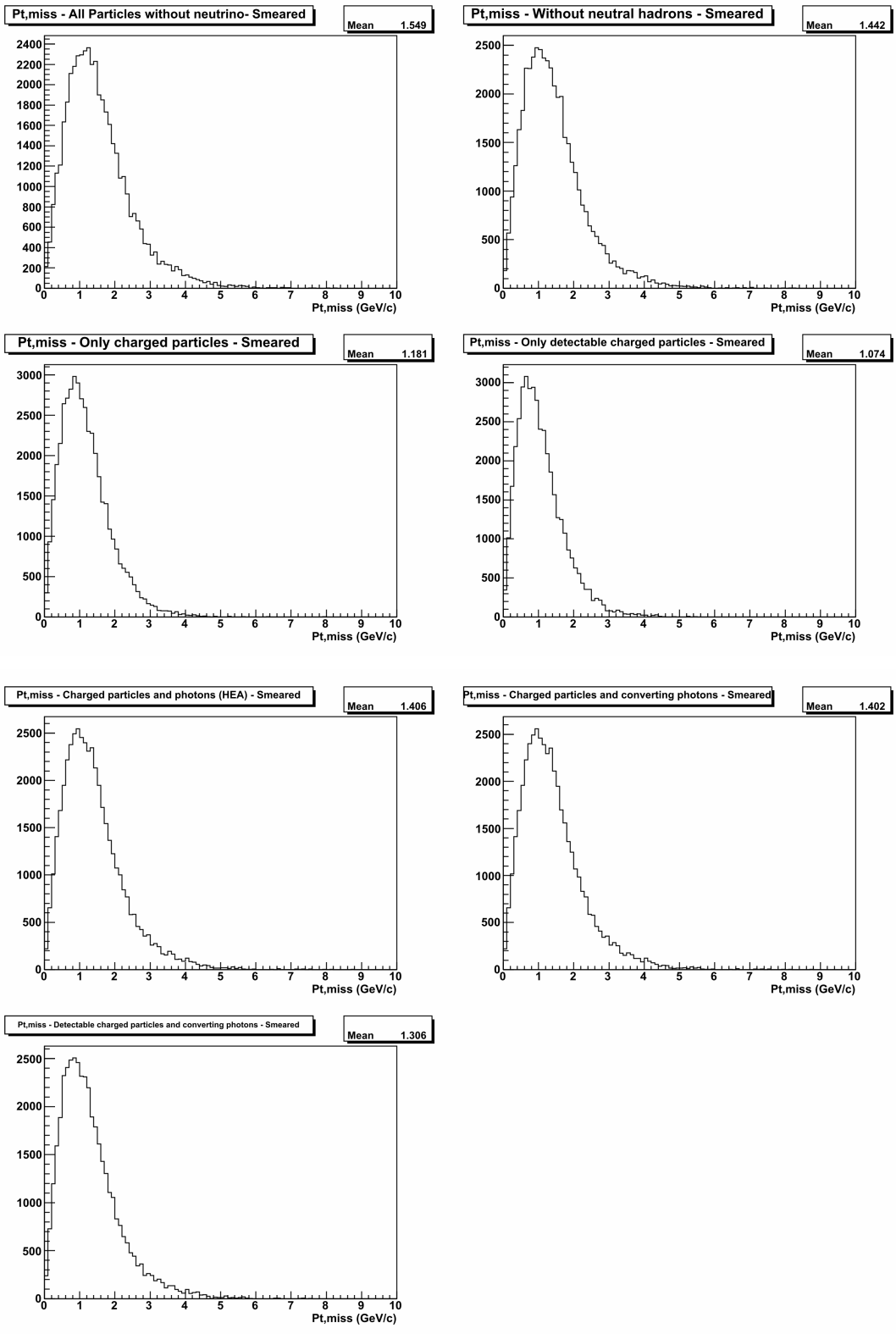

Figure A.8: $P_{t,miss}$ distributions obtained with a smeared ν_μNC sample - for details see section 6.3.2 and Figure 6.15 andFigure 6.21-

A.4. ν_τCC Sample

A.4.1. Non-smeared sample

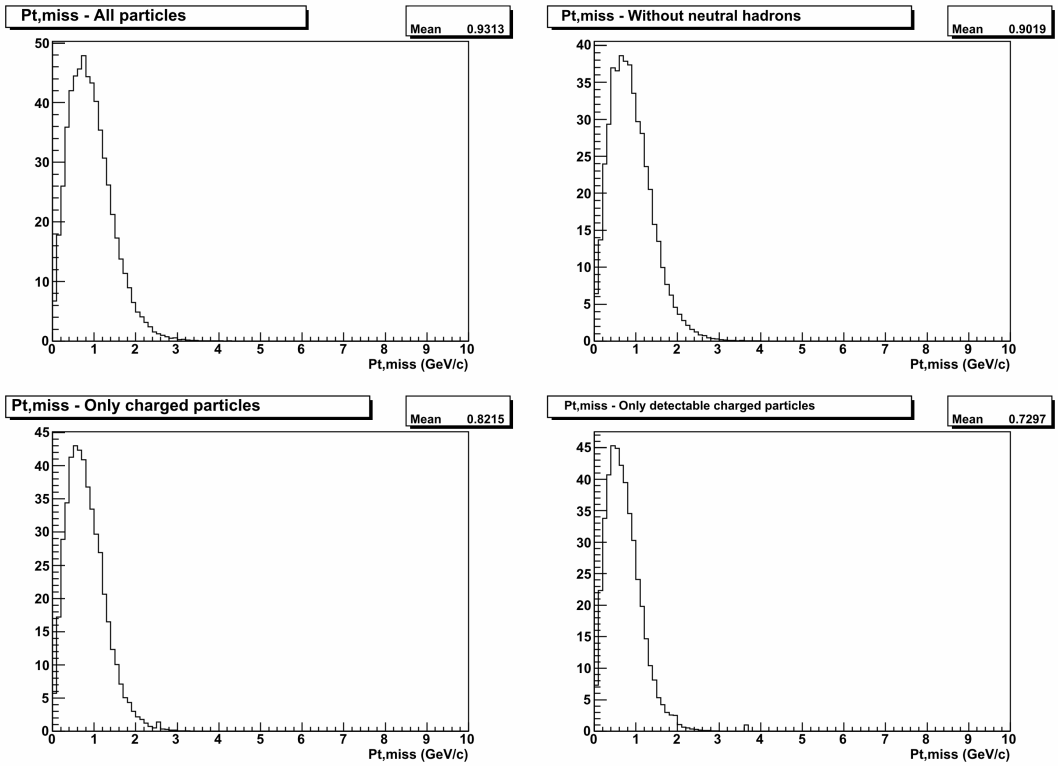

Figure A.9: $P_{t,miss}$ distributions obtained with a non-smeared ν_τCC sample - for details see section 6.3.2 and Figure 6.17

A.4.2 Smeared sample

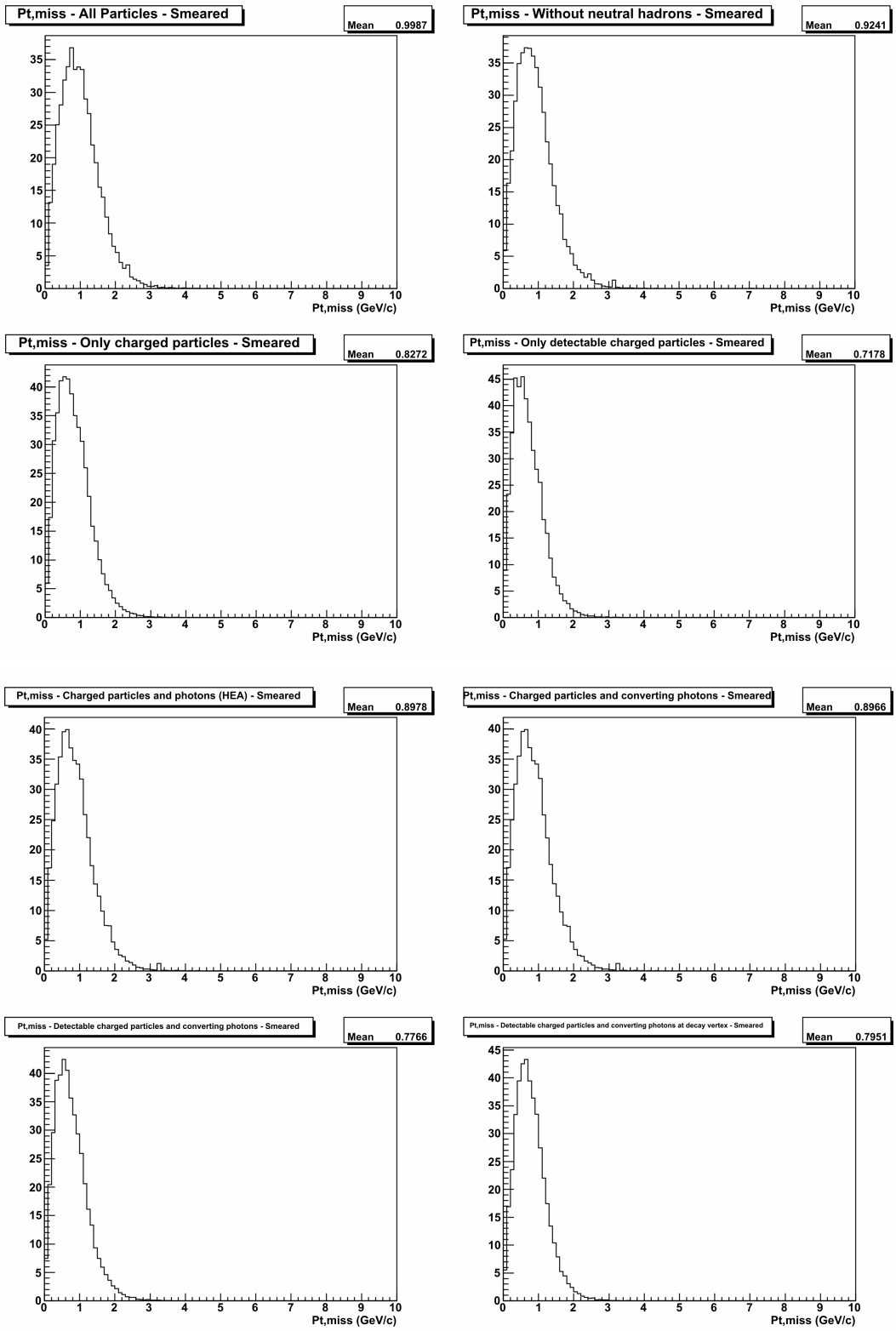

Figure A.10: $P_{t,miss}$ distributions obtained with a smeared ν_τCC sample - for details see section 6.3.2 and Figure 6.17 and Figure 6.21.

References

[1] W. Pauli, letter to radioactive ladies and gentlemen at the Tubingen conference, 4 Dec. 1930.

[2] C.L. Cowan, F. Reines, F.B. Harrison, H.W. Kruse, A.D. McGuire, Science 124 (1956) 123.

[3] M. Goldhaber, L.Grodzins, A.W. Sunyar, Phys. Rev. 109 (1958) 1015.

[4] G. Danby, J.-M. Gaillard, K. Goulianos, L. M. Lederman, N. B. Mistry, M. Schwartz, J. Steinberger , Phys. Rev. 9 (1962) 36.

[5] S.L. Glashow, Nucl. Phys. 22 (1961) 579.

[6] S. Weinberg, Phys. Rev. Lett. 19 (1967) 1264.

[7] A. Salam, (1969), Proc. of the 8th Nobel Symposium on Elementary particle theory relativistic groups and analyticity, Stockholm, Sweden, 1968, edited by N.Svartholm, p.367-377.

[8] R. Davis, Phys. Rev. Lett. 12 (1964) 302.

[9] R. Davis et al., Phys. Rev. Lett. 20 (1968) 1205.

[10] S.M. Bilenky and B. Pontecorvo, Phys. Rept. 41 (1978) 225.

[11] M. Goldhaber, L.Grodzins, A.W. Sunyar, Phys. Rev. 109 (1958) 1015.

[12] E. Majorana, Nuovo Cim. 14 (1937) 171.

[13] S.M. Bilenky, C. Giunti and W. Grimus, Prog. Part. Nucl. Phys. 43 (1999) 1,hep-ph/9812360. a

[14] C. Giunti, M. Laveder, hep-ph/0310238

[15] Z. Maki, M. Nakagawa, and S. Sakata, Prog. Theor. Phys. 28, 870 (1962)

[16] B. Pontecorvo, Zh. Eksp. Teor. Fiz. 53, 1717 (1967) [Sov. Phys. JETP 26, 984 (1968)].

[17] R.N. Mohapatra and P.B. Pal, Massive neutrinos in physics and astrophysics (World Sci. Lect. Notes Phys. 72, 2003).

[18] C.W. Kim and A. Pevsner, Neutrinos in physics and astrophysics (Harwood Academic Press, Chur, Switzerland, 1993), Contemporary Concepts in Physics, Vol. 8.

[19] J.N. Bahcall, Neutrino Astrophysics (Cambridge University Press, 1989).

[20] Chlorine experiment. The experimental tecnique was suggested in B. Pontecorvo, Chalk River Lab. PD ˝U205 report (1946).

[21] **Homestake** .The final results of the Homestake experiment are reported in B.T. Cleveland et al., Astrophys. J. 496 (1998) 505.

[22] **Gallium experiments**. Gallex collaboration, Phys. Lett. B447 (1999) 127

[23] **SAGE.** SAGE collaboration, Phys. Rev. C60 (1999) 055801d

[24] **GNO**: GNO collaboration, Phys. Lett. B616 (2005) 174 (hep-ex/0504037)

[25] **Kamiokande**. Y. Fukuda et al., Phys. Rev. Lett. 77 (1996) 1683.

[26] **Super-Kamiokande**. Super-Kamiokande collaboration, hep-ex/0508053

[27] **Super Kamiokande.** Super Kamiokande Coll., Nucl. Phys. B145 (2005) 112

[28] **SNO**. First phase: SNO collaboration, Phys. Rev. Lett. 87 (2001) 071301 (nucl-ex/0106015)

[29] **SNO**. SNO collaboration, Phys. Rev. Lett. 89 (2002) 011301 (nucl-ex/0204008);

[30] **SNO** collaboration, Phys. Rev. Lett. 92 (2004) 181301 (nucl-ex/0309004)

[31] **KamLAND**. KamLAND collaboration, Phys. Rev. Lett. 90 (2003) 021802 (hep-ex/0212021);

[32] **KamLAND**. KamLAND collaboration, Phys. Rev. Lett. 94 (2005) 081801 (hep-ex/0406035)

[33] Reines, F., M.F. Crouch, T.L. Jenkins, W.R. Kropp, H.S. Gurr, G.R. Smith, J.P.F. Sellschop,B. Meyer, 1965, Phys. Rev. Lett. 15 , 429.

[34] Achar, H. et al,, 1965, Phys. Lett. 18 , 196

[35] Zatsepin, G.T. and V.A. Kuzmin, 1962, Sov. J. Nucl. Phys 14 , 1294.

[36] Osborne, J.L., S.S. Said, A.W. Wolfendale, 1965, Proc. Phys. Soc. 86 , 93.

[37] **IMB**, R.M. Bionta et al., Phys. Rev. D38 (1988) 768

[38] **Soudan** 2, M. Sanchez et al., hep-ex/0307069

[39] **MACRO**, M. Ambrosio et al., Phys. Lett. B566 (2003) 35 (hep-ex/0304037)

[40] **CHOOZ**, M. Apollonio et al., Phys. Lett. B466 (1999) 415, hep-ex/9907037

[41] **CHOOZ,** M. Apollonio et al., Eur. Phys. J. C27 (2003) 331, hep-ex/0301017

[42] **K2K**, K2K collaboration, Phys. Rev. Lett. 90 (2003) 041801 (hep-ex/0212007)

[43] **K2K**, K2K collaboration, Phys. Rev. Lett. 94 (2005) 081802 (hep-ex/0411038)

[44] **MINOS**, MINOS collaboration, hep-ex/0605058

[45] Zacek, G. et al., 1986, Phys. Rev. D 34 , 2621.

[46] Vidyakin, G.S. et al., 1994, JETP Lett. 59 , 390.

[47] Achkar, B., et al., 1995, Bugey Coll., Nucl. Phys. B 434 , 503

[48] **LSND**, A. Aguilar et al., Phys. Rev. D64 (2001) 112007, hep-ex/0104049

[49] **Karmen,** B. Armbruster et al., Phys. Rev. D65 (2002) 112001, hep-ex/0203021

[50] **CCFR/NuTeV**, A. Romosan et al., Phys. Rev. Lett. 78 (1997) 2912, hep-ex/9611013

[51] **NOMAD**, P. Astier et al., Phys. Lett. B570 (2003) 19, hep-ex/0306037

[52] **MiniBooNE**, The MiniBooNE Collaboration, ArXiv:0704.1500v2, 2007

[53] **CHORUS,** E. Eskut et al. (CHORUS Collaboration), Nucl. Instrum. Meth. A 401, 7(1997)

[54] **K2K,** Nishikawa, K. et al., 1997, KEK-PS proposal, Nucl. Phys. Proc. Suppl. 59 , 289.

[55] **K2K,** Nishikawa, K. et al., 2001, K2K Coll., Proceedings of the EPS HEP 2001 Conference, Budapest, Hungary.

[56] **OPERA,** OPERA Collaboration, M. Guler et al. Experimental proposal, CERN-SPSC-2000-028

[57] http://www-numi.fnal.gov/PublicInfo/forscientists.html

[58] CNGS project: http://proj-cngs.web.cern.ch/proj-cngs/ OPERA Collaboration, M. Guler et al. CERN-SPSC-2001-025

[59] R. Acquafredda et al. The OPERA experiment in the CERN to Gran Sasso neutrino beam. JINST, 4(04):P04018, 2009

[60] Nucl. Instr. Meth. A,577(3) :523$^{\perp}$ 539, 2007.

[61] ArXiv:0804.1958v1 12 Apr 2008

[62] M. Ambrosio et al., IEEE Trans. Nucl. Sci. 51, 975 (2004)

[63] A. Bergnoli et al., Nuclear Physics B (Proc. Suppl.) 158 (2006)

[64] E. Barbuto et al., Nucl. Instr. Meth. A525 (2004)

[65] ArXiv:1102.1882v1 9 Feb 2011

[66] C.Bozza et al, IEEE Nuclear Science Symposium Conference Record, 2005

[67] T. Nakano (CHORUS Collaboration), International Europhysics Conference on High-Energy Physics (HEP 2001), Budapest, Hungary, 12-18 July 2001

[68] Y. Déclais, 48th International School of Subnuclear physics, Erice September 2010

[69] G.Romano, Emulsioni nucleari, (A.A 1977-1978), Università di Roma

[70] N.Armenise et al., Nucl. Instr.Meth. A551, 261-270 (2005)

[71] S.Amendola et al. DSF-US-4/98 (1998)

[72] http://operaweb.lngs.infn.it/operawiki/index.php/DecaySearchProc

[73] G. De Lellis, internal communication

[74] G.De Lellis - Collaboration Meeting (September 2010)

[75] OPERA internal note OPLAPP-1812-01, December 2001

[76] OPERA internal note OPLAPP-2409-08, September 2008

[77] Nuclear Instruments and Methods in Physics Research A 512 (2003) 539–545

[78] V.I.Highland, NIM 129, 497 (1975)

[79] M. Besnier, private communication

[80] R.Brun, M.Hansroul., GEANT3.16 User's guide Phys320 (1985).

[81] M.Besnier., PhD. thesis (2008) LAPP-T-2008-02.

[82] A.Sheshukov, internal communication, March 2010

[83] D.Autiero, internal communication, March 2010

[84] ArXiv - 1006.1623v1, 8 June 2010

[85] T. Ariga, private communication

[86] CERN-SPSC-2010-020 / SPSC-SR-064

[87] T.Ariga, internal communication, March 2010

[88] F.Di Capua, internal communication, March 2010

[89] D. Autiero. The OPERA event generator and the data tuning of nuclear reinteractions. Nucl. Phys. B - Proceedings Supplements, 139:253 – 259, 2005

[90] F. R. Juget, internal communication, November 2008

Acknowledgement

I would like to express my deep and sincere gratitude to my supervisor, Prof. Giuseppe Grella for giving me the chance to work for my Ph.D. in the Emulsion Group of the University of Salerno. His wide knowledge and his logical way of thinking have been of great value to me. His understanding, encouraging and personal guidance have provided a good basis for the present thesis.

I especially thank Dr. Cristiano Bozza for his valuable advice and friendly help, for carefully reading the draft of this thesis and his comments; without him it would not work.

I wish to express my warm and sincere thanks to Prof. Dario Autiero who gave me the opportunity to work with him at the IPNL (Lyon). He introduced me to the kinematical analysis of events: his concepts have had a remarkable influence on my view of the field of high-energy Physics.

During this work I have collaborated with many colleagues to whom I am thankful; I wish to express my warmest thanks to all those who have helped me with my work at IPNL: Prof. Yves Déclais, Prof. Elisabetta Pennacchio, Dr. Antoine Cazes and Dr. Timothée Brugière

I wish to acknowledge my group mates Maurizio di Marino, Dr. Chiara Sirignano and Dr. Simona Maria Stellacci, and Marialaura Cozzuto for making the stay in Salerno such a wonderful time.

I owe my loving thanks to my family: they have spent a lot of efforts in supporting my research. Without their encouragement and understanding it would have been impossible for me to bring this work to completion. My special gratitude is due to my brother, my sisters and their families for their loving support.

Additionally, I like to thank all other young people and friends I met on the way in the various universities around Europe; thanks to them I have not only learned about Physics, but also about life!